CFD Study on Flame Flashback in Low Swirl Premixed Burners

by

Darshan Raju

to obtain the degree of Master of Science
at the Delft University of Technology,
to be defended publicly on 24 August 2022.

Student number: 5068800
Thesis committee: Prof. dr. ir. S.A. Klein, TU Delft, supervisor, chair
Dr. ir. R. Pecnik, TU Delft
Dr. I. Ivan Langella, TU Delft

TU Delft

Abstract

The energy transition from fossil fuels to renewable energy sources is crucial for climate resilience. In particular, hydrogen combustion in gas turbine combustors is expected to play an essential role in the energy transition. Hence, a fuel-flexible gas turbine combustor operating with a wide range of natural gas and hydrogen fuels is necessary. Low Swirl Burner (LSB), developed at Lawrence Berkeley National Laboratory (LBNL), is one of the promising solutions for fuel-flexible gas turbine combustors. However, hydrogen combustion in LSB at lean conditions is accompanied by several challenges, especially flame flashback. Flashback results in damage and shutdown of gas turbines. Recent experimental studies performed on LSB revealed the occurrence of flame flashback at a high volume percentage of hydrogen, but the exact cause of the flashback in LSB is yet to be discovered.

In this study, numerical modelling of low swirl premixed burner with turbulent flow and high hydrogen content is performed. RANS simulations are performed initially for the non-reacting flow and are validated with the experimental measurements. Flamelet combustion model with Zimont Turbulent Flame speed correlation is employed to model the reacting flow. The flame front position obtained from the Zimont correlation closely agrees with the experiments. Further, Algebraic Flame Surface Wrinkling (AFSW) correlation is compared with the Zimont correlation for hydrogen-enriched flames. Based on the comparison, it is concluded that the AFSW correlation did not lead to a significant difference. However, both the correlations failed to model the flashback process. Therefore, the potential mechanism responsible for the flame flashback in LSB is examined. It has been found that none of the standard flashback mechanisms is accountable for the flame flashback in LSB. Furthermore, the effect of different flame shapes reported in the experiments is evaluated. It has been observed that 'M' shape flame has more propensity to flashback than 'V' shape flame. Then, a shear layer and turbulent wakes in the premix nozzle of the LSB were noticed. Hence, an increase in flame speed due to the local enrichment of thermo-diffusive unstable hydrogen flame and all the aforementioned effects might lead to a sudden flashback in LSB.

Acknowledgement

A great deal of appreciation is extended to my supervisor Professor Sikke Klein for giving me such a remarkable opportunity to work on this challenging topic for my Master's thesis. This work would never be possible without his continuous guidance and support.

I would like to express my gratitude to Dr. ir. R. Pecnik and Dr. I. Ivan Langella for being a part of my thesis committee.

I am very thankful to Professor Dirk Roekaerts for always being available for short discussions. His depth explanations have aided me in understanding the physics of combustion better. Additionally, I would like to thank Mathieu for providing access to the cluster and helping me with the simulations.

My deepest thanks to my parents for believing and supporting me during my Masters's studies at TU Delft. Finally, I want to thank my friends for their help, love, and care during my Master's studies at TU Delft.

Darshan Raju
Rijswijk, August 2022

Contents

Nomenclature

Abbreviations

AFSW	Algebriac flame Surface Wrinkling
BSLKW	Baseline k-ω
CFD	Computational Fluid Dynamics
CIVB	Combustion Induced Vortex Breakdown
CRZ	Corner Recirculation zone
DNS	Direct Numerical Simulation
EBM	Eddy Breakup Model
EDC	Eddy Dissipation Concept
EDM	Eddy Dissipation Model
HSB	High Swirl Burner
HSI	High Swirl Injector
IGT	Industrial Gas Turbine
IRZ	Inner Recirculation zone
ISL	Inner Shear Layer
LBNL	Lawrence Berkeley National Laboratory
LBO	Lean Blow Out
LES	Large Eddy Simulation
LSB	Low Swirl Burner
LSI	Low Swirl Injector
NETL	National Energy Technology Laboratory
ORZ	Outer Recirculation zone
OSL	Outer Shear Layer
PIV	Particle Image Velocimetry

PVC	Precessing Vortex Core
RANS	Reynolds Averaged Navier Stokes
RKE	Realizable k-ϵ
RNG	Re-Normalisation group k-ϵ
RSM	Reynolds Stress Model
RZ	Recirculation zone
SimVal	Simulation Validation
SKE	Standard k-ϵ
SKW	Standard k-ω
SSTKW	Shear Stress Transport k-ω
STP	Standard Temperature and Pressure
TFSC	Turbulent Flame Speed Closure
TKE	Turbulent Kinetic Energy
UDF	User Defined Function
URANS	Unsteady Reynolds Averaged Navier Stokes
VB	Vortex Breakdown

Symbols

α	Heat diffusivity (m^2/s)
δ	Boundary layer thickness (m)
δ_f	Flame thickness (m)
$\dot{m}$	Mass flow rate (Kg/s)
ϵ	Turbulent dissipation rate (m^2/s^2)
κ	Flame stretch (s^{-1})
λ	Thermal conductivity ($W/m.K$)
μ	Dynamic viscosity (Pa/s)
ν	Kinematic viscosity (m^2/s)
ω	Turbulent specific dissipation rate ($1/s$)
ϕ	Equivalence ratio (-)

ρ	Density (Kg/m^3)
τ	Shear stress (Pa)
θ	Swirl angle (-)
$\vec{\omega}$	Vorticity ($1/s$)
D	Diameter (m)
k	Turbulent kinetic energy (m^2/s^2)
L_m	Markstein length (m)
l_η	kolmogorov length scale (m)
l_t	Integral length scale (m)
P	Pressure (Pa)
P_o	Inlet pressure (Pa)
R	Radius (m)
R	Reynolds stress (m^2/s^2)
S_L	Stretched laminar flame speed (m/s)
S_L^0	Unstretched laminar flame speed (m/s)
S_T	Turbulent flame speed (m/s)
S_{ij}	Strain rate component ($1/s$)
$S_{T,LC}$	Local Consumption Turbulent Flame speed (m/s)
$S_{T,LD}$	Local Displacement Turbulent Flame speed (m/s)
T_o	Inlet temperature (K)
t_η	kolmogorov time scale ($1/s$)
t_{l_t}	Integral time scale ($1/s$)
U^+	Non dimensional velocity (m/s)
U_τ	Friction velocity (m/s)
$u_i^{'}$	Fluctuating velocity component (m/s)
U_o	Bulk velocity (m/s)
U_z	Axial Velocity (m/s)
U_{z_c}	Central channel axial velocity (m/s)

U_{z_s}	Swirler axial velocity (m/s)
y^+	Non dimensional wall distance $(-)$
Z	Axial Position (m)
t	time (s)

Non-dimensionalnumbers

Da	Damköhler number
Ka	Karlovitz number
Le	Lewis number
Ma	Markstein number
Re	Reynolds number
S	Swirl number
Sc	Schmidt number

List of Figures

List of Tables

1

Introduction

The majority of the energy used by mankind is extracted from fossil fuels like oil, coal and gas, which is evident from the figure 1.1. Since the industrial revolution, humans have constantly exploited fossil fuels, mostly for electricity generation. According to Environmental Protection Agency (EPA) report from 2019, 65% of the world's electricity is generated from fossil fuels [2]. These fossil fuels are the largest source of carbon dioxide (CO_2) and Carbon monoxide (CO) emissions. By the end of 2030, it is expected that fossil fuels will lead to 39 billion tonnes of CO_2 emission, which in turn causes 2°C rise in global temperatures [16][94]. An energy transition from fossil fuels to renewable energy is inevitable to avoid global warming.

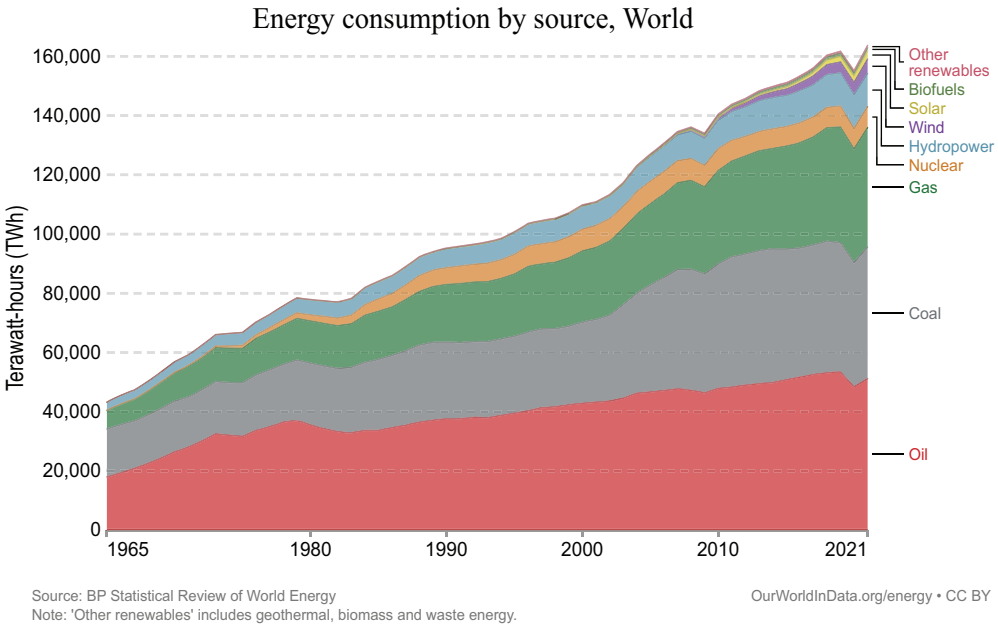

Figure 1.1: Statistics of world energy consumption by fuel source, obtained from Our World in Data, Ref.[49]

The utilization of renewable resources like wind and solar for electricity generation has been gaining interest in recent years due to their advancements in cost-effective technologies. One of the major drawbacks of these renewable sources is the seasonal variation of energy supply. The inconsistent energy production is termed as energy intermittency [118].

Substitution of renewable sources instead of fossil fuels results in power outages since the conventional electric grids function based on the just-in-time principle, meaning, the produced energy is transmitted instantly to the end user. This energy intermittency problem can be addressed by employing energy storage systems. One such implementation of energy storage systems is converting excess energy generated from renewable sources into mechanical energy via compressing the air and pumping the water to an elevated reservoir. Later, a turbine is utilized to extract electricity when there is energy demand. However, implementing them on a large scale requires a large landmass and high infrastructural investment [77] [102].

Energy can also be stored in the form of chemical energy. One such example is batteries, but these have a lower power density when compared to fossil fuels and the lifetime of batteries is limited [132]. The other alternative for chemical storage is hydrogen production through steam reforming, partial oxidation of liquid fuels and electrolysis when there is a surplus of electricity [86]. The so-produced hydrogen can be used as fuel in Industrial Gas Turbines (IGTs) to balance the electricity demand since hydrogen is free from carbon emissions.

The major drawback of employing hydrogen in IGTs is nitrogen oxides (NO_x) emissions, where NO_x emissions and the efficiency increase proportionally with temperature. Since NO_x emissions are related to smog and acid rain, which causes respiratory illness and environmental damage, European Union (EU) has imposed stringent rules on developing IGTs [72]. To attain the highest possible efficiency considering the emission regulation by the EU, a swirl stabilized, lean-premixed combustion technique is implemented. The lean-premixed combustion refers to the excess oxidizer premixed with the fuel in the premixed system before entry into the combustion chamber. Upon combustion, a flame front is produced inside the combustion chamber. Here, the flame is stabilized by imparting swirling motion to the turbulent flow for enhanced mixing.

Apart from the NO_x emissions, various technical challenges are encountered in IGTs when the natural gas is replaced with hydrogen-enriched fuel. Due to the highly reactive and diffusive nature of hydrogen [105], the flame speed of hydrogen-enriched fuel could be five times greater than that of natural gas. Therefore, the flame will likely propagate upstream into the premix system against the incoming flow. The upstream flame propagation, as shown in figure 1.3 is known as a flashback, an important safety concern, which results in damage and shutdown of IGTs. Flashback in IGTs not only damages the hardware but also leads to increased emissions [9]. Flashback occurs when there is an imbalance between the local flame speed and flow velocity. The standard three modes of flashback that have been documented: core flow, Combustion Induced Vortex Breakdown (CIVB) (see figure 1.2) and boundary layer (see figure 1.3) [9]. Therefore, this thesis focuses on the cause that leads to flame flashback in Low Swirl Burners (LSB).

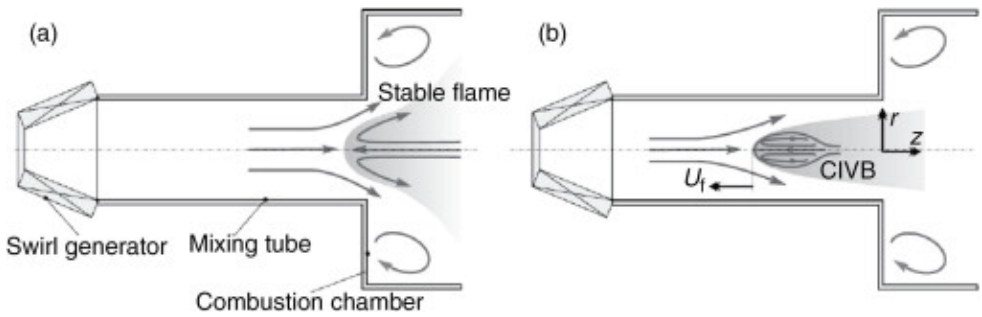

Figure 1.2: Illustration of swirl stabilized premixed flame, (a) depicts the stable flame and (b) depicts the unstable flame due to Combustion Induced Vortex Breakdown (CIVB), obtained form Kroener et al. [64]

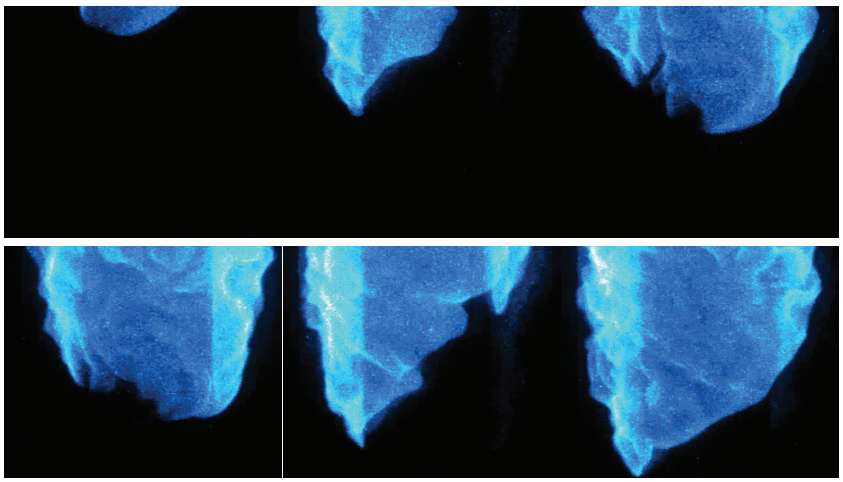

Figure 1.3: Snapshots of boundary layer flashback event over the centre body of the premixed methane-air flame in swirling flow, where the direction of the flow is from bottom to top, obtained form Ebi and Clemens [33]

1.1. Thesis Motivation

The hydrogen-enriched fuel has relatively less carbon emissions than pure hydrocarbon fuels [6] [74][78][90]. However, hydrogen-enriched fuels at leaner conditions pose many difficulties like the flame flashback, high flame speed, and instabilities. Therefore, by investigating the effect of hydrogen in hydrogen-enriched fuels, the influence of hydrogen in such a flame can be studied, which will pave the way to study pure hydrogen (100%) fuel-based combustion systems.

Swirling flames are used in IGTs because of their aerodynamic flame stabilization, high turn-down ratio and fewer emission footprints [95]. The swirling flow with tangential and axial velocity components enhances fuel mixing and turbulence. The figure 1.4 depicts the different injectors, namely High Swirl Injector (HSI) and Low Swirl Injector (LSI) employed in the High Swirl Burners (HSB) and Low Swirl Burner (LSB), respectively. The HSB is predominately used in hydrocarbon fuel-based combustion systems because of its flame stabilizing mechanism. In HSB, Inner Recirculation Zone (IRZ) formed due to Vortex Breakdown (VB) acts as a flame stabilizer [59]. Due to the complex interaction between the IRZ and the flame in HSB, employing hydrogen-enriched fuel in HSB is difficult and challenging [54]. Alternatively, LSB is devoid of such interactions [19] and have higher flashback resistance than HSB [19]. However, the flame flashback in LSB was encountered at high hydrogen content [7] [19] and the mechanism responsible for flame flashback is not understood well. Therefore, this thesis aims to better understand the mechanism accountable for flashback in LSB.

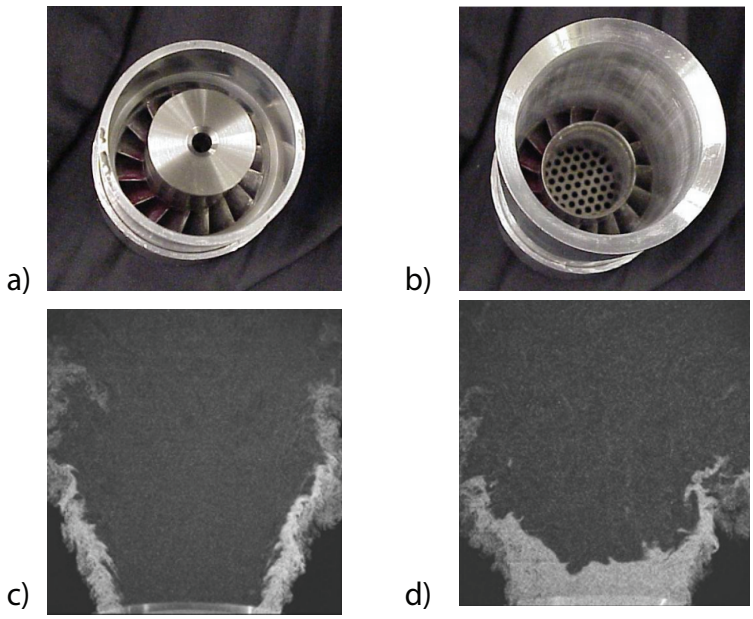

Figure 1.4: Image of High Swirl Injector (a) and Low Swirl Injector (b). Particle Image Velocimetry (PIV) representing the reacting flow field of High Swirl Injector (c) and Low Swirl Injector (d), adapted from Johnson et al. [54]

1.2. Research Questions

There are numerous experimental studies available in literature about LSB [17] [19][23][53] [75]. However, there are not many numerical models especially addressing the flame flashback in LSB using numerical simulations. Therefore, this thesis focuses on better understanding the flame flashback in LSB, leading to the formulation of the following research questions.

- *What turbulence and combustion model are suitable to simulate combustion in LSB burner configuration at high hydrogen content*
- *What are the potential reasons for the flame to flashback in LSB with hydrogen-enriched fuels ?*

1.3. Thesis Outline

This thesis focuses on the numerical modelling of the combustion process in LSB in a turbulent flow with hydrogen-enriched fuel mixtures. Time-efficient Reynolds Averaged Navier Stokes (RANS) turbulence models are used in conjunction with the flamelet combustion model along with turbulent flame speed correlations (to close the overall reaction rate of the combustion process). The results obtained from the numerical modelling have been verified with the experimental measurements done at Lawrence Berkeley National Laboratory (LBNL) [19] [20].

In chapter 2, the flow governing equations and turbulent flows are discussed in general. Following that, the turbulence modelling approach used in RANS equations is discussed along with turbulence models. On top of that, the basic theory of laminar and turbulent premixed combustion is presented with the governing equations of combustion.

The chapter 3 deliberates about the significance and characteristics of swirl flows. Apart from that, the flame stabilization techniques employed to stabilize the flame are briefed. Following that, the literature study of the LSB is performed, where the difference between the HSI and LSI is analysed. Consequently, the flow and flame aerodynamics of LSB is studied. After that, combustion models used in modelling the turbulent premixed combustion are explained. Finally, the flashback mechanisms and the experimental observations identified from the literature are briefed.

The chapter 4 explains the computational setup of the model and the meshing techniques employed in this study for the numerical calculations reported in detail. In addition, the boundary conditions and the combustion parameters required for the simulations are presented.

The chapter 5 discusses the numerical validation of both non-reacting and reacting flows. Initially, the three-dimension mesh independence study was performed for non-reacting flows. Following that, the RANS turbulence models are evaluated with the experimental measurements of Cheng and Littlejohn [20] which answers the following sub-question of this thesis:

* **Determine the best RANS turbulence model which replicates the non-reacting low swirl flow features seen in experiments.**

After that, the numerical validation of reacting flow simulations is validated with the experimental measurements of Cheng et al. [19]. In addition, the flame positions are compared quantitatively with the experimental measurements of Cheng et al. [19] and the numerical simulations of Muppala et al. [87] for different fuel mixtures varying in vol.% of hydrogen using turbulent flame speed correlations. The hydrogen-enriched fuel mixtures are simulated for two different combustion models to answer the following sub-question of this thesis:

* **How does the reaction rates of hydrogen-enriched fuels vary due to the addition of an effective Lewis number ($\mathbf{Le_{eff}}$) in the turbulent flame speed closure model ?**

In chapter 6, the potential reasons for flashback occurrence in LSB are discussed elaborately. Based on the experimental and numerical understanding grasped from the literature and simulations, the prevalent mechanism of flashback in LSB is evaluated. Further, the numerical simulations of 'M' and 'V' shaped flames have been performed. Furthermore, the effects of the axial mass flow rate provided to the central channel of the LSI are investigated. Subsequently, the potential reasons for the flame flashback in LSB are analysed quantitatively based on the flow field of the premix nozzle. The above-mentioned analyses were performed to answer the final research question mentioned in section 1.2.

2

Theoretical Framework

This chapter is devoted to discussing the necessary theoretical, and fundamental concepts of fluid dynamics and combustion related to this research are discussed. Fluid flow governing equation and turbulence concepts are discussed in section 2.1 and 2.2. Following this, the basics of combustion physics appropriate to this study are presented.

2.1. Governing Equations

The mathematical equations that govern the fluid flow are the conservation equations of mass, momentum and energy. These conservation equations are derived based on Newton's second law of motion and mass conservation within the continuum limit. The differential form of continuity and Navier Stokes equations in a fixed frame of reference are:

$$\frac{\partial \rho}{\partial t} + \nabla \cdot (\rho \vec{u}) = 0 \tag{2.1}$$

$$\rho \frac{\partial \vec{u}}{\partial t} + \rho(\vec{u} \cdot \nabla)\vec{u} = -(\nabla p) + \nabla \cdot \bar{\bar{\tau}} + \vec{f} \tag{2.2}$$

Where $\vec{u}(\vec{x}, t)$ = (u, v, w), $\vec{x}$ = (x, y, z), ρ and $\bar{\bar{\tau}}$ are the velocity vectors, position vectors, density and viscous stress tensor of the fluid respectively in inertial frame of reference. The non linear momentum transport equation 2.2 consists of convective term $(\rho(\vec{u}\cdot\nabla)\vec{u})$ also known as inertial term, pressure term (∇p), viscosity diffusive term $(\nabla \cdot \bar{\bar{\tau}})$ and body or volume force term $(\vec{f})$. ∇ and ∇^2 are the gradient and the Laplacian operator defined in Appendix A. For incompressible and Newtonian fluids, the viscous stresses are proportional to strain rates with the constant of proportionality μ known as dynamic viscosity, which is the property of the fluid.

$$\tau_{ij} = 2\mu S_{ij} \tag{2.3}$$

$$S_{ij} = \frac{1}{2}\left(\frac{\partial u_i}{\partial x_j} + \frac{\partial u_j}{\partial x_i}\right) \tag{2.4}$$

From the above generalisation the equation 2.2 reduces to equation 2.5

$$\frac{\partial \vec{u}}{\partial t} + (\vec{u} \cdot \nabla)\vec{u} = -\frac{1}{\rho}\nabla \vec{p} + \nu(\nabla^2 \vec{u}) + \vec{f} \tag{2.5}$$

Where ν is the kinematic viscosity, it is the ratio of dynamic viscosity (μ) over density. Fluid motion with rotation or nearly circular streamline is known as vortex motion, the intensity of such vortex motions ($\vec{\omega}$) is measured by applying curl to the $\vec{u}$. The measure of $\vec{\omega}$ aids in assessing the flow fields of swirling flows, especially in swirl burners. Therefore, the vorticity vector is defined as the rotation of the vector field.

$$\vec{\omega} = \nabla \times \vec{u} \tag{2.6}$$

The $\vec{\omega}$ is divergence-free (see Appendix A), which is akin to a continuity equation with constant density, this implies the vorticity field is source free [96]. Similar to $\vec{\omega}$ definition, the transport equation of $\vec{\omega}$ for incompressible fluids can be derived by applying curl to the Navier Stokes equation 2.5 see Appendix A for derivation.

$$\frac{\partial \vec{\omega}}{\partial t} + (\vec{u} \cdot \nabla)\vec{\omega} = (\vec{\omega} \cdot \nabla)\vec{u} - \vec{\omega}(\nabla \cdot \vec{u}) + \frac{1}{\rho^2}(\nabla\rho \times \nabla p) + \nu\,(\nabla^2\omega) \tag{2.7}$$

The left side consists of convective and transient terms. The $(\vec{\omega} \cdot \nabla)\vec{u}$ is the term responsible for stretching and tilting of vortices, the stretching and tilting is a three-dimensional property and it is shown in Appendix A. $\vec{\omega}(\nabla \cdot \vec{u})$ is the expansion or dilatation term and $1/\rho^2(\nabla\rho \times \nabla p)$ is the baroclinic term, for constant density flows these two-term can be neglected from vorticity transport equation. But for reacting flows like combustion due to temperature jump there will be a change in density. Even though there is a change in density, the flow is still incompressible since the density does not vary with respect to pressure [109]. $\nu\,(\nabla^2\omega)$ is the diffusion term and it is mostly neglected in high speed flows. The velocity at a point due to $\vec{\omega}$ can be evaluated by employing Biot-Savart's law:

$$\vec{u}_{rot}(\vec{x}) = \frac{1}{4\pi}\int_V \frac{\vec{\omega}\,(\vec{x}') \times \vec{\vec{x}} - \vec{x'}}{|\vec{x} - \vec{x'}|^3} dV\,(x') \tag{2.8}$$

The velocity due to the rotational part at a point $\vec{x}$ can be calculated by evaluating the equation 2.8. Where $\vec{x} - \vec{x'}$ signifies the distance between the point $\vec{x}$ and the flow field $\vec{x'}$. To understand it better consider a vorticity concentrated volume V' as shown in figure 2.1, The velocity induced at a point $\vec{x}$ by the vorticity concentration located at a point $\vec{x'}$ can be calculated by integrating equation 2.8 over the volume V'.

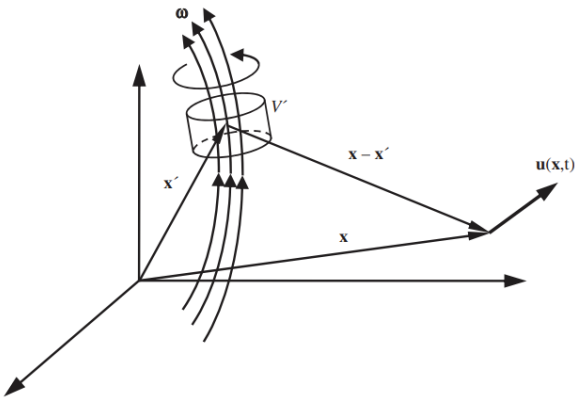

Figure 2.1: Geometrical representation of the Biot-Savart's law in arbitrary coordinate, from Ref.[66]

The equation 2.8 is derived based on the assumption that the flow is incompressible, that is $\nabla \cdot \vec{u} = 0$ [66]. But equation 2.8 is also used in many reacting flow studies [58] [14][62] .

2.2. Turbulent Flows

$$Re = \frac{uL}{\nu} \tag{2.9}$$

Theoretically, fluid flows are classified based on a non-dimensional parameter known as the Reynolds number, defined in equation 2.9, where L is the characteristic length of the flow. Flow is named to be turbulent if the flow acceleration dominates viscosity of the fluid. Whereas the viscosity dominated flow is termed as laminar flow. Turbulent flow is characterised by the presence of eddies or vortices which is responsible for the continuous fluctuations of velocity (u'). Initially, the turbulent flow was considered to be an inviscid flow since the viscous term was assumed to be negligible when compared to the inertial term. On the contrary, the turbulent flow should have a finite viscous effect to describe flow separation, and drag effects and no slip boundary at the fluid-solid interface. Therefore the fluid flow is divided into two regions, viscosity dominant and inertial dominant region; the line separating the two regions is called the boundary layer. The region far away from the wall is free from viscous effect, whereas the region near the wall is viscosity effected. The region near the wall is characterised by the length scale δ. δ is the boundary layer thickness (δ) with finite viscosity, defined in equation 2.10.

$$\delta = \frac{\nu x}{U_0} = L\sqrt{\frac{1}{Re}} \tag{2.10}$$

The equation 2.10 is derived from the scaling analysis of the 'x' momentum equation (coordinate axis along the flow direction) within the boundary layer. The x is the distance from the beginning of the boundary layer along the x axis, and U_0 or U_∞ is the mean velocity or free stream velocity. The boundary layer over a flat plate is illustrated in figure 2.2.

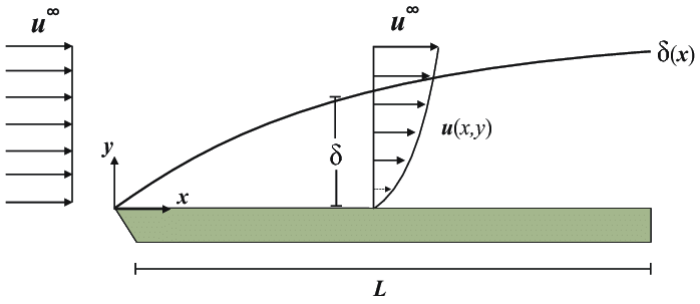

Figure 2.2: Boundary layer over a flat plate adopted from Ref.[104]

Initially, eddies are generated in the boundary layer due to the shear stress developed at the fluid-solid interface. Eddies are assumed to be a localised circular motion of fluid flow which has a flow direction different from the actual flow. Eddies have a wide range of temporal and spatial scales depending upon the diameter of the eddies and spinning velocity. These eddies advect and grow in size by taking energy from the core of the turbulent flow. In such a scenario, turbulent flow exhibits random fluctuations due to varying eddie sizes.

Eddies present in the turbulent flow posses energy levels known as Turbulent Kinetic Energy (TKE) depending upon the length scale of the eddies. The mean TKE produced by velocity fluctuations is defined by:

$$\overline{k} \equiv \frac{1}{2}\overline{u_i' u_i'} \tag{2.11}$$

The different scales in the turbulent flow are categorized as follows:

- **Large scale** or macro scale represents the characteristic dimension of the flow domain.
- **Integral scale** represents the size of the largest eddie in the flow. The size of the largest eddie solely depends upon the flow geometry
- **Taylor microscale** is the intermediate scale. From this scale, viscosity starts to affect the flow
- **Kolmogorov scale** is characterised by the size of a small eddie, where energy starts to dissipate

The TKE due to the various scales in turbulent flow is represented in wave number space $E(\kappa)$ for homogeneous isotropic turbulence in figure 2.3, where u_i' is equal in all directions. Then, the TKE defined in equation 2.11 reduces to equation 2.12

$$\overline{k} = \frac{1}{2}\overline{u_i'^2} \tag{2.12}$$

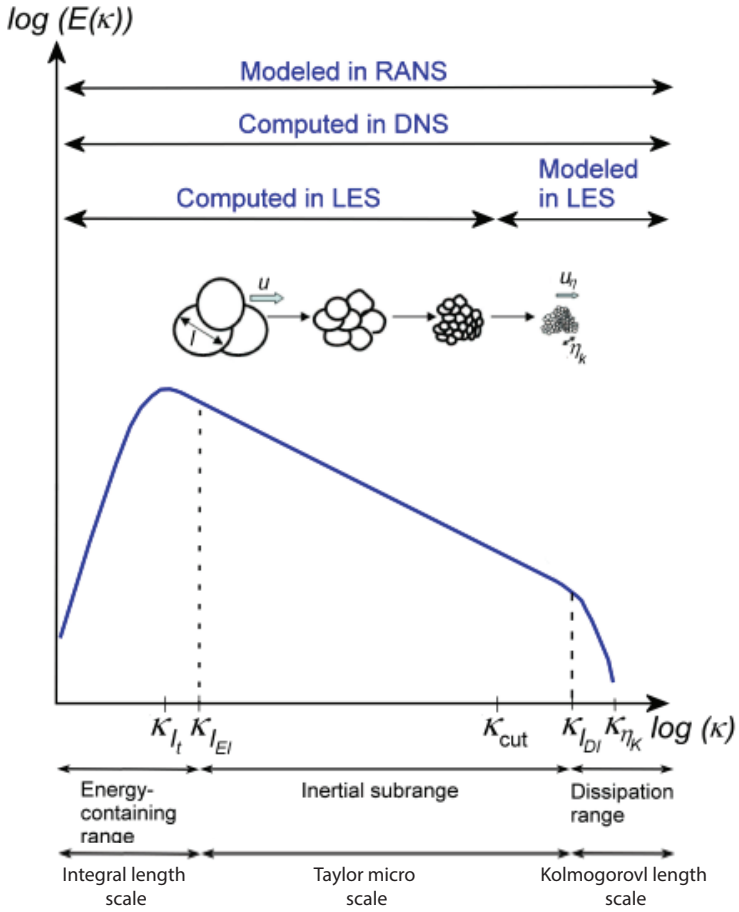

Figure 2.3: Energy spectrum of Turbulent Kinetic Energy (TKE) versus wave number for homogeneous and isotropic turbulence, adopted from Ref.[107]

2.2.1. Spatial and temporal scales in turbulence

The energy cascade theory of turbulence by Richardson [106] is used widely to analyse the magnitude of turbulent flow. Energy cascade theory states that for a homogeneous and isotropic turbulence, the large scale eddies get energy from the mean flow by vortex stretching [124]. Then, these large eddies or integral scale eddies (l_t) cascade down to smaller eddies known as Kolmogorov eddies (l_η). In the Kolmogorov regime, molecular diffusion starts to play a vital role as the order of magnitude of the scales can be estimated based on the molecular diffusion and turbulent dissipation rate (ϵ). Here, ϵ is defined as the rate at which viscosity converts TKE into thermal energy. According to the Kolmogorov hypothesis, the energy dissipation rate remains constant until it goes to the minimum Kolmogorov size [100]. From figure 2.3 it is seen that the larger eddies tend to have high energy. These high energy eddies transfer its energy to the successively smaller eddies.

By scaling analysis, various length and time scales along with non-dimensional numbers are summarised in table 2.1. First, the integral scales are discussed in detail. Integral length scale (l_t) is estimated by integrating the velocity autocorrelation function f as defined in equation 2.13. The velocity scale is obtained based on the Turbulent Kinetic Energy (TKE) per unit mass definition (equation 2.15). The time scale is obtained by scaling l_t with fluctuating velocity (u') as defined in equation 2.17. In addition to that, the Reynolds number specific to the integral length scale is also mentioned in equation 2.19.

Then, scales in the Kolmogorov range are considered. Since turbulent flows are heavily diffusive and dissipative, scales in the Kolmogorov range are developed based on the dimensions of diffusion (L^2/T) and dissipation (L^2/T^3). Depending on these dimensions, length, velocity and time scales (equation 2.14, 2.16 and 2.18) are constructed. Analogous to the integral scale, a specific Reynolds number is defined for the Kolmogorov scale in equation 2.20 and this is equal to unity since both the Inertial and viscous terms are equal in the Kolmogorov scale [32].

	Integral		kolmogorov	
Length	$l_t = \int_0^\infty f\, dr$	(2.13)	$l_\eta = \left(\frac{\nu^3}{\epsilon}\right)^{1/4}$	(2.14)
Velocity	$u' = \sqrt{2k}$	(2.15)	$u'_\eta = (\nu\epsilon)^{1/4}$	(2.16)
Time	$t_f = \frac{l_t}{u'}$	(2.17)	$t_\eta = \left(\frac{\nu}{\epsilon}\right)^{1/2}$	(2.18)
Non-dimensional number	$Re_{l_t} = \frac{u' l_t}{\nu}$	(2.19)	$Re_\eta = \frac{u'_{l_\eta} t_\eta}{\nu} = 1$	(2.20)

Table 2.1: Scales and non-dimensional numbers relevant to turbulent flows

2.3. Fluid flow calculation in RANS

The aforementioned length scales of eddies needs to be resolved or modelled to simulate turbulent flows with Computational Fluid Dynamics (CFD). Computational approaches used in the computation of turbulent flows are classified as RANS (Reynolds Averaged Navier Stokes), LES (Large Eddy Simulation), and DNS (Direct Numerical Simulation). The size of the cells needs to be smaller than the length scale of the eddies to compute turbulence, this method of computation is known as DNS, whereas in LES the eddies of Taylor micro scale are resolved and the eddies smaller than Taylor micro scale are modelled. Apart from employing smaller mesh sizes, there are various turbulence models available in the literature to model turbulence. RANS is more feasible and time efficient when compared to the other two computational methods. RANS was developed to solve the mean values of all flow parameters. The RANS equations are obtained by averaging the instantaneous equations. Since the turbulent flow is characterised by the presence of eddies and fluctuating flow parameters, it is convenient to analyse the flow by decomposing the turbulent flow into mean and fluctuating parts. This is done by Reynolds decomposition as defined in equation 2.21 for incompressible non-reactive flows. Analogous to Reynolds decomposition, Favre decomposition is employed in compressible and reactive flows. In equation 2.22 the density weighted average of quantitied is illustrated. $\tilde{U}$ is the Favre averaged flow velocity, and U'' is the fluctuating velocity around the Favre averaged flow velocity. Favre decomposition and averaging are applied to the instantaneous continuity equation to obtain mean continuity equation 2.24. Similarly, the Favre averaging of instantaneous Navier Stokes equation leads to equation 2.25.

$$u_i(\vec{x},t) = \overline{u_i(\vec{x},t)} + u''(x,t) \tag{2.21}$$

$$f = \tilde{f} + f'' \tag{2.22}$$

Where,

$$\tilde{f} \equiv \langle f \rangle = \frac{1}{n_{samples}} \sum_{n=1}^{n_{\text{samples}}} f_n \tag{2.23}$$

$$\frac{\partial \overline{\rho}}{\partial t} + \frac{\partial}{\partial x_i}\left(\overline{\rho}\tilde{u}_i\right) = 0 \tag{2.24}$$

$$\frac{\partial \overline{\rho}\tilde{u}_i}{\partial t} + \frac{\partial}{\partial x_j}\left(\overline{\rho}\tilde{u}_i\tilde{u}_j\right) = -\frac{\partial \overline{p}}{\partial x_i} + \frac{\partial \overline{\tau}_{ij}}{\partial x_j} + \overline{\rho}g_i - \frac{\partial}{\partial x_j}\left(\widetilde{\overline{\rho}u_i'' u_j''}\right) \tag{2.25}$$

Where, u_i is the velocity in i direction ($i = 1, 2, 3$). Comparing equation equation 2.2 and equation 2.25, an additional term, known as Reynolds stress tensor is present in the right end of equation 2.25. From the mass conservation of the velocity fluctuations it is evident that the Reynolds stress terms are positive which adds to the momentum equation. The Reynolds stress term is a symmetric tensor consisting of six independent components (R_{ij}). Accounting the continuity equation alongside the three momentum equations ($\tilde{u_i}$) and pressure ($\overline{p}$) there are a total of ten unknowns, this leads to the closure problem.

The Reynolds stress term is closed by the turbulent viscosity hypothesis, commonly known as the Boussinesq hypothesis [92]. The momentum transfer by the turbulent eddies is modelled by introducing eddy kinematic viscosity or turbulent viscosity(ν_T).The Reynolds stress tensor for incompressible flow is defined in the following way,

$$R_{ij} = -\rho\overline{u_i' u_j'} \simeq -\frac{2}{3}\rho k\delta_{ij} + 2\rho\nu_T\overline{S_{ij}} \tag{2.26}$$

Where k is the TKE and δ_{ij} is the Kronecker symbol, the momentum increase due to the fluctuations in turbulent flow is accounted by modelling ν_T using various two-equation models. The two additional equations are TKE and a form of eddy or turbulent dissipation. These equations are solved to close the Reynolds stress term. The equations of the two-equation models and their assumptions are discussed elaborately in Appendix B.

2.3.1. Near wall treatment and y+

Vortices or eddies are generated near the wall as a result of the no-slip boundary condition. For fully developed turbulent flow, turbulence is significantly affected in the near wall region due to the presence of the wall. The normal velocity fluctuations near the wall decrease as a result of no-slip boundary. To define the magnitude of velocity change (gradient) inside the viscous dominating boundary layer, a wall friction velocity (u_τ) and length scale smaller than δ is defined in equation 2.27 and 2.28 based on wall shear stress τ_w.

$$u_\tau^2 = \frac{\tau_w}{\rho} \tag{2.27}$$

$$\delta_\nu = \nu\sqrt{\frac{\rho}{\tau_w}} = \frac{\nu}{u_\tau} \tag{2.28}$$

$$\frac{\tau}{\rho} = -\overline{u'v'} + \nu\frac{\partial\overline{u}}{\partial y} \tag{2.29}$$

Where u_τ is the viscous scale velocity. In turbulence, the total shear stress normalized by ρ is a sum of Reynolds stresses ($-\overline{u'v'}$) and viscous stresses ($\nu(\partial\overline{u}/\partial r)$) as defined in equation 2.29. The relation expressed in equation 2.29 is derived from the scaling analysis of RANS equations for a fully developed stable turbulent flow. Based on this formulation, the boundary layer is divided into three different regions depending upon viscous and Reynolds's stress, they are:

- **Core region**: Otherwise known as outer region, Reynolds stresses dominate over viscous stresses. Hence only Reynolds's stresses are modelled by the models discussed in Appendix B
- **Wall region**: This is also known as the logarithmic wall layer or log law layer, where both the Reynolds stresses and viscous stresses are almost constant over the region
- **Viscous sublayer**: This region lies in close proximity to the wall where Reynolds stresses are considered to be negligible

Based on the assumptions made in different regions, the mean velocity profiles of outer region, logarithmic wall region and viscous sub layer can be obtained from the relations mentioned in table 2.2. To match the velocity profile of viscous sub layer and log law layer, an additional wall units 2.30 and 2.31 were introduced by normalising the velocity with viscous scale velocity. Based on the results of several experiments of turbulent channel flow, it was found that the velocity profile of viscous sublayer is valid till $y^+ = 5$ [92]. Therefore a new zone, known as the buffer zone ($5 < y^+ < 30$) connecting viscous sub layer and log law layer was introduced.

$$y^+ = \frac{y}{\delta_\nu} \tag{2.30}$$

$$u^+ = \frac{u}{u_\tau} \tag{2.31}$$

Location	Layer	Mean velocity
$y^+ < 5$	Viscous sublayer	$u^+ = y^+$
$5 < y^+ < 30$	Buffer layer	$\frac{1}{\kappa}\left[\ln\left(y^+ - l_v^+\right) + \Pi\right]$
$y^+ > 30$	Log law layer	$\frac{1}{\kappa}\left[\ln\left(y^+\right) + \Pi\right]$

Table 2.2: Velocity profiles of the inner Wall regions, from Ref.[92]

All three layers mentioned in the table 2.2 are collectively known as inner layers; see figure 2.4. The dominating viscous effect in the viscous sublayer, starts to lose its impact in the log law layer region. From the mean velocity profiles of all the three layers defined in table 2.2, it is evident that the mean velocity profile of the viscous sublayer is linear with the distance from the wall (y^+). Meanwhile, the mean velocity profile of buffer and log law layer is defined by displaced log law [48], where κ is the Von Karman constant equal to 0.4187, Π and l_v^+ are constants with value 2 and 6 respectively [92].

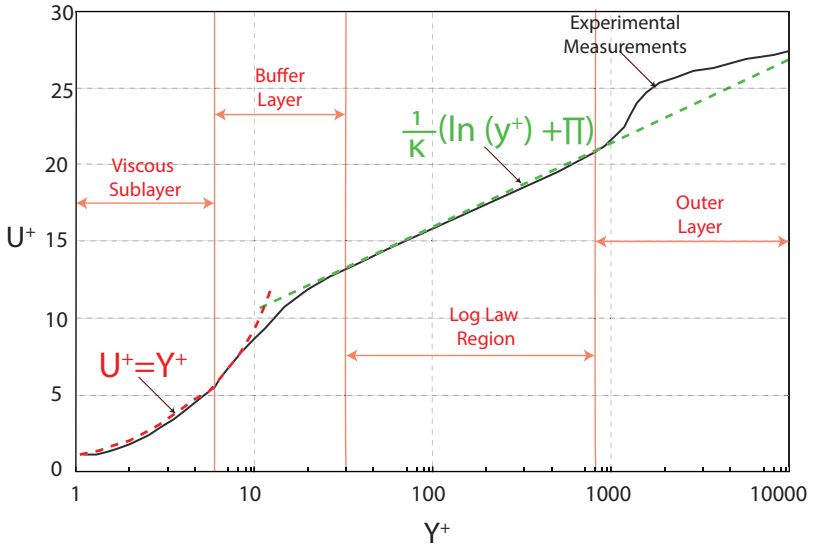

Figure 2.4: Wall function of different layers in dimensionless coordinates adopted from Ref.[1]

2.4. Combustion

A high temperature redox chemical reaction between fuel and oxidizer (air) is termed as combustion. A flame is produced as a result of fuel oxidation. Combustion is an exothermic reaction which produce heat and light energy along with other byproducts.

$$CH_4 + 2\,O_2 + 2 * 3.76\,N_2 \rightarrow CO_2 + 2\,H_2O + 2 * 3.76\,N_2 \tag{2.32}$$

$$H_2 + 0.5\,O_2 + 0.5 * 3.76\,N_2 \rightarrow H_2O + 0.5 * 3.76\,N_2 \tag{2.33}$$

Reactions 2.32 and 2.33 represents a methane and a hydrogen combustion reaction that takes place in combustor under stoichiometric conditions, respectively. Nature of the combustion is defined by the parameter knows as equivalence ratio (ϕ). ϕ is the ratio of actual fuel-air ratio to stoichiometric fuel-air ratio.

$$\phi = \frac{\left(\frac{X_{fuel}}{X_{air}}\right)}{\left(\frac{X_{fuel}}{X_{air}}\right)_{st}} \tag{2.34}$$

Where X is the mass fraction. Combustion is broadly classified into three types based on how fuel-oxidizer interaction takes place [81], they are listed below:

- **Premixed combustion:** When the fuel and oxidiser are mixed prior to the combustion, a homogeneous mixture is delivered to the combustion chamber. A reaction controlled premixed flame is produced when the mixture is well mixed. The mixture is said to be rich when ϕ >1 and lean when ϕ <1
- **Non-premixed combustion:** Where the fuel and oxidiser are fed separately and mixing takes place inside the combustor to produce diffusion controlled diffusive flame
- **Partially Premixed Combustion:** Partially premixed mixtures produce partially premixed flame (PPF) which is a combination of both premixed flame and diffusion flame which takes place due to insufficient mixing. PPF has different thermodynamical states locally within the flame [80]

Incoming flow in the combustion chamber can either be laminar or turbulent based on the flow properties, which are discussed in upcoming sections.

2.4.1. Governing equations for combustion modeling

Since combustion is associated with many species and enormous heat release, transport equations of species and energy are also required in addition to mass and momentum equations to model combustion. These equations are derived based on a low Mach number approximation since the fluid velocity and flame velocity are smaller than the speed of sound. This assumption leads to the decoupling of dynamic pressure, and only the background pressure P_0 is taken into account [8] and the fuel is said to obey the ideal gas law as defined in equation 2.35.

$$\rho = \frac{P_0 \overline{M}}{R_u T} \tag{2.35}$$

Where M is the molecular weight of the mixture and $R_u = 8.314\,J/mol$ is the universal gas constant. The species conservation equation described in equation 2.36 gives information about the evolution of different species involved in combustion.

$$\frac{\partial}{\partial t}\rho Y_k + \frac{\partial}{\partial x_i}\left(\rho Y_k \vec{u_i}\right) = -\frac{\partial}{\partial x_i}\left(\vec{J_k}\right) + \dot{\omega}_k, \qquad \text{for} \qquad k = 1, \ldots, N \tag{2.36}$$

Where k is the species index, Y_k is the mass fraction, and $\vec{u_i}$ is the mixture velocity vector. Unlike mass conservation, species mass can not be conserved with convective and diffusive fluxes since the species can either be consumed or produced in combustion; hence production rate ($\dot{\omega}_k$) is modelled separately to account for the changes due to the chemical reactions. The first term on the left-hand side is the unsteady term, and the second term accounts for the convective flux. The first term on the right-hand side, which accounts for diffusion, needs to be modelled by using diffusion models like generalised Fick's law as given in equation 2.37.

$$\vec{J_K} = \rho_k \vec{U_K} = -\rho D_{i,j} \nabla \vec{Y_i} - D_{T,k} \frac{\nabla T}{T} \tag{2.37}$$

Where $\vec{U_k}$ is the diffusion velocity vector, $D_{i,j}$ is the binary mass diffusivity of species i with respect to the species j in the mixture and $D_{T,k}$ is the Soret diffusion coefficient. The last term in equation 2.37 accounts for the temperature diffusion (Soret effect) due to gradients of temperature. Mostly, the Soret effect is assumed to be negligible. The species transport equation after incorporating Fick's law is defined in equation 2.37 as follows,

$$\frac{\partial}{\partial t}\rho Y_k + \frac{\partial}{\partial x_i}\left(\rho Y_k \vec{u_i}\right) = \frac{\partial}{\partial x_i}(\rho D_{i,j} \frac{\partial Y_k}{\partial x_i}) + \dot{\omega}_k, \qquad \text{for} \qquad k = 1, \dots, N \tag{2.38}$$

The transport equation of total energy (e) is represented in equation 2.39.

$$\frac{\partial}{\partial t}\rho e + \frac{\partial}{\partial x_i}\rho e \vec{u} = -\frac{\partial}{\partial x_i}\left(\vec{j_q} + \overleftrightarrow{\sigma} \cdot \vec{u}\right) + s_e \tag{2.39}$$

Where e is the total energy which is a sum of internal energy, kinetic, gravitational potential [126]. $\vec{j_q}$ is the diffusive energy flux which is due to the contribution of three different fluxes: temperature gradient ($\vec{q}_{conduction}$), species diffusion ($\vec{q}_{inter\,diffusion}$) and different diffusion velocity ($\vec{q}_{Dufour}$). In combustion, the Dufour effect due to different diffusion velocities is more often neglected [126]. $\overleftrightarrow{\sigma} \cdot \vec{u}$ is the energy flux due to stress in the fluid, and this is of much smaller magnitude when compared to the enormous amount of energy released during combustion, so it is neglected. Other forms of energy unaccounted in the total energy are taken care by introducing the energy source or sink term s_e.

$$\vec{q}_{conduction} = -\lambda \frac{\partial T}{\partial x_i} \tag{2.40}$$

$$\vec{q}_{interdiffusion} = \sum_{k=1}^{N} \rho h_k Y_k \vec{U}_k = -\rho D_{i,j} h_k \frac{\partial \vec{Y}_k}{\partial x_i} \tag{2.41}$$

The diffusive heat flux through conduction is defined by Fourier's law of heat flux, where λ is the thermal conductivity of the mixture and h_k in equation 2.41 is the species enthalpy. The inter diffusion heat flux is modelled by Fick's law similar to 2.38. After considering these assumptions the simplified energy equation is given as follows,

$$\frac{\partial \rho e}{\partial t} + \frac{\partial}{\partial x_i}\left(\rho u_i e\right) = -\frac{\partial}{\partial x_i}\left(-\lambda \frac{\partial T}{\partial x_i} + \sum_{k=1}^{N} -\rho D_{i,j} h_k \frac{\partial \vec{Y}_k}{\partial x_i}\right) + s_e \qquad \text{for} \qquad k = 1, \dots, N \tag{2.42}$$

Energy conservation equation can be represented in various forms and these equations can be found in textbooks by Williams [130] and Kuo [67]. From the energy conservation equation, conservation equation for enthalpy can be derived from $e = h + P/\rho$. After assuming negligible viscous dissipation and neglecting the transient pressure term the transport equation of enthalpy is represented as,

$$\frac{\partial \rho h}{\partial t} + \frac{\partial}{\partial x_i}(\rho u_i h) = -\frac{\partial}{\partial x_i}\left(-\lambda \frac{\partial T}{\partial x_i} + \sum_{k=1}^{N} -\rho D_{i,j} h_k \frac{\partial \vec{Y}_k}{\partial x_i}\right) + s_e \qquad \text{for} \qquad k = 1, \ldots, N \quad (2.43)$$

Solving turbulent reacting flow involves a lot variables and species so to reduce the computational cost whilst maintaining accuracy, various simplifications are introduced; they are reduced chemistry, flamelet hypothesis and statistical approach. These three methods are employed together or separately to reduce the computation cost considerably. The Favre averaged RANS equation specific to reacting flows, and their closure models are discussed in chapter 3.

2.5. Laminar premixed combustion

Initially, Friedman and Burke [39] studied the laminar flame structure and divided the flame zone into preheat and reaction zone. The figure 2.5 shows the schematic representation of laminar premixed flame obtained based on solving the one-dimensional, steady state and adiabatic mass and momentum conservation equations with single-step chemistry.

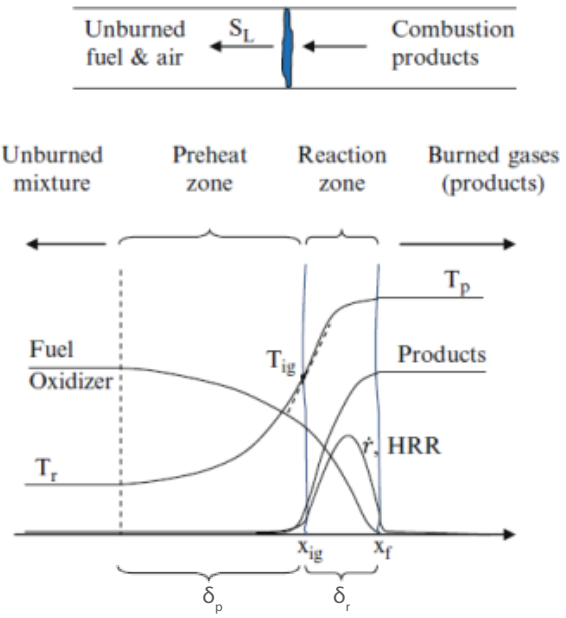

Figure 2.5: Premixed flame propagation adopted from Ref.[15]

When the premixed unburned mixture flows into the combustion chamber, reactions occur after the ignition temperature (T_{ig}) is attained. As a result of ignition, a bright luminous flame front is established where reactants are changed into products. The temperature increases monotonously from the initial unburned mixture temperature (T_r) to that of the burned mixture (T_p). While the initial reactants are consumed, intermediate species are formed in the reaction zone and then these species are oxidized to form final products. The heat and species diffusion take place in between the reaction and the preheat zone. The thickness of the flame (δ_f) is a sum of preheat zone and reaction zone thickness and is also defined as stated in 2.44 [99]. In the flame front, heat is transferred from the reaction zone to preheat zone to keep the flame self-sustaining. Whereas mass transfers (radicals) in the opposite direction.

$$\delta_f \equiv \frac{\nabla T_{\max}}{T_{\mathrm{r}} - T_{\mathrm{p}}} \tag{2.44}$$

The velocity associated with mass crossing the flame front is known as laminar flame speed (S_L^0). S_L^0 is a fundamental property of premixed mixture, which is defined as the relative velocity between the flame and the incoming unburned mixture. S_L^0 is a function of inlet temperature (T_0), inlet pressure (P_0), equivalence ratio (ϕ) and the fuel itself. For lean premixed mixtures S_L^0 increases with increasing ϕ; this is due to the high reaction rate as a result of high Adiabatic Flame Temperature (AFT). Varying T_0 and keeping AFT constant also show the same increasing behaviour of S_L^0 which is attributed to the increased diffusion rates in preheat zone. The effect of P_0 on S_L^0 can't be generalised for all the fuels, unlike T_0. For example, in the case of methane increasing P_0 increases the overall reaction rate, but in high hydrogen content mixtures (syngas), pressure has a non-monotonous behaviour on the overall reaction rate. The S_L^0 is directly proportional to δ_f and inversely proportional to the overall reaction rate. Another important parameter which influences S_L^0 is the rate of mass and heat diffusion. The rates of heat and mass diffusion in the flame front are quantified by the Lewis number (Le). Le of a particular species in a mixture is defined in equation 2.45.

$$Le_k = \frac{\alpha_k}{D_{i,j}} = \frac{\lambda_k/\rho_k C_{p,k}}{D_{i,j}} \tag{2.45}$$

where α_k and $C_{p,k}$ are the heat diffusivity and specific heat at a constant pressure of the species k. By assuming the S_L^0 equal to the unburnt mixture flow velocity and with Rankine-Hugoniot relations [69] for one-dimensional flame, aids in understanding the back pressure generated by the premixed flame.

$$\rho_u u_u = \rho_b u_b = \rho S_L^0 \tag{2.46}$$

$$\rho_u u_u^2 + p_u = \rho_b u_b^2 + p_b \tag{2.47}$$

Where 'u' and 'b' subscript signifies the unburnt and burnt state. From equation 2.46 and 2.47 the relation for the back pressure generated by the premixed flame is given as follows,

$$\Delta p = \rho_u (S_L^0)^2 \left(\frac{\rho_u}{\rho_b} - 1\right) = \rho_u (S_L^0)^2 \left(\frac{T_p}{T_r} - 1\right) \tag{2.48}$$

$$\Omega = \frac{T_p}{T_r} \tag{2.49}$$

The one-dimensional laminar flame discussed above is just a generalisation of an ideal laminar flame front, but in reality, the flame will have velocities in the other two directions moreover the flow will be turbulent. Then S_L^0 in equation 2.48 is replaced by Turbulent flame speed (S_T) which is discussed in the further sections.

$$\Delta p = \rho_u (S_L^0)^2 \left(\frac{\rho_u}{\rho_b} - 1\right) = \rho_u (S_T)^2 (\Omega - 1) \tag{2.50}$$

Typically, S_T will be ten times greater than S_L^0. Hence, in equation 2.48 flame speed is more dominant than the density jump. In turbulent flows, the eddies will tend to wrinkle and stretch the flame. The role of stretch in premixed flame front is discussed elaborately in the next section.

2.5.1. Flame stretch and preferential diffusion

The planar, unstretched flame is an ideal flame, and the speed associated with it is known as unstretched laminar flame speed S_L^0. In most real cases, the flame front is curved, wrinkled and stretched, and they can affect flame speed. The flame stretch is characterised by a stretch rate κ. κ is defined by Williams 1975 as the Lagrangian time derivative of the flame area of an infinitesimal element on the flame surface, and mathematically it is represented in equation 2.51. Stretching of the flame happens due to the surface gliding of the point in the flame induced by the tangential velocity of the flow, the unsteady flame in the flow and curvature of the flame [69].

$$\kappa = \frac{1}{A}\frac{DA}{Dt} \tag{2.51}$$

The mathematical representation of flame stretch defined in 2.52 denotes the contribution to flame stretch by flow non linearity, flame motion and flame curvature [69].

$$\kappa = \nabla_t \cdot \vec{u}_t + (\vec{u}_F \cdot \vec{n})\,(\nabla \cdot \vec{n}) \tag{2.52}$$

Where $\vec{u}_t$ is the tangential flow velocity, $\vec{u}_F$ is the flame surface velocity, ∇_t is the Lagrangian tangential derivative and $\vec{n}$ is the unit normal vector of the flame surface. The first term in equation 2.52 is known as the hydrodynamic stretch, which denotes the stretch due to the effect of non-uniform tangential flow velocity and the second term in equation 2.52 is known as the unsteady term, which signifies the impact of flame motion ($\vec{u}_F$) and flame curvature ($(\nabla \cdot \vec{n})$.

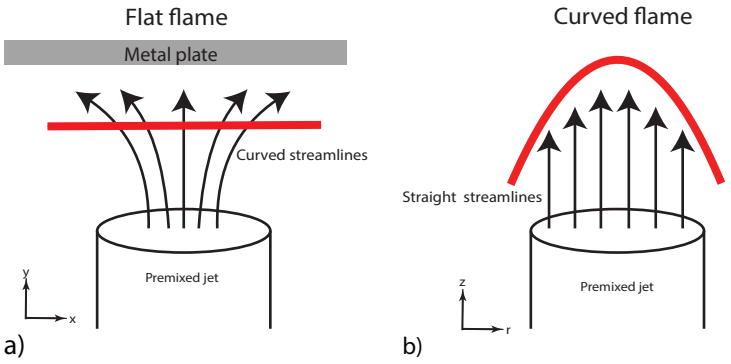

Figure 2.6: Flame stretch in divergent and uniform flow field adopted from [71]

The figure 2.6 (a) and (b) depict the flame in the divergent and uniform flow field, which produces a stationary planar flame in stagnation flow and Bunsen flame, respectively. From the figure 2.6 (a), it is evident that the flame is anchored at the position where the local flow speed is equal and opposite in direction. Due to the divergent flow field, the flame gets stretched radially outward due to the increased radial velocity. This is known as a positively stretched flame. The velocity vector of the diverging flow field is given below

$$\vec{v} = \{ax, -ay, 0\} \tag{2.53}$$

Since it is a stationary flame $\vec{u}_F$ equal to zero and equation 2.52 simplifies to $\kappa = a$ which denotes that for a stationary flame in stagnation flow the flame stretch is positive. A similar kind of analysis can also be done for Bunsen flame with velocity and normal unit vector given below,

$$\vec{v} = \{0, 0, -w\} \quad , \quad \vec{n} = \{-cos\alpha, 0, sin\alpha\} \tag{2.54}$$

where α is the flame cone angle. Upon using the equation 2.52 the flame stretch simplifies to equation 2.55 assuming w and α as constants.

$$\kappa = \frac{-w\ sin\ 2\alpha}{2R_f} \tag{2.55}$$

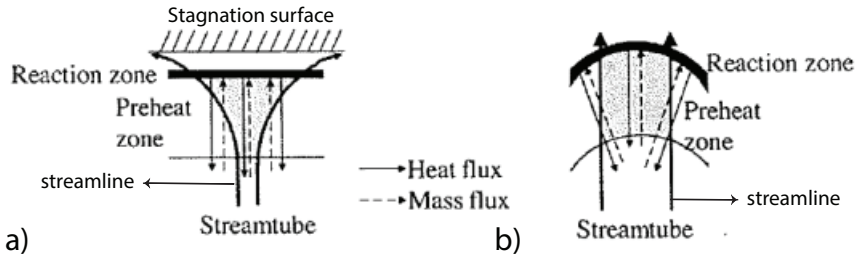

Figure 2.7: Flame stretch in divergent and uniform flow field adopted from [71]

It is evident that flame in figure 2.7 (a) which experience tension is positively stretched and flame in figure 2.7 (b) is negatively stretched. The above discussion only hold for stationary flames, that is $\vec{u}_F$ equal to zero. Markstein [101] found the linear relation between the flame speed and stretch and is expressed below:

$$\frac{S_L}{S_L^0} = 1 - l_m\kappa \tag{2.56}$$

$$\mathrm{Ma} = \frac{l_m}{\delta_f} \tag{2.57}$$

$$\mathrm{Ka} = \frac{\delta_f \kappa}{S_{L,0}} \tag{2.58}$$

Where, S_L is the stretched laminar flame speed and l_m is the Markstein length. The last term in equation 2.56 is usually represented by two non-dimensional numbers defined in equation 2.57 and 2.58. For an ideal case with zero stretch the equation 2.56 simplifies to S_L = S_L^0. The sign of the Markstein length depends upon the fuel reactivity to stretch. For a positively stretched flame, fuels responding with increased reactivity has positive l_m, whereas fuel responding with decreased reactivity has negative l_m. The vice versa is true for negatively stretched flames.

Sung et al. [119] reported the effect on flame speed and reactivity due to different rates of diffusivity of mass and heat (preferential diffusion) with respect to their stretch. Lewis number aids in understanding these effects on flame speed. The figure 2.7 depicts the two flow configurations with a grey surface indicating the control volume of the preheat zone and the streamlines of a stream tube. By performing an energy balance of the control volume the preferential diffusion effects on flame speed are studied. For steady-state idealized premixed flame and assuming no reaction occurring in preheat zone the energy balance equation from 2.43 reduces to equation 2.59.

$$\frac{\partial}{\partial x_i}\left(\rho u_i h\right) = -\frac{\partial}{\partial x_i}\left(-\lambda\frac{\partial T}{\partial x_i} + \sum_{k=1}^{N} -\rho D_{i,j} h_k \frac{\partial \vec{Y}_k}{\partial x_i}\right) \qquad \text{for} \qquad k = 1, \ldots, N \tag{2.59}$$

The term on the left-hand side is the convective flux where no flux flows across the stream tube, and the term on the right-hand side is diffusive fluxes of heat and mass, respectively. In figure 2.7 (a) the heat flux goes out of the control volume and for figure 2.7 (b) the heat flux comes into the control volume through their lateral surfaces. Therefore there is an increase or decrease in enthalpy depending upon stretch. This enthalpy change is balanced by diffusive mass flux for unit Lewis number mixtures, therefore no change is flame speed or flame temperature is observed [71]. But for non-unit Lewis number, the flame speed and temperature are affected depending upon the stretch type and Lewis number; they are summarised in table 2.3.

Flame type	Planar flame (positively stretched)	Curved flame (negatively stretched)
$Le > 1$ $\alpha > D$	The heat flux goes out of the C.V at a faster rate, hence the local Flame temperature decreases below the AFT which in turn decreases the flame speed	Since more heat flux is gained than mass flux the heat diffusion is greater than mass diffusion. Hence, local temperature will be grater than the AFT, thus the flame speed
$Le < 1$ $\alpha < D$	Mass diffusion dominates over heat diffusion, mass flux comes into the C.V. Resulting in local increase in ϕ. Hence, flame temperature increases over adiabatic flame temperature leading to increase in burning velocity S_d	The highly diffusive component (H_2) diffuses faster outside the the C.V, resulting in local lean region. This decrease the flame temperature less than AFT, that is the heat diffusion effect is less than mass diffusion. Hence, local temperature and flame speed decreases

Table 2.3: Summary of preferential diffusion effects on AFT and flame speed

To summarise, flame stretch is an important parameter that influences the flame speed, especially in a specific combustion regime known as the flamelet regime.

2.6. Flame front instabilities

So far the premixed flame was assumed to be stable, however, in the real case scenario, the premixed flame is subjected to instabilities like hydrodynamic instability and thermo-diffusive instability when the planar flame is perturbed. Therefore, hydrodynamic flame instability and thermo-diffusive flame instability will be discussed in subsection 2.6.1 and 2.6.2.

2.6.1. Hydrodynamic flame instability

Hydrodynamic instability is due to the interaction of the flame front with the flow. Assume a perturbed flame front which is thin and propagating with a constant S_L^0 as shown in figure 2.8. Upon perturbation, the flame front is bulged convex and concave towards the reactants. Due to the density discontinuity, the convex part of the flame front increases the area of the incoming stream tube. This causes the incoming flow to slow down before the flame front. Therefore, high pressure is created before the flame front. The converse effect is true for the concave part of the flame front.

The high and low pressure before the flame front paves the way for the flame front to move upstream (convex) and downstream (concave) with respect to the flow leading to unstable flame.

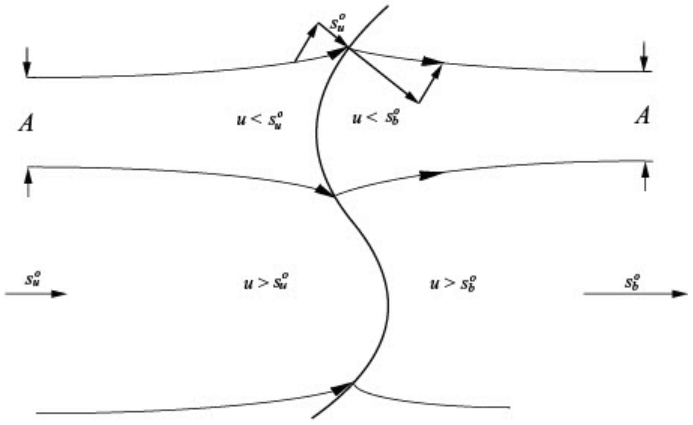

Figure 2.8: Schematic illustration of flame and flow interaction due to hydrodynamic flame instability adopted from Ref.[68]

2.6.2. Thermo-diffusive instability

Thermo-diffusive instability occurs when the heat conduction upstream to the reactants and reactants diffusion downstream to the flame front does not occur over the same length scale. Upon perturbation, the flame front is stretched positively (convex) and negatively (concave). For the premixed mixture with positive Markstein length l_m (positive Ma), the flame speed increases for negatively stretched flame and decreases for positively stretched flame due to the consequence of the non-unity Lewis number. This damps out the perturbation and stabilizes the flame as seen in figure 2.9 (b). This kind of intrinsic stabilization mechanism is seen in most hydrocarbon flames [68]. But, in the case of hydrogen-enriched fuels with negative Ma, the flame speed increases for positively stretched flame and decreases for negatively stretched flame leading to flame instability as seen in figure 2.9 (a).

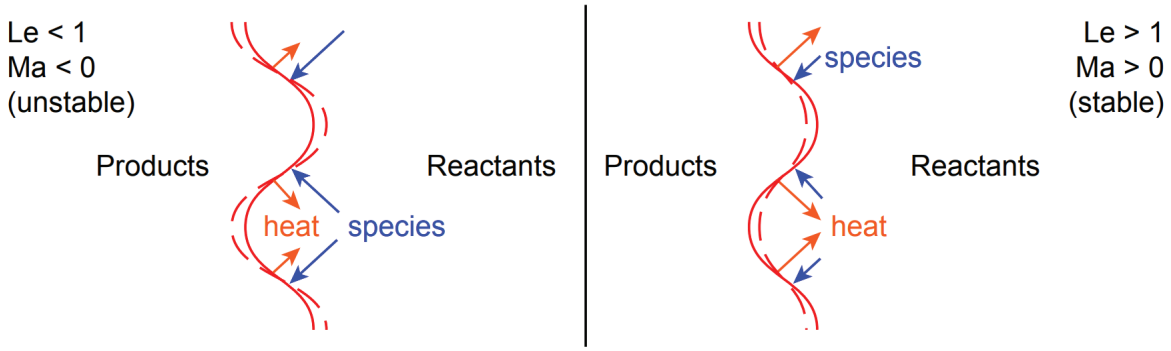

Figure 2.9: Schematic Illustration of thermal-diffusive instability for $Le < 1$ (a) and $Le > 1$ (b), adopted from Ref.[26]

2.7. Turbulent premixed combustion

Turbulent phenomena are exploited in combustion to increase mixing, reactivity, and efficiency. In many laboratory research, perforated plates are used to generate turbulence [116] [85] [10]. When the flame encounters turbulent flow, the laminar flame structure is replaced by regimes where turbulence and combustion interact. In combustion, since a large number of chemical reactions take place within the flow, a large range of temporal scales are present, ranging from nanosecond to second in addition to turbulence temporal and spatial scales [126].

Turbulence flame regimes are classified by Borghi and Peters [11] [97] based on non-dimensional numbers obtained by scaling analysis. The flow and chemical time scales used for the scaling analysis are defined in table 2.1 and table 2.4 respectively. Identification of an appropriate regime is necessary to model the reaction process. These diagrams are constructed based on the following assumptions; isotropic turbulence, adiabatic, unit Lewis and Schmidt number ($Sc = \nu/D_{i,mix}$). The concept of this diagram is based on the size of eddies and δ_f. If the eddies size is larger than δ_f, then eddies have no room to penetrate the flame; they end up stretching and wrinkling the flame. This is known as the flamelet concept where the turbulent flame can be modelled as a collection of stretched laminar flamelets with local flame speed S_L^0. Conversely, if the size of the eddie is smaller than the flame thickness, then the eddie will penetrate the reaction zone and distort the flame and time scale, which is known as the non-flamelet region. The line separating the flamelet and non-flamelet region is based on Klimov and Williams criterion [129]. The interaction between the flame front and turbulence is characterised by Damköhler number (Da) and Karlovitz number (Ka). Da number is defined as a ratio of turbulent integral time scale and chemical time scale (equation 2.60). A second Damköhler number (Da_η) is also defined similarly based on Kolmogorov time scale (equation 2.63). The Karlovitz number is simply the reciprocal of Da_η as seen in equation 2.64. The different lines in the figure 2.10 set the boundaries between various premixed combustion regimes.

Combustion		
Length	$\delta_f = \frac{\nu}{S_L^0}$	(2.60)
Velocity	S_L^0	(2.61)
Time	$t_{chemical} = \frac{\nu}{S_L^0}$	(2.62)
Non-dimensional numbers	$\mathrm{Da}_{l_t} = \frac{t_f}{t_c}$ (2.63)	$\mathrm{Da}_{l_\eta} = \frac{t_\eta}{t_f} = \frac{1}{Ka}$ (2.64)

$$\frac{t_{l_t}}{t_\eta} = Re_{l_t}^{1/2} = DaKa \; ; \quad Ka = \left(\frac{\delta_f}{l_\eta}\right)^2 \; ; \quad Re_t/Da_t = \left(\frac{u'}{S_L^0}\right)^2 \; ; \quad Re_t Da_t = \left(\frac{l_t}{\delta_f}\right)^2$$

Table 2.4: Scales and non-dimensional numbers related to Combustion

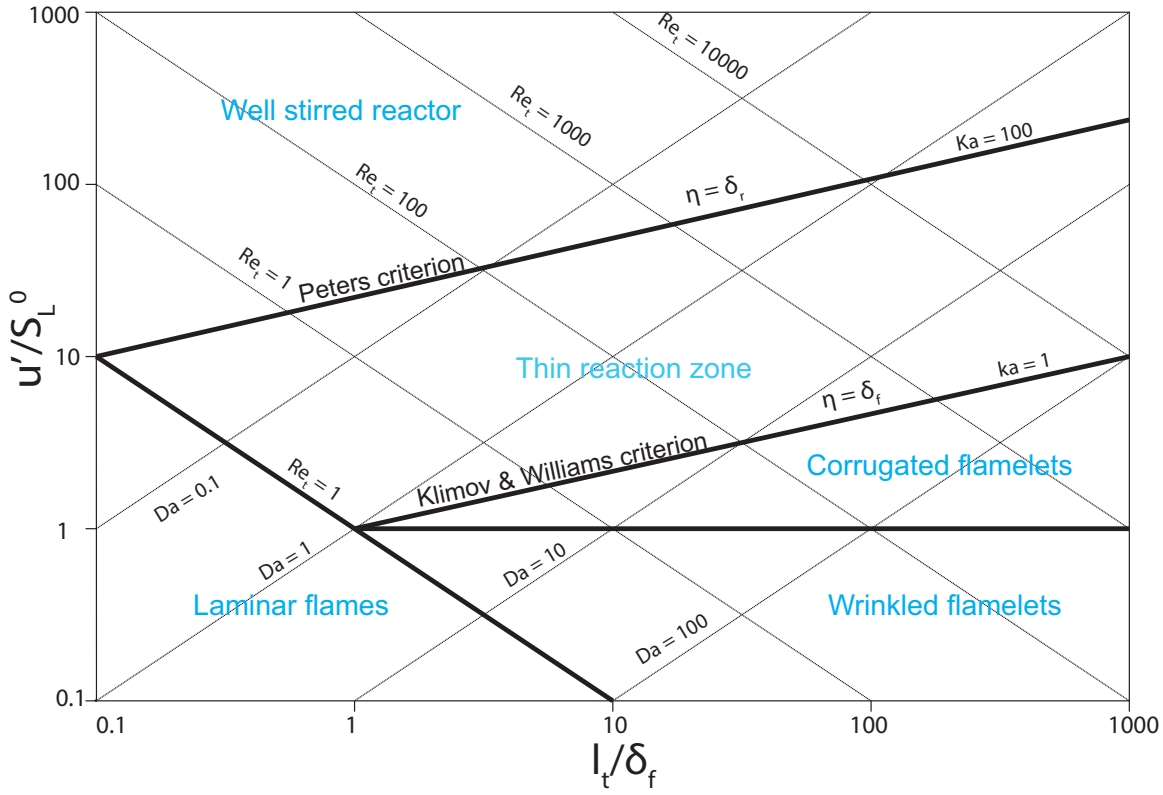

Figure 2.10: Borghi's and Peter's combustion regime diagram, adapted from Ref.[11][99]

Later, Peters postulated that even if the eddies are smaller than δ_f, the eddies will enter into the preheat zone and expand it [97]. Based on his postulate a different regime where the broad preheat zone exists is known as the thin reaction zone. The boundary separating a well-stirred reactor and thin reaction zone is known as peters criterion Ka_{δ_r} =1, this also corresponds to Ka =100. Ka_{δ_r} is defined as the ratio of reaction zone thickness to the Kolmogorov length scale. Borghi-Peters diagram is used to characterize different combustion regimes as depicted in figure 2.10.

Combustion regimes of turbulent premixed combustion are summarized in table 2.5. The figure 2.11 pictures the flame and turbulence interaction of different flame regimes.

$Ka < 1$	$Ka > 1$	$Ka > 100$
Flamelets	Thin reaction zones	Broken reaction zones
Flame thickness is smaller than turbulent eddies and they can't penetrate into flame. These flamelet region is further divided into wrinkled flamelets ($u' \approx S_L^0$) and corrugated flamelets ($u' > S_L^0$)	Small scale turbulent eddies penetrate into the preheat zone and enlarge the flame thickness	Reaction is the rate-limiting step since turbulence is much faster than reaction. Turbulence mixes like a well-stirred reactor

Table 2.5: Summary of turbulent premixed combustion regimes

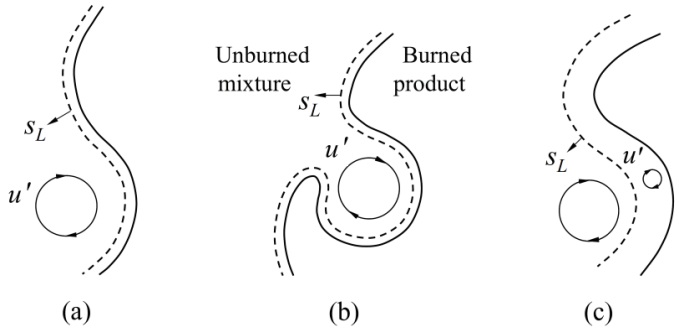

Figure 2.11: (a) Wrinkled flame, (b) Corrugated flame 4, (c) Thin reaction zone, from Ref.[68]

2.7.1. Turbulent flame speed

Turbulent flame speed (S_T) is defined as the average conversion rate of reactants into products. S_T is an important parameter because it is used to evaluate the operational metrics of the combustor. In contrast to S_L^0, S_T is not a physio-chemical and chemical kinetic property but it is a function of the turbulence in the flow and combustor geometry [42]. The S_T also has a direct impact on the flame length, which in turn affects the thermal loading of the combustor.

Damköhler's first hypothesis [28] states that when the turbulent scale (l_t) is greater than the flame thickness i.e in flamelet regime, the burning rate takes place in proportion with the flame surface area generation. Based on this hypothesis, the following relations can be derived from mass conservation.

$$\rho_u S_T A = \rho_u S_L A_T \tag{2.65}$$

Where A is the area of the approach flow and A_T area of turbulent flame brush. Assuming S_L to be constant over the flame, equation 2.65 can be rearranged into the following form

$$\frac{S_T}{S_L} = \frac{A_T}{A} \tag{2.66}$$

According to Damköhler, the interaction between the flame and flow is purely kinematic [28]. From this assumption, the area ratio can be approximated as follows,

$$\frac{A_T}{A} = \frac{S_T}{S_L} \approx \frac{u'}{S_L} \tag{2.67}$$

Based on the equation 2.67, Damköhler suggested a simple correlation for S_T

$$S_T = u' + S_L \tag{2.68}$$

From equation 2.68 it is evident that u' is dominant over S_L. If $u' >> S_T$ (distributed reaction regime) then, S_T will depend majorly on u'. Hence, different fuel won't make any difference. based on equation 2.68 many empirical correlation's are derived which is of the general form (equation 2.69),

$$\frac{S_T}{S_L} = A + B\left(\frac{u'}{S_L}\right)^n \tag{2.69}$$

where A, B and n are determined based on experimental data. There are innumerable correlations available in literature [73] for S_T, these correlations are used to model the mean chemical source term of the premixed combustion governing equation that is discussed elaborately in subsection 3.4.6.

3

Literature Review

In this chapter, the flow field topology of reacting and non-reacting swirling flows are discussed followed by the experimental investigations performed on Low Swirl Burner (LSB) so far are discussed along with their findings. In addition, the combustion models relevant to the study and their assumptions are also presented in detail. Finally, the flashback mechanism and the numerical studies specific to Low Swirl Injector (LSI) geometry are reviewed.

3.1. Swirl flow

Flows with a swirl velocity component (tangential or azimuthal) are termed as swirling flows. Swirling flows are characterised by their complex flow features, which are discussed in the following sections. Swirling flows are employed in many combustion systems due to their unique characteristics like flame stability, enhanced mixing, clean combustion and heat transfer rate. Generally, swirl flow can be generated by using one of the methods specified by Gupta et al. [45]. The tangential injection and vanes are often widely used to create swirl flows. Specifically, in gas turbine combustors, the annular pipe containing a set of swirler vanes at a specific angle is used to deflect the axial flow to create rotation in the flow.

The vanes of the swirler may be flat or curved. The profile of the vanes is usually flat because of their ease in manufacturing compared to curved vane profiles. However, curved vanes create high turbulence than flat vanes, and it is preferred in some cases because of their aerodynamic benefits [70]. The vane swirlers are classified depending upon the direction of fluid flow, they are axial and radial swirler. The sketch of axial and radial swirler are shown in figure 3.1. The flow field produced by the two swirlers will be almost the same [57]. According to Gupta et al. [45], axial vane swirler has low efficiency than tangential entry swirler in creating a swirl. Radial swirler results in high-pressure loss when compared to axial swirlers.

The degree or intensity of the swirl is calculated based on the non-dimensional swirl number 'S'. Swirl number is defined as the ratio of the axial flux of angular momentum (G_θ) to an axial flux of axial momentum G_x times the nozzle radius R_b.

$$S = \frac{G_\theta}{R_b G_x} \tag{3.1}$$

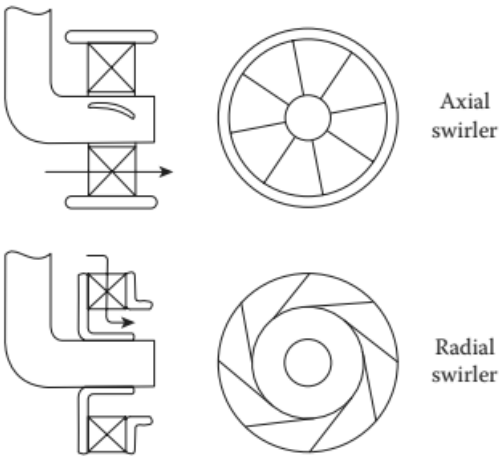

Figure 3.1: Types of swirler adopted from Ref.[70]

where G_θ and G_x are derived from the momentum equations for turbulent incompressible axisymmetric flow neglecting the viscosity since μ is negligible when compared to turbulent viscosity. For complete derivation, refer to Ref.[25]

$$G_\theta = \int_0^\infty (\rho uw + \rho\overline{u'w'})r^2 dr \tag{3.2}$$

$$G_x = \int_0^\infty (\rho u^2 + \rho\overline{u'^2} + (p - P_\infty))\, r dr \tag{3.3}$$

The measured axial and tangential momentum from equation 3.3 and 3.2 are highly uncertain; therefore, turbulent stress, pressure and swirl's rms terms in equation 3.3 and 3.2 are neglected since these terms contribute to a negligible momentum deficit. The equation 3.4 is the commonly used relation to quantifying the swirl intensity.

$$S = \frac{\int_0^R uw\, r^2 dr}{R\int_0^R u^2\, r dr} \tag{3.4}$$

Since the parameters mentioned above are not known priorly, the swirl number is defined geometrically based on the swirl angle of the vane [45] as seen in equation 3.5. This formulation aids in calculating the swirl intensity before the experimental or computational study.

$$S = \frac{2}{3}\left[\frac{1-(R_c/R_i)^3}{1-(R_c/R_i)^2}\right] tan\theta \tag{3.5}$$

Where, R_c is the radius of the central body of the annular pipe, R_i is the injector or nozzle radius of the swirler and θ is the swirl angle or vane angle. If the diameter of the centre body is very small when compared to nozzle diameter then equation 3.5 simplifies to:

$$S = \frac{2}{3}\, tan\theta \tag{3.6}$$

Depending on the swirl intensity and its flow field, the swirl is classified as weak, intermediate, and strong swirls. The swirl number range for each of the swirl types varies, and it is unique to a specific case since it depends on many factors like Reynolds's number and the enclosure ratio of the sudden expansion. The intensity of the swirl for a particular case is classified based on the formation of Recirculation Zones (RZ) and their interactions with other flow features. Such flow field formation and their interactions are discussed in the next sections.

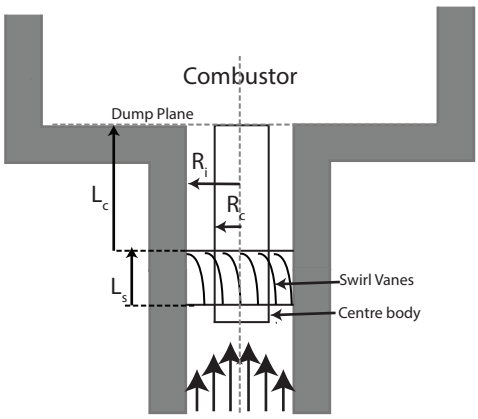

Figure 3.2: Geometry of a swirler adapted from Ref.[18]

3.1.1. Swirl flow characteristics

The physics of the swirling flow depends mainly upon whether the geometry is confined or unconfined. Swirling flow in the context of this study is denoted by a swirling flow from the nozzle followed by a sudden expansion into the surroundings or confinement as shown in figure 3.2. Imparting swirl in the flow field creates an Inner Recirculation Zone (IRZ) or Centre Recirculation Zone (CRZ) aerodynamically in the vicinity of the nozzle exit due to the presence of the bluff body. However, the formation of CRZ is also seen in non-swirling annular jets Vanierschot and Van den Bulck [123]. In swirling jets, the so-formed CRZ is significantly affected by swirl intensity and other flow features created due to swirl.

Vanierschot and Van den Bulck [123] studied the effects of swirl on the CRZ for different swirl numbers of the turbulent annular swirling jet. From the streamlines in figure figure 3.3 of both non-swirling and swirling flow, the formation of recirculation zones near the enclosure (Walls) is evident, which are termed as Outer Recirculation Zones (ORZ). The formation of ORZ is due to the presence of walls. The ORZ is subjected to axial and radial oscillations and periodic shrinkage. Shear layers are formed in between the boundaries of the two RZ. Shear layers are thin layers with a high tangential velocity gradient. The Inner shear Layer (ISL) is formed between IRZ and jet boundaries, and the Outer Shear Layer (OSL) is formed between the ORZ and jet. In these shear layers, eddies are generated due to shear layer instability of Kelvin Helmholtz type [50]. These eddies were visualized by the isocontours of λ_{ci}, where λ_{ci} is the imaginary part of the eigenvalue of the velocity gradient tensor. λ_{ci} was used rather than vorticity since it identifies only the free stream vortices.

From figure 3.3 (a), it is seen that a large number of eddies are generated in the ISL than in the OSL of the non-swirling jet. These eddies cause perturbations and continue to grow as they convect within the CRZ; hence a peak value of velocity fluctuations is seen in ISL. This will perturb the stagnation point of the CRZ. Hence the stagnation point of the CRZ is seen slightly off from the central axis.

The figure 3.3 (b) shows the flow field of the swirling jet with swirl intensity S = 0.37. It is seen that apart from the CRZ formed close to the nozzle, a second RZ has formed due to Vortex Breakdown (VB). The comprehensive reason for the formation of VB is lacking in the literature.

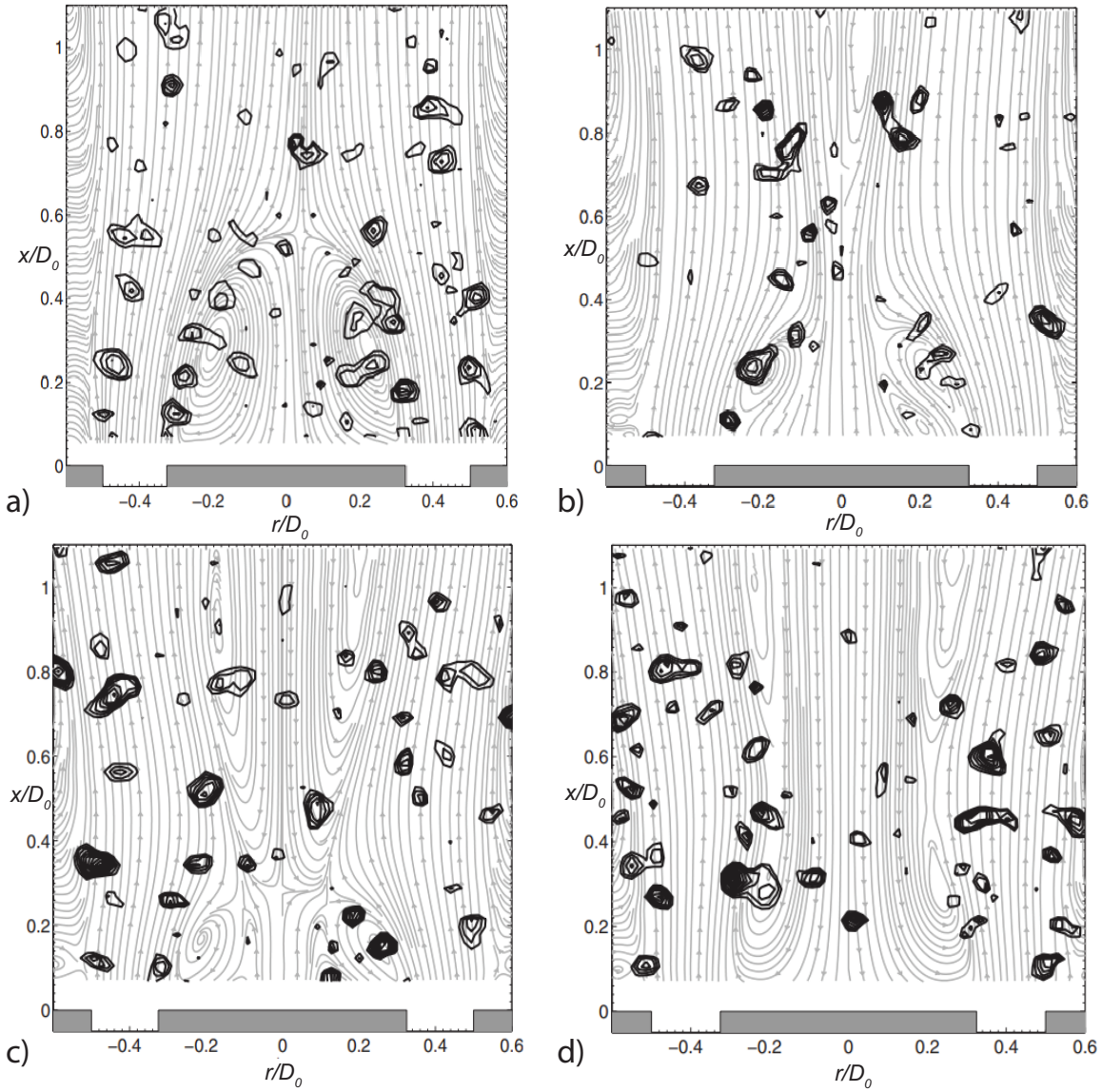

Figure 3.3: Isocontours of λ_{ci} with time-averaged streamlines of non- swirling jet (a), swirling jet S = 0.37 (b), S = 0.57 (c) and S = 0.74 (d) adopted from [123].

According to Escudier and Keller [37] and Lucca-Negro and O'doherty [76] VB is due to the adverse radial pressure gradient generated as a result of tangential velocity decay along the central axis. As a result of the swirling flow expanding radially in the sudden expanding geometry, an adverse radial pressure gradient is created in the centre. According to Gupta et al. [45], The formation of VB is due to swirl-induced radial pressure gradient. The physical mechanism of VB and their types are extensively reviewed by Lucca-Negro and O'doherty [76] and Brito Lopes et al. [13]. Centrifugal force is created as a result of the radial pressure gradient. Therefore, the centrifugal forces must be in equilibrium with the radial pressure gradient. VB is said to take place only if the swirl intensity is greater than a particular swirl intensity known as critical Swirl intensity (S_{cr}).

$$\frac{dp}{dr} \approx \rho \frac{W^2}{r} \tag{3.7}$$

Comparing the flow field of figure 3.3 (b) and (c), it is evident that the VB size and strength of the CRZ increase as the swirl number (S) increases. VB bubble found downstream of the nozzle moved upstream upon increasing swirl intensity. At high swirl (S = 0.74) figure 3.3 (d), the RZ formed in the vicinity of the nozzle merges with the breakdown bubble.

Apart from the formation of RZ and shear layers, Precessing Vortex Core (PVC) is found in swirling flow due to the axial and radial periodic oscillations of CRZ precessing around the axis of symmetry [120]. PVC is an asymmetric scale coherent 3-D structure. PVC is developed when the vortex core in the centre precesses around the axis of symmetry. Studies done by Huang and Yang [47] show that PVC stays on the boundary of the IRZ. According to Syred [120], these instabilities are the function of S, equivalence ratio and flow geometry (confinement ratio) for reacting flows. The vortex core processing around the axis is shown in figure 3.4. The instabilities mentioned above and their interaction make the swirling flow field complex.

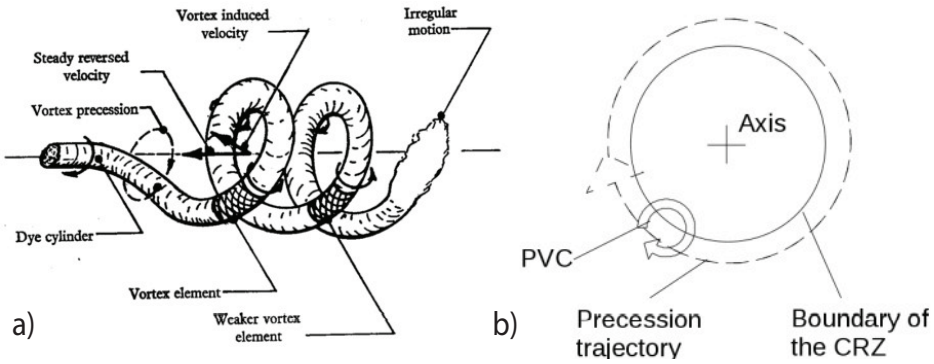

Figure 3.4: Sketch of Precessing Vortex Core (PVC) from Ref.[120] and [76]

3.2. Flame Stabilization

Flame is stabilized when there is a quasi-steady balance between the local flame speed and the flow velocity. Flame stabilization is achieved by employing various techniques: placing a bluff body, opposed jets, recessed bluff body and pilot flame in the flow field as shown in figure 3.5. The bluff body aids in anchoring the flame in their wake region when the flow speed is higher than the flame speed, whereas the opposed jet creates an area of low velocity for the flame to settle. The main drawback of the above two techniques is the pressure loss due to the drag. In the case of the recessed bluff body and pilot flame, the stabilized flame is often prone to blow off since the recirculation zone formed by the recessed bluff body and pilot flame are directly influenced by the velocity fluctuations in the mainstream flow [112].

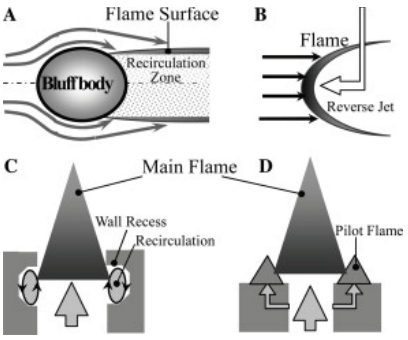

Figure 3.5: Flame stabilization techniques Ref.[112]

The swirl is widely utilized in many gas turbine combustors for flame stabilization, apart from the aforementioned techniques. The swirl stabilized combustor does not need an extra jet or bluff body near the flame to generate a region of low velocity or RZ to anchor the flame. Instead, the CRZ created as a result of VB helps in stabilizing the flame in the region of high-velocity shear layers as shown in figure 3.6. The CRZ aids in bringing back hot combusted product to the flame by which the flame is stabilized. Apart from the CRZ, ORZ created due to sudden expansion also plays a vital role in stabilizing the flame. PVC arising from swirling flow, as discussed in subsection 3.1.1 leads to enhanced mixing. While its unsteady behaviour may trigger resonance with the combustor acoustics modes and lead to thermo-acoustics instabilities. The turbulent intensity of such PVC is high, and consequently, the flame speed.

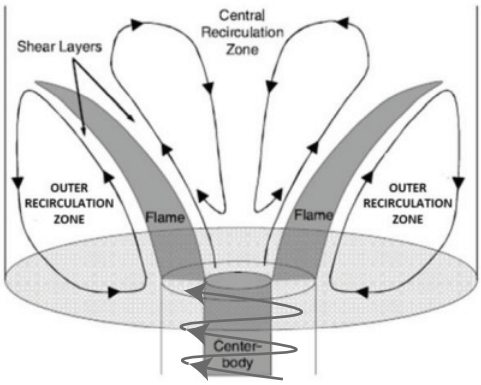

Figure 3.6: Flame of the reacting swirling flow in confinement from Ref.[117]

Swirl burners are used in both premixed and non-premixed combustion due to their flame stability and combustor performance. The generation of an RZ is desirable since it brings back the hot products to serve as a root by providing a heat source for continuous ignition of the fresh reactants for flame stabilization, especially in lean premixed combustion. Tecflam swirl burner [82], Sydney swirl burner [110], Turbomeca swirl nozzle [83] and dual swirl burner [31] are some of the laboratory scale swirl burners that are studied extensively in literature. Turbomeca and dual swirl burner use radial swirler, whereas Sydney swirl burner utilizes tangential port to create a swirl. The Tecflame swirl burner generates swirl mechanically by movable block. A detailed review of experimental works on the aforementioned swirl burners was performed by Al-Abdeli and Masri [3], for both confined and unconfined conditions.

3.3. Low Swirl Burners

The concept of stabilizing the flame using a large RZ in high swirl flows was a proven technique. The alternate mechanism of stabilizing the flame in low-swirl flow employing flow divergence was discovered by the research group led by Dr Robert K. Cheng in 1991 at Lawrence Berkeley National Laboratory (LBNL) [17]. A swirl was created in the flow field by introducing a small amount of air tangentially in the co-flow of the concentric burner, while an un-swirled flow of premixed reactants was supplied to the inner region. This method of generating swirl is known as jet Low Swirl Burner (LSB). Centrifugal force induced by the swirl made the flow diverge, and the flame was stabilized at the location where the local mass flux balances the burning rate. The swirl was varied by adjusting the tangential airflow. The weak swirl pushed the flame downstream until blow-off, while the strong swirl pulled the flame close to the nozzle exit. The most distinct characteristic of this method of flame stabilization is that flame stabilization does not rely on flow recirculation, and the so-produced flames were detached from the burner rim.

Yegian and Cheng [131] performed laser diagnostics to investigate the flame stabilization mechanism, flow field and flame stability of jet LSB when the burner was confined with a quartz glass cylinder of various diameters and end constrictions with a small central opening. It was found that LSI adapted well to the enclosure and doesn't exhibit flame oscillations. Whereas, in high swirling flow, several studies from Heitor et al. [46] and Schefer et al. [108] show that flame stabilization was sensitive to swirl intensity [113].

Yegian and Cheng [131] identified a small region of flow reversal in the non-reacting flow of enclosure ratio 3 (thrice the diameter of the nozzle). But, for reacting flow, the RZ was not identified, this is because of the combustion-induced flow acceleration. But for enclosure ratio two, a long RZ on the central axis and small recirculation zones are found near the walls for both non-reacting and reacting flow. Even though the RZ is formed on the central axis, it did not play any role in stabilizing the flame [131].

The swirl created through the jet LSB is not possible to implement in practical applications like gas turbine combustors because of multiple inlet ports. So, later in 2000, Cheng et al. [22] invented a patented novel swirler design known as vane LSB consisting of vanes known as a Low Swirl Injector (LSI). LSI was placed in the premixer at a distance of one or two diameters upstream of the dump plane to ensure residence time for mixing to take place in non-swirling and swirling regions. The LSI consist of two sections, the annular swirling region and the inner non-swirling region figure 3.7 shows the upstream and downstream images of the LSI. The swirling part consists of packed swirl vanes, and a perforated plate is present in the inner region to impart turbulence to the flow.

Figure 3.7: Images of LSI, upstream image (a) and downstream image (b) adopted from [27]

3.3.1. Swirl number definition of LSI

The difference in the flame shape of the jet LSB and vanes LSB was reported by R. K. Cheng et al., [22]. It was found that the jet LSB flames were planar, whereas the flames produced by vanes LSB were bowl-shaped. It was also reported that the swirling flow in the annular region did not disturb the core flow. The non-dimensional number defined in equation 3.4 was used to quantify the swirl of Jet LSB, but equation 3.4 does not apply to vane LSB since many uncertainties were encountered while integrating high gradient velocity near the wall, so Cheng et al. [22] came up with the new equation 3.8 to quantify swirl based on the mass flow split between the un-swirled and swirled region.

$$S_v = \frac{2}{3}\tan\theta \frac{1-(R_c/R_i)^3}{1+(R_c/R_i)^2\left((U_c/U_a)^2-1\right)} \tag{3.8}$$

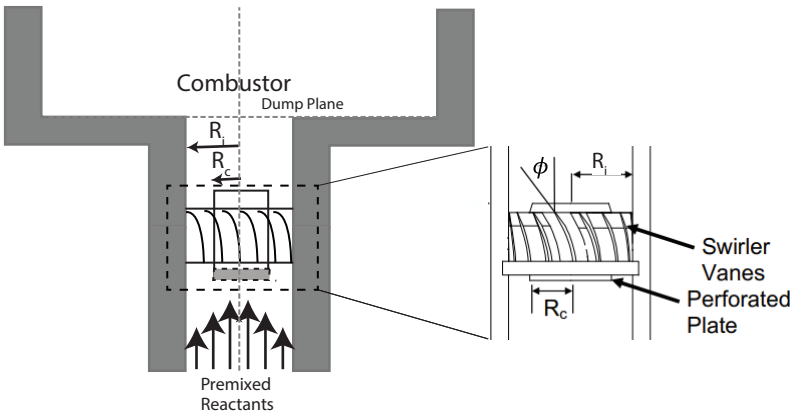

Figure 3.8: Schematics of the Low Swirl Injector (LSI), adapted from Ref. [22] and [38]

Here θ is the vane angle, R_i is the radius of the injector, R_c is the radius of the non-swirled central region, U_c and U_a is the area averaged or volume-averaged velocity of the non-swirled central region and swirled annular region respectively. When U_c is zero the equation 3.8 simplifies to equation 3.5 used in High Swirl Injectors (HSI). It is challenging to quantify the swirl before the experiments since one needs to know the average velocity in the centre and annular channel, so Cheng et al. [24] replaced U_c/U_a in terms of mass flow rate as defined in equation 3.9.

$$S = \frac{2}{3}\tan\theta \frac{1-R^3}{1-R^2+m^2\left(1/R^2-1\right)^2 R^2} \tag{3.9}$$

Where, R = R_c/R_i and m = m_c/m_a, m_c and m_a is the mass flowing through the centre channel and the annular swirling region respectively. Therkelsen et al. [121] did a parametric study to understand the effects of different R, vanes shape, vane angles, and perforated plate blockage based on LSI Lean Blow Out (LBO) performance. The mass flow split was calculated based on the drag coefficients of the swirler. The drag coefficients were sensitive and directly proportional to R, but it was insensitive to θ. The thin vane with a constant radius of curvature similar to the one used by Johnson et al. [53] produced a high-pressure drop than a curved vane. The m can be varied by changing the perforated plate thickness, where an increase in thickness reduces m_c [7].

3.3.2. Comparison of HSI and LSI flow fields

From the articles published by the research group of R. K Cheng [17] [131] [22] [24] it is evident that flame stabilisation mechanism in LSB is different from high swirl flame stabilisation mechanism. The former made use of a swirl to stabilize the flame, whereas the latter uses an RZ to stabilize the flame. Johnson et al. [54] studied the flow fields of HSI (figure 3.2) and LSI (figure 3.8) of premixed methane flame at Standard Temperature and Pressure (STP) by using Particle Image Velocimetry (PIV). The LSI and HSI were mounted vertically on the top of the flow settling chamber and fired without an enclosure as shown in flame photographs figure 3.10 (a) and (b) of HSI and LSI, respectively. The figure 3.9 shows the PIV image of the flame produced from HSI and LSI. The difference in mie scattering intensities outlines the flame front.

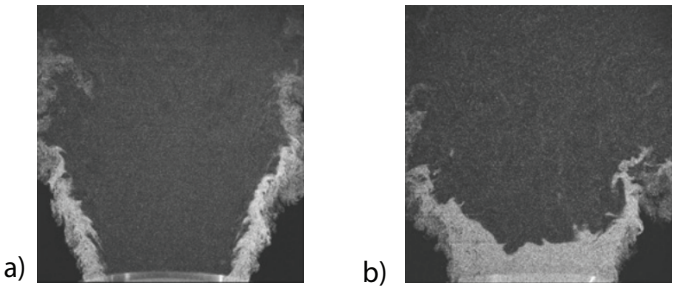

Figure 3.9: PIV images of flames produced by HSI and LSI respectively, adopted from [54]

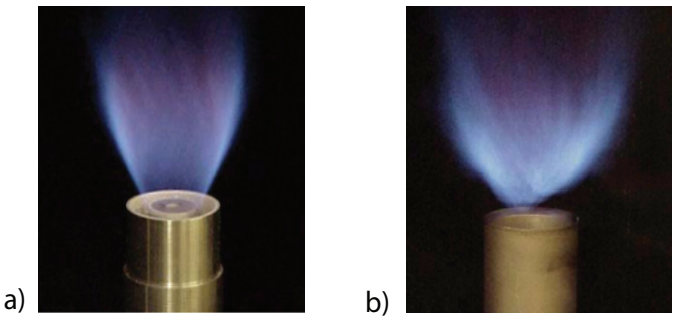

Figure 3.10: Photographs of flames produced by HSI and LSI respectively, adopted from [54]

From figure 3.10 and figure 3.9, it is evident that the HSI flame was attached to the burner rim, whereas the LSI flames were detached. The figure figure 3.11 (a) and (b) show the non-reacting mean velocity vector of HSI and LSI superimposed on the contour of 2D turbulent kinetic energy, respectively. It is seen that in figure 3.11 (a) a strong RZ is formed in the wake of the centre body, and in figure 3.11 (b) a small region of flow reversal was found along the central axis. Similarly, comparing the reactive flow field of HSI and LSI (figure 3.12 (a) and (b)), a weak RZ and decreased velocity decay were found in HSI and LSI, respectively, when compared to figure 3.11. This is due to combustion-induced accelerations and the combined effect of increased viscosity in hot products [51]. The contour of the turbulent kinetic energy of the non-reacting flow shows that turbulent intensities are high in the shear layers. On the other hand, the turbulent kinetic energy was found to be low for reacting flow. Johnson et al. [54] compared RZ formed in HSI and LSI and found that the recirculation mass flow ratio in LSI was forty times lower than that of HSI.

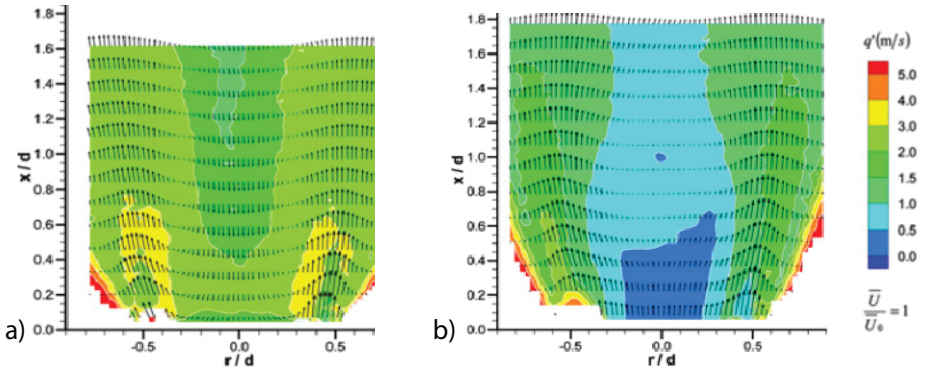

Figure 3.11: Mean velocity vectors of non-reacting flow-field on the contour of 2D turbulent kinetic energy of HSI (a) and LSI (b), adopted from [54]

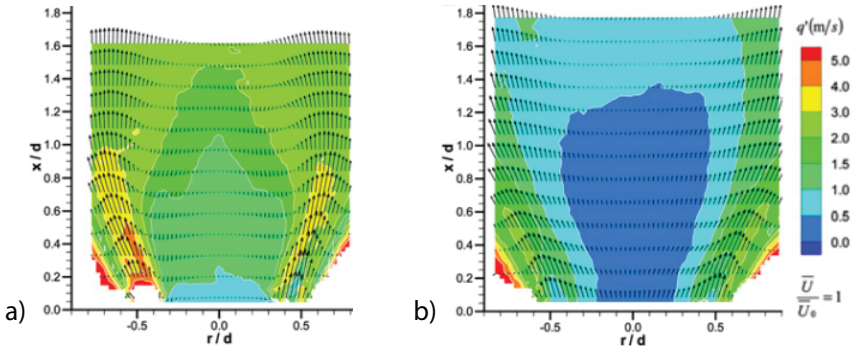

Figure 3.12: Mean velocity vectors of reacting flow-field at $\phi = 0.7$ on the contour of 2D turbulent kinetic energy of HSI (a) and LSI (b), adopted from [54]

3.3.3. Flow aerodynamics of LSB

LSB exploits the principle of propagating the wave nature of the premixed flame. They consume the reactants like self-sustained waves that propagate at flame speed. Hence this concept of flame stabilisation is feasible only for premixed flames [23]. The LSB utilises the diverging flow field produced due to the swirl. The presence of the non-swirling central passage inhibits RZ formation in the near field region of the nozzle exit (i.e. flow field downstream of the nozzle exit). Due to the diverging flow field, the fluid experiences an aerodynamics strain along with the velocity down ramp in the near field region due to the adverse axial pressure gradient. This allows the flame to settle in a location where the flame and flow velocity are equal and opposite. Cheng et al. [23] investigated the aerodynamics of the LSB flow field of various Re for a constant swirl intensity of 0.5 in an open environment. From the analysis of PIV data, Cheng et al. [23] concluded that the shear stresses were maximum in the shear layer and minimum in the non-swirling region for all the cases due to the turbulence created by the perforated plate. In accordance with Johnson et al. [54] and Yegian and Cheng [131], a small recirculating zone further downstream of the flame was formed for the highest Re.

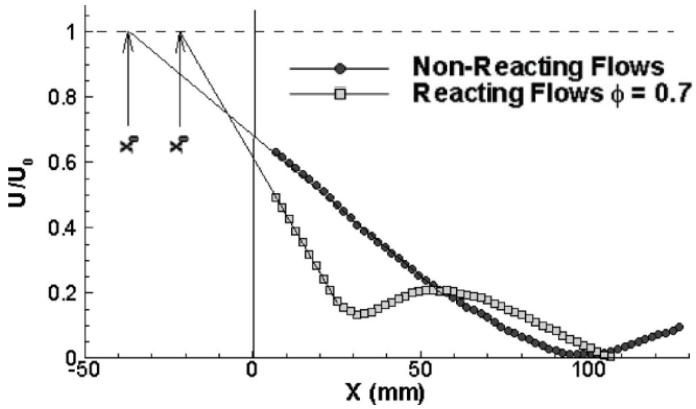

Figure 3.13: Averaged axial velocity profiles of non-reacting and reacting flows along the central axis normalised and extrapolated with free stream velocity U_0 for Re ≈ 77500, adapted from [23].

Cheng et al. [23] discussed the two important parameters, namely the virtual origin x_0 and axial stretch rate or divergence rate $a_x = (dU/dx)/U_0$ which are important in characterising the diverging flow field of LSI. The x_0 is a reference point in the centre axis, where the flow field starts to diverge. This is analogous to the upstream stagnation point of the RZ in high swirl flows. The x_0 is calculated by extrapolating the velocity data obtained after the dump plane to the free stream velocity U_0 as shown in figure 3.13. They compared x_0 for increasing Re of both non-reacting and reacting flows. From figure 3.14 (a), it is evident that the x_0 decreases with increasing Re, which signifies the upstream shift of the diverging flow, but eventually, x_0 was found to be insensitive to Re. For a constant Re, the x_0 was found to be high for non-reacting flow compared to reacting flow. Similarly, the velocity decay rate or strain rate a_x was also evaluated for increasing Re of both non-reacting and reacting flows, figure 3.14 (b). The strain rate remained constant irrespective of Re. An increase in velocity decay was seen in reacting flows, and it is also obvious from the slope of the reaction flow velocity profile in figure 3.13.

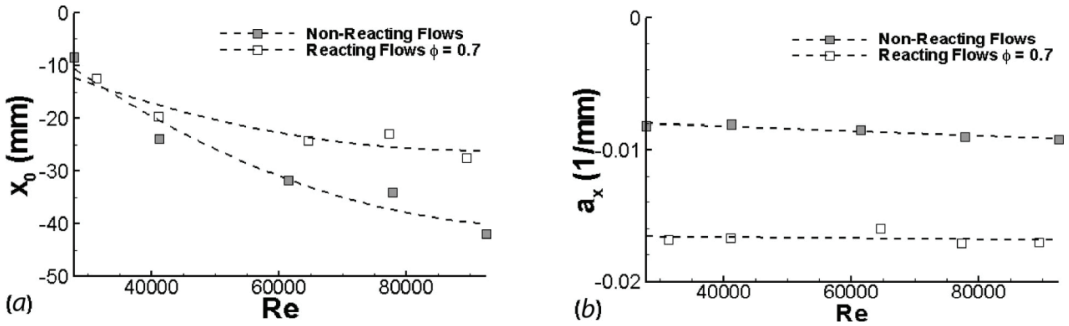

Figure 3.14: Virtual origin x_0 (a) and velocity decay rate a_x (b), for increasing Reynolds's number, adapted from Cheng et al. [23],

Cheng and Littlejohn [20] did an experimental study to understand the effects of enclosure in LSB's. They chose an enclosure ratio of 3.15 (20cm) and 2.44 (15.5cm) to analyse the flow fields of an open and enclosed environment of both reacting and non-reacting flow with S = 0.51. From the normalized mean axial velocity profiles of non-reacting flows along the central axis demonstrated in figure 3.15 (a), it is seen that the velocity profiles show more or less the same trend irrespective of Re, except for U_0 = 10 m/s since the flow was not developed until Re> 50000 in open flow. However, differences between open and enclosed flow fields were found. The x_0 increased when the enclosure ratio was decreased, and a Strong RZ was formed in enclosed flows.

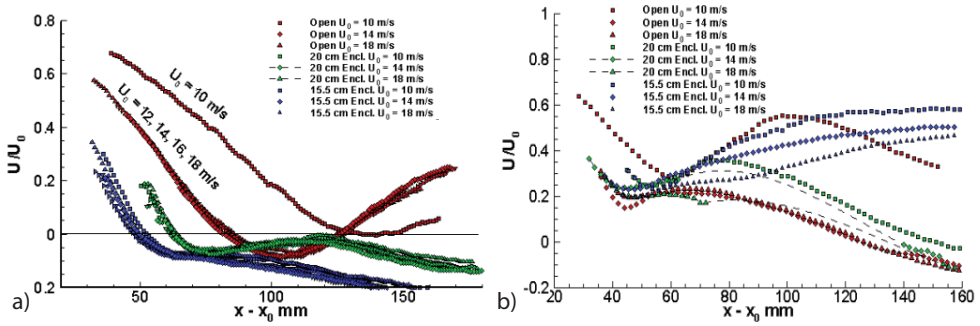

Figure 3.15: Normalized axial velocity of Non-reacting (a) and reacting (b) flow field along the centre line of the burner, adapted from Cheng and Littlejohn [20]

Similarly, the methane/air reacting flow velocity profile shown in figure 3.15 (b) also depicts the exact trend in the near field region ($x - x_0 < 40mm$) irrespective of Re, except for U_0 = 10 m/s in open environment. It is evident from figure 3.15 (b) that the RZ formed in non-reacting flow for enclosure ratio 2.44 was not found within the PIV domain in reacting flow. Since the PIV domain was only set to 13 cm by 13 cm, which is less than half the size of the enclosure length, the formation of RZ in an enclosure ratio of 2.44 can not be qualified. Hence, the diverging flow field structure was not sensitive to Re in both reacting and non-reacting flow.

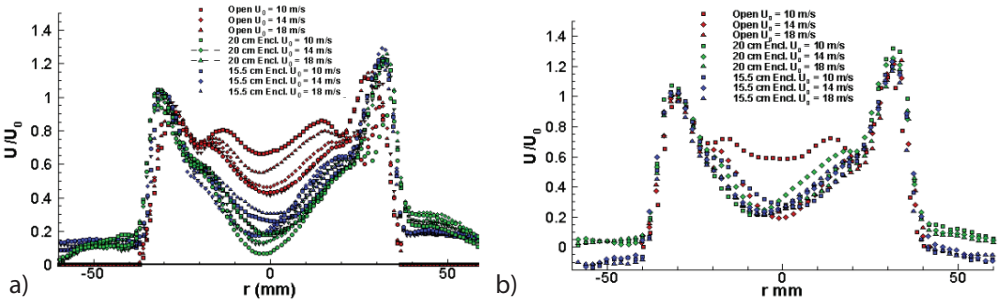

Figure 3.16: Normalized Axial velocity of Non-reacting (a) and reacting (b) flow field along the radial line at 6.5 mm downstream of the dump plane, adapted from Cheng and Littlejohn [20]

Analogously, from the radial velocity profiles shown in figure 3.16 (a), the peak value and their location followed the same trend. But in the centre, non-swirled region, significant differences were identified in figure 3.16 (a) because of the undeveloped flow features present in the open flow environment. Two peak values seen in the radial profiles of the TKE (figure 3.17) show the presence of inner and outer shear layers in reacting and non-reacting flow fields. The same self similar flow features was also reported by Littlejohn and Cheng [74], Cheng and Littlejohn [21] and Cheng et al. [18] from their PIV analysis of reacting and non reacting flows fields.

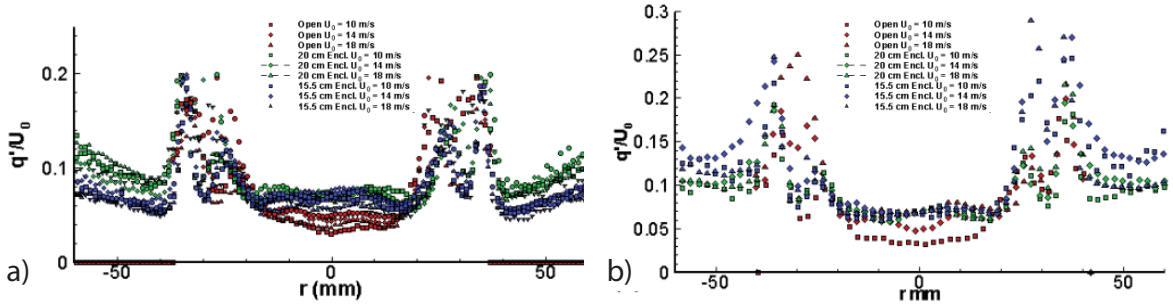

Figure 3.17: Normalized 2D turbulent kinetic energy of Non-reacting (a) and reacting (b) flow field along the radial line at 6.5 mm downstream of the dump plane, adapted from Cheng and Littlejohn [20]

Cheng et al. [23] investigated the adaptation of LSB to different fuels. He derived an equation 3.10 for a stable flame at a fixed location based on the theory that the turbulent flow speed (S_T) must be equal to the flow velocity at the leading edge of the flame.

$$1 = \frac{S_T}{U_0} + \frac{dU}{dx}\frac{(x_f - x_0)}{U_0} \tag{3.10}$$

Where x_f is the position of the flame. From equation 3.10, it is evident that for fuel with high S_T (e.g.H_2), the divergence of the flow must be reduced and vice versa for fuels having less S_T (e.g. biomass) to maintain stability.

3.3.4. Flame aerodynamics of LSB

Cheng and Littlejohn [20] investigated the flame behaviour of open and enclosed flames of hydrogen-enriched fuels. In hydrogen-enriched fuels, above a certain ϕ, an 'M' shaped flame attached to the burner rim was produced rather than the detached 'v' shaped flame seen in hydrocarbon fuels. The formation of an 'M' shaped flame was attributed to the ignition happening in the outer shear layer due to the highly diffusive nature of hydrogen.

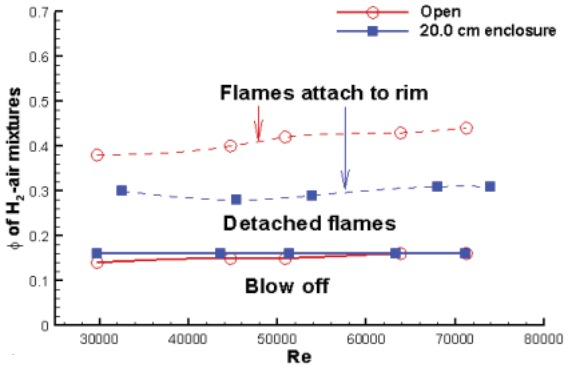

Figure 3.18: Flame shape map of hydrogen-enriched flames, adapted from Ref.[19]

From the figure 3.18, it is evident that the enclosure did not affect the LBO limit. For enclosed flames, the ϕ limit of the attached flame remained constant irrespective of different bulk velocities. The ϕ limit of the open flame was higher than the enclosed flame, which is attributed to the ORZ formation in the enclosure. The ϕ limit was inversely proportional to the percentage of hydrogen in the fuel. Cheng and Littlejohn [20] concluded that both the attached and detached flame did not alter the flame stabilisation mechanism, but the formation of ORZ in the enclosure provided additional stabilisation resulting in an 'M' shaped flame. In addition, no significant difference was found between the flow fields of the detached and attached flames. Hydrogen-enriched fuel-produced flames showed similar flow field features to hydrocarbon flames, discussed in subsection 3.3.3.

Cheng et al. [19] investigated the performance of LSI for different H_2 concentrations at STP and at elevated temperature and pressure conditions similar to the gas turbine in SimVal combustor of NETL. The change in flame shapes phenomenon seen by Cheng and Littlejohn [20] also occurred at STP and at elevated temperature and pressure conditions.

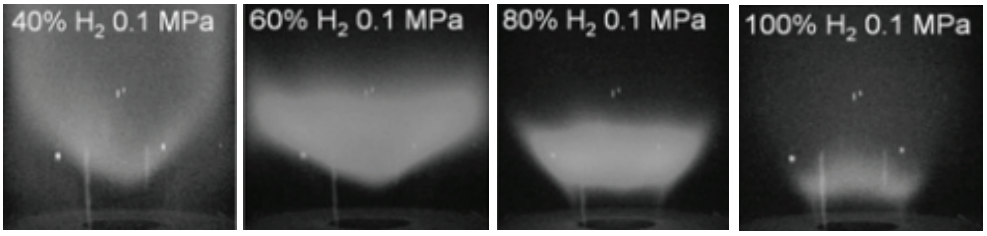

Figure 3.19: Photographs of flame luminosity of various CH_4/H_2 flames at $\phi = 0.4$, P= 0.1 MPa, adapted from Ref.[19]

The flame shape and flame stabilization of H_2 enriched flames were similar to CH_4 flames containing up to 60 vol.% of H_2 concentration as observed by Littlejohn and Cheng [74] and Cheng et al. [23]. The flame started to move closer to the burner exit as the H_2 concentration was increased above 60 vol.% of due to the highly diffusive nature of H_2. At 80 vol.% of H_2 the flame was attached to the burner exit, as seen in flame photographs (figure 3.19). Irregular burning of H_2 in the ORZ was also reported for H_2 enriched flames.

3.4. Turbulent Premixed Combustion modelling

In combustion, the turbulence of the flow is influenced by the flame due to flame-produced flow acceleration, which is due to heat release from the flame front. Conversely, turbulence can also enhance the chemical reaction rate or even quench the flame [99]. Therefore, to model the two-way interaction between flame and flow, an additional species transport equation 2.36 for each species involved in combustion is needed. The source term ($\overline{\dot{\omega}_k}$) in equation 2.36 is highly nonlinear due to the exponential function present in the rate coefficient. Therefore, modelling $\overline{\dot{\omega}_k}$ is of importance since it is responsible for the heat and species production in the flame zone. Since most of the real-life problems of interest are turbulent, the Favre averaged species transport equation, which is succinctly expressed below, is used to model combustion.

$$\frac{\partial}{\partial t}\left(\bar{\rho}\tilde{Y}_k\right) + \frac{\partial}{\partial x_i}\left(\bar{\rho}\tilde{u}_i\tilde{Y}_k\right) = -\frac{\partial}{\partial x_i}\left(\widetilde{J^k}\right) + \overline{\dot{\omega}_k} - \frac{\partial}{\partial x_i}\left(\bar{\rho}\overline{u_i''Y_k''}\right) \tag{3.11}$$

The second term on the left side is the convective term, and the first term on the right side of equation 3.11 depicts the laminar diffusive flux, which can be modelled using Fick's law as stated previously in equation 2.37. Still, most often, it is negligible when compared to turbulent flux. Therefore, the laminar diffusive flux is neglected. The middle term in the right side of equation 3.11 represents the mean chemical source term. Premixed combustion is modelled so that the interactions between turbulence and chemistry can be addressed.

The last term in equation 3.11 is the turbulent Scalar flux $\left(\bar{\rho}\overline{u_j''Y_k''}\right)$. In RANS, it is modelled based on the gradient diffusion assumption as defined in equation 3.12. Sc_t is the turbulent Schmidt number, and it is 0.7 by default in Fluent for eddy viscosity turbulence models, and it is equal to unity in Reynolds Stress turbulence model [44]. The presence of counter diffusion was noticed by Bray et al. [12] and Pope [100]. But for highly turbulent flows ($Re_T >> 1$) counter diffusion is assumed to be negligible [125].

$$\left(\bar{\rho}\overline{u_i''Y_k''}\right) = -\left(\frac{\mu_t}{Sc_t}\right)\frac{\partial Y_k}{\partial x_i} \tag{3.12}$$

The mean chemical source term is the only unclosed term in equation 3.11. Due to the presence of non-linearity and multiple reactions, direct analysis is not feasible. So, modelling the source term appropriately predicts the flame and its effects on the flow. In the case of hydrogen combustion, reactions take place rapidly, implying the chemical time scale is smaller than the turbulent time scale (Da>1). In such a case, combustion occurs in a flamelet regime. As discussed previously in section 2.7, turbulent eddies can't penetrate into the flame in the flamelet regime and flame is assumed to be devoid of flow interactions. Therefore, the flame is assumed to be thin and occupies only a small region of the whole domain. Combustion models, which aim to resolve the chemical source term based on the geometry of the flame and rate limiting turbulent mixing, are discussed in the upcoming section.

3.4.1. Progress variable equation

Linking all the system variables to one specific variable, 'c' is known as the progress variable approach, with the assumption of thin flame, one-step chemistry with unit Lewis number and adiabatic condition. Where c is known as the normalized sum of product mass fraction across the flame as defined in equation 3.13. By definition, c ranges from 1 to 0, where c= 0 represents the unburned state, and c= 1 represents the burned state. The main advantage of this approach is that, instead of tabulating system variables as a function of spatial distance, solving the scalar transport equation of a single normalized progress variable saves computing time. Then for the specific expansion ratio, the mean density decreasing across the flame is calculated based relation defined equation 3.14.

$$c = \frac{Y_F - Y_{F,min}}{Y_{F,max} - Y_{F,min}} \tag{3.13}$$

$$\bar{\rho} = \frac{\rho_u}{(1 + \Omega\tilde{c})} \tag{3.14}$$

The Favre averaged transport equation of progress variable transport equation:

$$\frac{\partial}{\partial t}(\bar{\rho}\tilde{c}) + \frac{\partial}{\partial x_i}(\bar{\rho}\tilde{c}\tilde{u}_i) = -\frac{\partial}{\partial x_i}\left(\bar{J}_c\right) + \overline{\dot{\omega}_k} - \frac{\partial}{\partial x_i}\left(\overline{\rho u_i'' c''}\right) \tag{3.15}$$

where the first term on the right side of equation 3.15 represents the laminar diffusion, and the last term represents the turbulent scalar flux. Modelling these two terms are similar to the ones discussed in section 3.4. The mean reaction rate is the second term on the right-hand side of equation 3.15. The $\overline{\dot{\omega}_k}$ is modelled based on the assumption that it is a product of laminar reaction rate and flame wrinkling due to turbulence as depicted in equation 3.16.

$$\overline{\dot{\omega}_k} = \rho_u S_{L0} I_0 \Sigma \tag{3.16}$$

I_0 is the flame stretch factor, and Σ is the average flame surface density. The reaction source term is modelled based on algebraic correlations, which are discussed elaborately in the next sections under the flamelet assumption.

The progress variable transport equation may not model hydrogen flames accurately due to the non-unit Lewis number effects (preferential effects). Since transport equations of species and temperature are essential to model hydrogen flames, provided the coupling effects of mass and heat diffusion are resolved.

3.4.2. Eddy Dissipation Model (EDM)

The Eddy Dissipation Model (EDM) is developed from the Eddy Breakup Model (EBU), which was initially developed by Spalding [114] for computing turbulent premixed flame. This was further developed into the eddy dissipation model by Magnussen and Hjertager [79]. The EDM calculates the mean reaction rates ($\overline{\dot{\omega}_k}$), which is the unclosed term in the Favre averaged species transport equation 3.11. $\overline{\dot{\omega}_k}$ is expressed based on turbulent mixing as defined by equation 3.17 and 3.18 where, equation 3.18 is the limiting mass fraction species in premixed hydrogen-oxygen mixture. Where A and B are model constants with values 4 and 0.5, respectively. This model assumes that the chemical reaction happens much faster than turbulent mixing. This kind of model is suitable for flames where turbulent mixing is the rate-limiting step (Da>1), i.e. in the flamelet region [127].

$$\overline{\dot{\omega}_k} = \bar{\rho} A \left(\frac{\epsilon}{k}\right) \widetilde{Y}_{lim} \tag{3.17}$$

$$\widetilde{Y}_{lim} = \min\left(\widetilde{Y}_{H_2}, \frac{\tilde{Y}_{0_2}}{\beta}, B\frac{\tilde{Y}_{H_2 o}}{1+\beta}\right) \tag{3.18}$$

3.4.3. Eddy Dissipation Concept (EDC)

The EDC is an extension from EDM, developed by Magnussen et al [36]. It is based on the hypothesis that chemical reactions occur in fine structures where TKE dissipation occurs. The order of magnitude of the structure is assumed to be in the order of the Kolmogorov scales. The size of the structure (γ^*) is defined in equation 3.19.

$$\gamma^* = \gamma_\lambda^3 \tag{3.19}$$

where γ is the ratio of mass in the fine structure to the total mass, as shown below;

$$\gamma_\lambda^3 = \left(\frac{3C_{D2}}{4C_{D1}^2}\right)^{1/4} \left(\frac{\nu\varepsilon}{k^2}\right)^{1/4} = C_\gamma \left(\frac{\nu\varepsilon}{k^2}\right)^{1/4} \tag{3.20}$$

where $C_{D1} = 0.134$, $C_\gamma = 2.137$, $C_{D2} = 0.5$ are model constants. The time scale of fine structure is expressed as $\tau^* = 1/\dot{m}^*$, where $\dot{m}^*$ is the ratio of mass exchange between the fine structure and the surrounding. The expressions for τ^* and $\dot{m}^*$ is defined as

$$\tau^* = \left(\frac{C_{D2}}{3}\right)^{1/2} \left(\frac{\nu}{\varepsilon}\right)^{1/2} = C_\tau \left(\frac{\nu}{\varepsilon}\right)^{1/2} \tag{3.21}$$

where $C_\tau = 0.408$ is a model constant as well. The mean reaction rate of fine structure is calculated from the equation 3.22

$$\overline{\omega_i} = \frac{\rho\left(\gamma_\lambda\right)^2}{\tau^*\left[1-\left(\gamma\gamma_\lambda\right)^3\right]}\left(\widetilde{Y_k} - Y_k\right) \tag{3.22}$$

The $\widetilde{Y_k}$ represents the mean mass fractions of fine structure, and Y_k is the mass fraction of the same species in a control volume. The major drawback of this model is the computational cost since it calculates the mean reaction rate of all reactions in chemical mechanisms.

3.4.4. Turbulent Flame speed Closure (TFC)

Closing the source term through flame speed correlations is known as Turbulent Flame Speed Closure (TFC). This is possibly by deriving the transport equation explicitly containing the flame speed. The Favre averaged transport equation containing flame speed is expressed in subsection 3.4.6.

$$\frac{\partial}{\partial t}(\bar{\rho}\tilde{c}) + \frac{\partial}{\partial x_i}(\bar{\rho}\tilde{c}\tilde{u}_i) = \overline{\rho s_d \mid \vec{\nabla} c \mid} - \frac{\partial}{\partial x_i}\left(\overline{\rho u_i'' c''}\right) \tag{3.23}$$

where S_d is the burning velocity. Comparing equation 3.15 and 3.23 it is evident that the source term in equation 3.15 is replaced by $\rho S_d|\vec{\nabla}c|$ in equation 3.23. To address the closure problem, s_d has to be modelled separately. The mean of gradient c is replaced by the gradient of mean c, and S_d is replaced by turbulent flame speed (S_T) as expressed in equation 3.24 [99]

$$\overline{\rho s_d|\vec{\nabla}c|} = \overline{\rho_u} S_t|\vec{\nabla}\tilde{c}| \tag{3.24}$$

where ρ_u is the density of the unburned mixture. Replacing the first term on the right-hand side in equation 3.23 by equation 3.24 and modelling the turbulent scalar flux, the equation 3.25 is obtained.

$$\frac{\partial}{\partial t}(\bar{\rho}\tilde{c}) + \frac{\partial}{\partial x_i}(\bar{\rho}\widetilde{u_i}\tilde{c}) = \frac{\partial}{\partial x_i}\left(\frac{\mu_t}{Sc_t}\frac{\partial\tilde{c}}{\partial x_i}\right) + \overline{\rho_u} S_t|\vec{\nabla}\tilde{c}| \tag{3.25}$$

Considering a steady flame in a coordinate system moving with the speed of the flame S_T, the convective term and the source term balance out each other and only the diffusive term present in equation 3.25 is responsible for controlling the flame thickness. Similarly, upon integrating the one-dimensional flame, the burning rate is equal to $\rho_u S_T$; therefore, the burning rate and the flame thickness are modelled separately. The transport equation equation 3.25 is based on the assumption that large eddies affect the flame brush thickness, whereas the small eddies affect the burning rate [73].

It is substantial to emphasize that the S_T and burning rate represent the same terminology but has different definitions. S_T or commonly known as local displacement speed ($S_{T,LD}$) is the speed of the reference plane with respect to the unburnt mixture. Burning velocity or commonly known as local consumption speed ($S_{T,LC}$) is a measure of the mass burning rate per unit surface area normalized by the ρ_u. There are a plethora of experimental measurements of S_T available in the literature that are scattered widely since it depends upon the choice of the reference plane, ϕ, Lewis number, flow field, flow geometry and also depends on how S_t is measured [30][122].

However, equation 3.25 still has the closure problem since S_T is unknown. S_T is modelled using the algebraic correlations available for different fuel mixtures. Zimont [134] developed an correlation 3.26 to model the unclosed turbulent flame speed when $Re_t > 1, Da >> 1, Ka > 1$.

$$S_t = A\alpha_w u'^{3/4} S_{L0}^{1/2} l_t^{1/4} \alpha^{-1/4} = Au' \left(\frac{t_f}{t_c}\right)^{(1/4)} \tag{3.26}$$

Where α is the unburnt thermal diffusivity, and α_w is a constant multiplier used to avoid the numerical flame acceleration close to the walls. If nonphysical flame acceleration is seen close to the walls, α_w less than unity is specified to avoid such circumstances. In experiments, radial quenching of the flame is seen close to the walls. From equation 3.26 it is evident that the u' is the dominating term and the correlation 3.26 is of the S_T form (equation 2.67) postulated by Damköhler. In addition to the parameters in equation 3.26, the flame stretch effect is possible to include within the equation 3.26.

$$G = \frac{1}{2}\,\mathrm{erfc}\left\{-\sqrt{\frac{1}{2\sigma}}\left[\ln\left(\frac{\varepsilon_{cr}}{\varepsilon}\right) + \frac{\sigma}{2}\right]\right\} \tag{3.27}$$

Where $erfc$, σ and ϵ_{cr} in equation 3.27 are the complementary error function, standard deviation of dissipation rate of TKE and dissipation rate of TKE at critical rate of strain (g_{cr}) respectively. σ and ϵ_{cr} are defined as:

$$\sigma = \mu_{str} \ln\left(\frac{l_t}{\eta}\right) \tag{3.28}$$

$$\varepsilon_{cr} = 15 v g_{cr}^2 \tag{3.29}$$

In Fluent by default g_{cr} is set to 1 x 10^8 which signifies no stretch. g_{cr} is generally determined from experiments. However, Fluent provides a model to calculate g_{cr} based on turbulence parameters.

$$g_{cr} = \frac{B S_{L0}^2}{\alpha} \tag{3.30}$$

Where B is constant with a value of 0.5. Various turbulent flame speed correlations specific to the LSB are discussed in the next section.

3.4.5. Turbulent flame speed correlation for hydrogen-enriched fuels

Apart from the Zimont turbulent flame speed model, many correlations similar to Zimont are available in the literature, among them the S_T correlations (equation 3.31) developed by Muppala et al. [89] were validated for premixed methane, ethylene and propane fuel produced flames for pressure up to 1.0 Mpa. The main difference between equation 3.26 and 3.31 is the inclusion of the pressure dependence term.

$$\frac{A_\mathrm{T}}{\bar{A}} = 1 + aRe_{l_t}^{0.25}\left(\frac{u'}{s_\mathrm{L}}\right)^{0.3}\left(\frac{p}{p_0}\right)^{0.2} \tag{3.31}$$

A equals 0.46 for methane/air premixed mixture, and P_0 is the atmospheric pressure. The S_T model equation 3.31 is commonly known by the name Algebraic Flame Surface Wrinkling (AFSW). Even though the turbulence is high, preferential diffusion effects play a major role in hydrogen-enriched flames. Therefore, Dinkelacker et al. [29] modified equation 3.31 by including the effective Lewis number Le_{eff} to account for non-unit Lewis number effects. Modified correlation of S_T is given as follows:

$$\frac{A_\mathrm{T}}{\bar{A}} = 1 + \frac{0.46}{exp(Le_{eff}-1)}Re_{l_t}^{0.25}\left(\frac{u'}{s_\mathrm{L}}\right)^{0.3}\left(\frac{p}{p_0}\right)^{0.2} \tag{3.32}$$

$$\frac{1}{Le_{eff}} = \frac{D}{\alpha} = \frac{x_{CH_4}D_{CH_4}}{\alpha} + \frac{x_{H_2}D_{H_2}}{\alpha} \tag{3.33}$$

Muppala et al. [87] applied equation 3.32 to simulate LSB produced flames. Muppala et al. [87] concluded that equation 3.32 performed well in predicting the axial velocity profiles of Cheng et al. [19].

3.4.6. Turbulent flame speed correlations specific to LSI

Littlejohn and Cheng [74] measured the S_T for ethylene, propane, methane and hydrogen flames of LSI and LSB. The S_T was measured at a point where the linear decay of the velocity profiles starts to deviate. The measured S_T/S_L data scaled linearly with u'/S_L, complying with the Damköhler second postulate. The similar kind of linear behaviour was also seen in other experimentally measured S_T data [22][20][74]. A correlation of S_T is obtained by fitting the experimental S_T data and takes the form of equation 2.69, where A is equal to unity and B is equal to 2.16 for hydrocarbon fuel produced flames in LSB [74].

$$\frac{S_T}{S_L} = 1 + 2.16\frac{u'}{S_L} \tag{3.34}$$

Substituting equation 3.34 in equation 3.10, the empirical constant B for different fuels can be presumed based on

$$1 - \frac{(x_f - x_0)}{U_0} = \frac{S_T}{U_0} = \frac{S_L}{U_0} + \frac{Bu'}{U_0} \tag{3.35}$$

From the above equation, the empirical constant 'B' aids in tailoring the flow field for stable combustion and investigating the operability of various fuel blends. Cheng and Littlejohn [20] observed the linear behaviour of S_T in enclosed flame hydrocarbon and hydrogen fuel-produced flames. The enclosure effects also showed that S_T was not affected. This kind of linear behaviour is unlike Bunsen burner-produced flames and expanding flames seen in combustors. For hydrogen flame, the empirical constant 'B' (3.15) was found to be higher than that of hydrocarbon flames, which is due to the slight upstream position $(x_f - x_0)$ of the flame when compared to hydrocarbon flame.

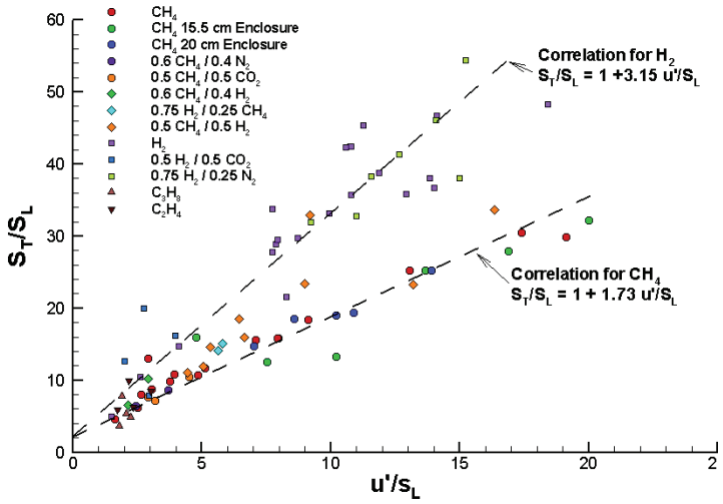

Figure 3.20: Flame speed correlation of LSI adopted from Ref.[20]

3.5. Flashback Mechanisms

Flashback is the inherent feature of premixed combustion. A generalised definition of flame flashback responsible for undesirable combustion can be defined as an upstream propagation of flame towards the burner or into the premix section of the gas turbine. Flame flashback significantly increases the temperature in the premix section and causes significant damaging effects since the pre-mixer is not designed to operate in such conditions [56]. Flashback is due to the imbalance between the local flame speed and flow velocity. When the former is greater than the latter flashback occurs. The mechanisms behind flashback are listed below [9]:

- **Flame propagation in core flow**: When turbulent flame speed (S_T) is greater than the inflow velocity, S_T is directly proportional to flame temperature. S_T increases when the reactivity of the fuel increases. Usually, this is avoided by maintaining a high inflow velocity in the gas turbines [9] [34]
- **Flashback due to combustion instabilities**: In swirling flows, phenomena like flow divergence, RZ and Vortex Breakdown (VB) distort the flame and cause unsteady heat release. Unsteady heat release couples non-linearly with pressure fluctuations and acoustic modes oscillations [9] which results in combustion instabilities. These instabilities result in velocity deficit which paves the way for the flame front to propagate upstream.

- **Flame propagation within boundary layer**: This mechanism occurs due to similar reasons mentioned in the flame propagation in the core. The propensity of flame to flashback in the boundary layer is much higher than core flow since the flow velocity gradually reduces towards the wall due to the no-slip condition, known as Boundary Layer Flashback (BLF). S_T outbalances the flame velocity in the boundary layer at a particular distance from the wall due to quenching [35]. Hence, swirling flows with very high Re, in addition to high swirling intensities, resulting in a thin boundary layer; thus, the flashback mechanism through boundary layer flashback is rarely feasible [34].
- **Combustion Induced Vortex Breakdown (CIVB)**: This mechanism is of particular interest in swirl stabilised combustion. In swirling flows, the flame will be anchored at the upstream tip of the recirculation zone in high swirling flows. Due to the non-aligned pressure and density contour lines, vorticity is created due to the baroclinic term in equation 2.7. This results in negative azimuthal vorticity, which decreases the axial velocity in the axis according to Biot Savart's law [40]. The combustion-induced negative velocity is accountable for the flame's flashback; this is called CIVB. From the point of initialisation of the flashback, the upstream propagating flame induces a force on its own, leading to further upstream propagation even when the flow velocity is greater than the turbulent flame speed. The additional force is generated as a result of turbulence (vortex) and chemistry (heat release) interaction at the RZ tip [62].

3.5.1. Flame flashback due to CIVB

Fritz et al. [41] experimentally investigated the mechanism of flashback in lean premixed natural gas combustion of swirling flows without a centre body. The visualized flame over 900 ms had various shifts in its position. Due to the complicated dynamics, the operability limit of the combustor was difficult to ascertain. Later Kröner et al. [65] obtained the flashback limits. The operability limit was determined for the flame when the flame propagated entirely in the mixing zone.

From the axial velocity measurement of the point just upstream of the flame in the axis of symmetry as shown in figure 3.21, the axial breakdown of the flow was seen with significant flow reversal, which in turn leads to the upstream flame propagation. Whereas, in the off-axis point, the magnitude of the flow reversal was much lesser than at the point on the axis. From figure 3.21, it is evident that the axial velocity drops to negative in a very short span of time.

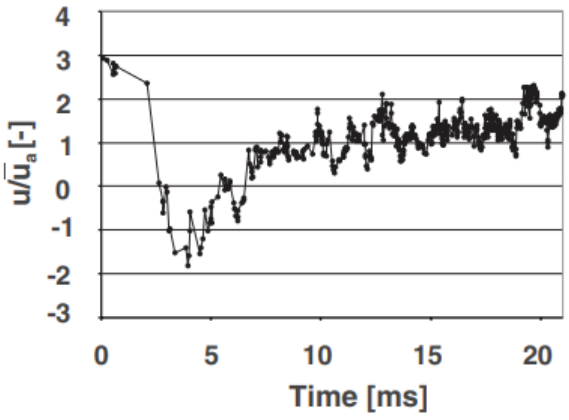

Figure 3.21: Axial velocity measurements at a point on the axis of the mixing zone over a span of time, from Fritz et al. [41]

Kiesewetter et al. [59] performed 2D flashback simulations using URANS-RSM turbulence model and EBU for combustion. In 2D, The swirler was modelled using the source term of angular momentum equation. The simple 2D model captured the CIVB flashback mechanism seen in the experiments of Fritz et al. [41]. Later, Kiesewetter et al. [58] performed a vorticity analysis with the vorticity transport equation and Schmidt flame speed model of 3D flashback simulations. Azimuthal vorticity due to stretching and tilting was found to be high compared to other terms of the vorticity transport equation. However, for different ϕ cases, no significant differences were seen in their magnitude. This indicates that the stretching and tilting term is not responsible for flashback. The expansion term is said to have a positive effect, i.e. positive azimuthal vorticity creation like the stretching and tilting term. So the baroclinic is the only term responsible for negative azimuthal vorticity creation.

To understand the initialization of flashback, Kiesewetter et al. [58] analyzed the flow field of flashback safe and prone cases for identical ϕ. The root cause for the initialization of flashback was attributed to the position of the flame concerning the stagnation point of the recirculation bubble. In an unstable configuration figure 3.22 (a), the reaction zone was found to be within the RZ and near the stagnation point. Hence, the negative vorticity creation due to baroclinic torque paved the way for the upstream flame propagation. For the safe configuration figure 3.22 (b), the reaction zone was found to be upstream of the stagnation point. Therefore, the positive induced velocity aided in inhibiting the upstream flame propagation even though the vorticity creation of baroclinic torque was high.

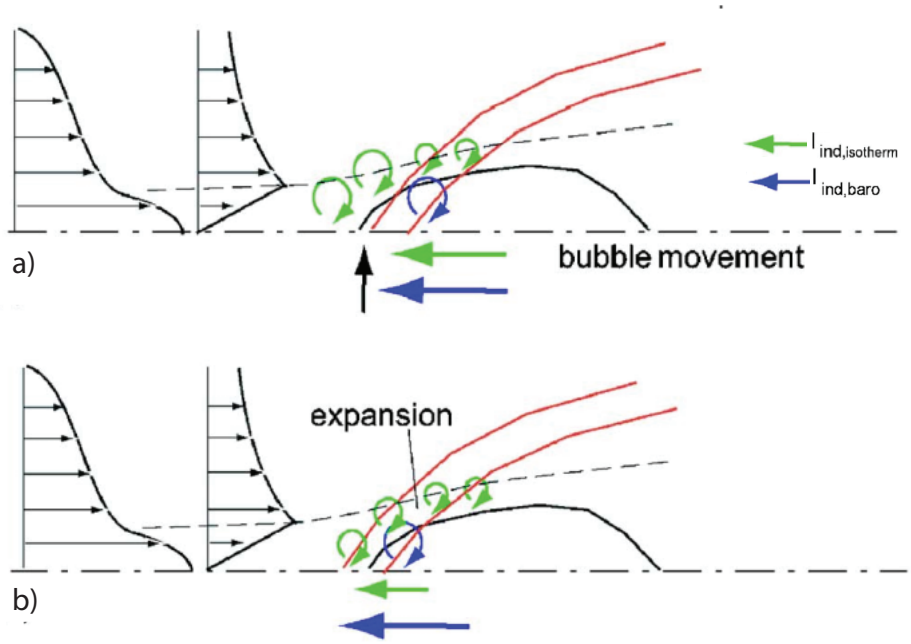

Figure 3.22: Schematics representation of the Combustion Induced Vortex Breakdown (CIVB), (a) depicts the flashback prone case and (b) depicts the flashback safe case, adapted from Ref. [58]

A similar kind of behaviour of the flame was also confirmed by the experimental investigation by Konle et al. [63]. Therefore, the flame propagation is governed by the recirculation tip and the position of the reaction zone, which in turn is governed by the chemistry of the combustion. This CIVB flashback mechanism is not limited to a single geometry, the mechanism is said to happen in other burners with the centre body as well [93], irrespective of the fuel.

3.5.2. Flame flashback in LSI

Although there are many literature studies about LSI, only a handful of studies addressed flame flashback in LSI. Cheng et al. [19] measured the flashback limit of H_2 enriched fuels by increasing ϕ and keeping vol.% of H_2, U_0, T_0 and P_0 constant until the occurrence of flashback. table 3.1 shows the conditions at which flame flashback occurred. The flame flashback was not encountered in the 'v' shape lifted flame reported by Johnson et al. [54] and Cheng and Littlejohn [20]. This implies that burning in OSL, which produces an 'M' shape flame, might be the reason for a flame flashback. However, the origin of flashback was inconclusive due to limited flashback experiments. The LSI has less propensity towards the occurrence of flashback when compared to HSI, which was attributed to the less turbulent fluctuation in the shear layers of LSI. From the visual investigation of flame done by Cheng et al. [19] it was presumed that the flashback did not originate in the nozzle wall but rather in the region of high turbulent fluctuations.

Case	$H_2(vol.\%of)$	$P_0(MPa)$	$T_0(\ K)$	$U_0(m/s)$	ϕ_{FB}
1	100	0.202	530	20	0.5
2	100	0.202	550	30	0.57
3	87	0.405	560	20	0.52
4	100	0.405	570	30	0.4
5	82	0.810	575	20	0.49
6	92	0.810	575	20	0.42

Table 3.1: Flashback limits ϕ_{FB} measured by Cheng et al. [19] for various inlet conditions

Beerer et al. [7] investigated the flame flashback in LSI. Flashback was established analogous to the method employed by Cheng et al. [19] and the fuel supply was terminated once the flashback was encountered. The figure 3.23 shows the pressure drop and axial velocity measurements performed by Beerer et al. [7] at a point in the centre line 15 mm downstream of the dump plane during the event of a flame flashback.

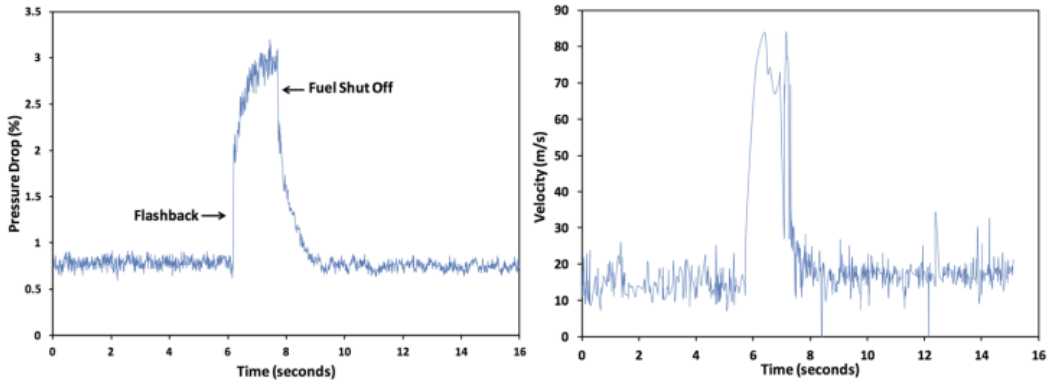

Figure 3.23: Pressure drop and axial velocity measurements at the point on the axis, 15 mm downstream the dump plane during the course of flashback, adapted form [7]

The sudden rise in axial velocity indicates the occurrence of flashback since the burned gas with low density should have high velocity according to the continuity equation. Once the fuel was terminated, the velocity and pressure drop recovered to their nominal range. Upon comparing both the figure 3.21 and figure 3.23, it is evident that the axial velocity in figure 3.23 remained positive over the span of the flashback event, unlike figure 3.21. Hence, it is intuitive that CIVB flashback mechanism is not responsible for flashback in LSI. The absence of pressure drop fluctuation in figure 3.23 suggests that flashback due to instabilities is implausible. Beerer et al. [7] examined the injector after the experiments and noticed a charred perforated plate which indicates the attachment of flame to the perforated plate consequent to flashback. In addition, the rise in axial velocity was attained in a short span of time, thus, indicating a sudden occurrence of flame flashback.

Therkelsen et al. [121] recorded the flame flashback in a high-speed video camera and confirmed the flashback originated in the core of the flow, even though the convective flow speed was much higher than the flame speed. Therkelsen et al. [121] credited the ISL for the flame flashback. Therkelsen et al. [121] suggests employing a tapered centre channel wall and decreasing the swirl angle to reduce the turbulent fluctuations, which might aid in addressing the flame flashback.

3.6. Previous numerical studies on LSI

Pitsch [98] developed a model to simulate the LSI, similar to the LSI used by Cheng and Littlejohn [20]. Initially, Pitsch [98] did a cold flow (without combustion) simulation with air to evaluate the correctness of boundary conditions. Upon validating the velocity plots obtained from the experiments of Cheng and Littlejohn [20]. It was found that the simulation performed well in predicting the cold flow characteristics observed in the experimental studies of Cheng and Littlejohn [20] and Johnson et al. [54]. A unit Lewis number fuel, methane, was employed to simulate reacting flows. Pitsch [98] initially resolved the flow through the nozzle with 8 million cells, and then the simulation result was used as an inlet boundary condition to simulate the combustion chamber. Pitsch [98] noticed a highly unsteady and nonuniform flow in the nozzle. The simulation of the combustion chamber produced an 'M' shaped attached flame (see figure 3.24), and the simulation performed well in capturing the flow details mentioned by Cheng et al. [19]

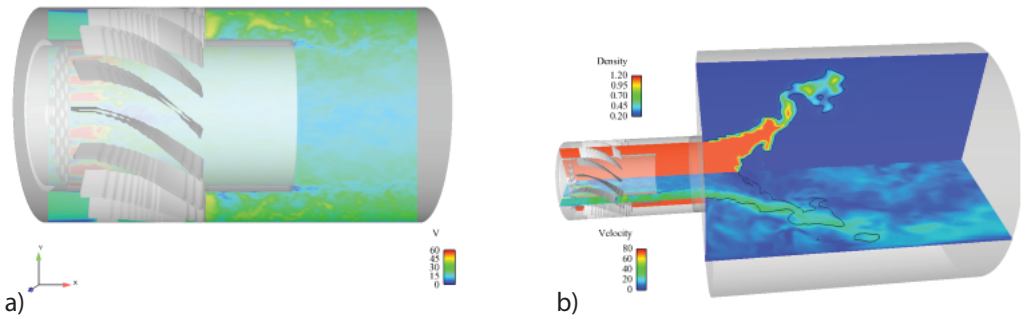

Figure 3.24: Instantaneous velocity contour of the injector from the simulation of lean premixed methane with $\phi = 0.59$ (a) and instantaneous density and velocity contour of from the simulation of lean premixed methane with $\phi = 0.59$ including the injector and the combustion chamber (b) from Ref. [98]

Pitsch [98] looked into flame flashback and he performed simulations for the flashback condition mentioned by Cheng et al. [19]; see table 3.1. Flashback was never observed in the simulations performed by Pitsch [98] for the cases mentioned by Cheng et al. [19] (case 1 and 2 in table 3.1). Even for ϕ = 0.6, flashback was never encountered in simulations. Pitsch [98] presumes that considering the non-unit Lewis number effect might lead to flashback. The other numerical studies on LSB in the literature are summarized in table 3.2 along with their computational methods and crucial observations.

Study	Computational Method	Observations and Remarks
Pitsch [98]	3D LES - Combination of level set G equation and progress variable	Simulated the nozzle and combustion chamber separately; Absence of flashback occurrence
Muppala et al. [87]	3D RANS - premixed turbulent flame speed closure model of Zimont (3.26) and AFSW model (3.32)	AFSW model performed well in predicting the hydrogen-enriched flames
Neumayer and Hirsch [91]	2D RANS - premixed turbulent flame speed closure model of Zimont (3.26)	2D model, velocity components specified separately to swirler and centre channel; EDC failed to predict the flame shape seen in experiments
Ranzijn [103]	RANS - 3D premixed and partially premixed turbulent flame speed closure model of Zimont	$k-\omega$ model performed well in modelling the turbulence; Simulation of unenclosed LSI produced a lifted flame

Table 3.2: Summary of numerical studies on LSB

Based on the numerical and experimental studies available in the literature, observations relevant to the study were discussed in this chapter. Apparently, only a few numerical studies of LSB mentioned in table 3.2 were available, and none of them investigated the occurrence of flashback in LSB. Nobody has reported the occurrence of flashback in their numerical studies. Thus, the flashback prediction in LSB is still an unaddressed question.

Based on the knowledge obtained from the literature, a computational model will be created, and numerical simulations will be performed with RANS and flamelet combustion model (TFC and AFSW) to study the reacting flows in LSB. In addition, the results from the numerical simulation will be validated with the available experimental and numerical results discussed in this chapter.

4

Numerical setup

This chapter discusses the experimental aspects and details of the chosen LSI's for numerical modelling, followed by the numerical setup of the computational domain. In the next sections, the mesh and the numerical methods used in the simulations are briefed.

4.1. LSI burner description

From the literature study, it is evident that there are a plethora of LSI burners; each one has its distinct experimental configurations and LSI geometry. This study selected the experimental setup and LSI of Cheng and Littlejohn [20] for numerical modelling. The reason for choosing this specific setup is because of the detailed information available about the combustion chamber and LSI geometry. In addition to that, the experimental study was performed with an enclosure. The schematics of the experimental setup are shown in figure 4.1.

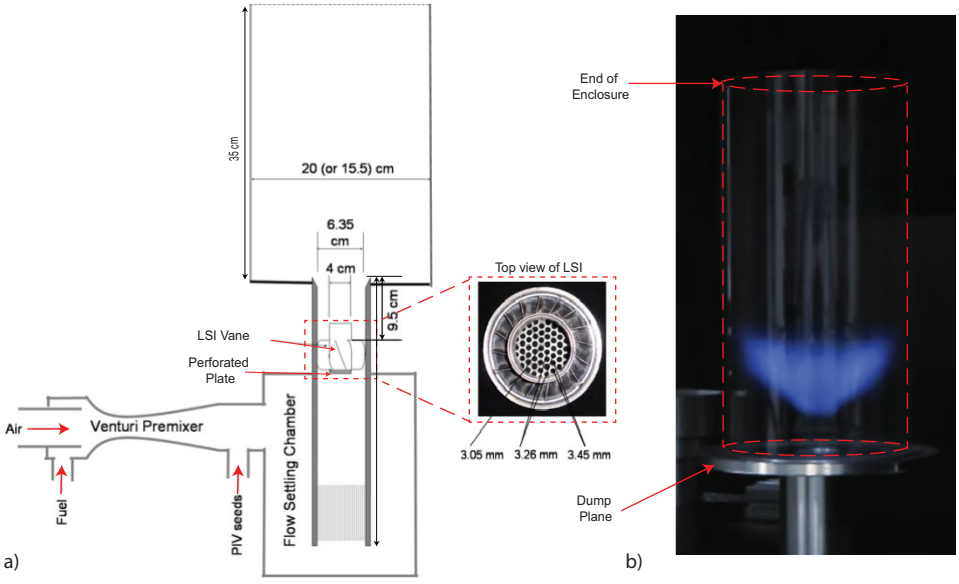

Figure 4.1: 2D Schematics of the experimental setup with dimensions not drawn to the scale (a) and Flame produced in the LSI experimental setup (b), adapted from [20]

.

From the experimental setup shown in figure 4.1 (a), it is evident that a homogeneous mixture of air and fuel is provided to the nozzle with the aid of a venturi premixer. The burner is divided into two parts: the nozzle, which consists of LSI with a diameter of 6.35 cm and a quartz enclosure with a diameter of 20 cm. The LSI is placed inside the 30 cm long nozzle at 5 cm upstream from the nozzle exit, whereas the vanes are recessed 9.5 cm from the nozzle exit. From the nozzle exit, a quartz cylinder extends up to 35 cm, and at the exit of the enclosure, no constrictions were placed. Hence the flow after the enclosure is flowing to the environment. The nozzle is chamfered at the exit to assist the swirling flow divergence.

The LSI employed in the experimental study of Cheng and Littlejohn [20] consists of sixteen vanes with a vane angle of 40. The LSI consist of a centre channel of 4 cm diameter (R = 0.63), which includes a perforated screen with varying hole perforation. The perforation of the centre hole has a diameter of 3.05 cm, the second and third-row consist of holes with a perforation diameter of 3.26 cm and the fourth and fifth has a large diameter of 3.45 cm, as shown in the bottom view of LSI in figure 4.2 (a). With the variable perforation diameter, the LSI had a swirl number (S) of 0.51.

The above-described LSI is used for validating and studying the non-reacting flow simulations of the LSI burner but for studying the reacting flow field, the different combustion chamber and LSI geometry employed by Cheng et al. [19] is used since the non-reacting flow field was not studied by Cheng et al. [19]. The diameter of enclosure, nozzle, and centre Chanel of the experimental setup of Cheng et al. [19] were 18 cm, 5.715 cm and 3.772 cm (R =0.66) respectively. The swirler was recessed 4.6 cm from the nozzle exit plate, which is shorter than the recess length employed by Cheng and Littlejohn [20]. The vane angle and S remained the same for both the flow configuration as seen in figure 4.2 (b) and (d). But the uniform perforation of 3.5 mm and non-chamfered nozzle exit was used in the experimental setup of Cheng et al. [19]. The uniform perforation of LSI's centre channel is shown in figure 4.2 (c).

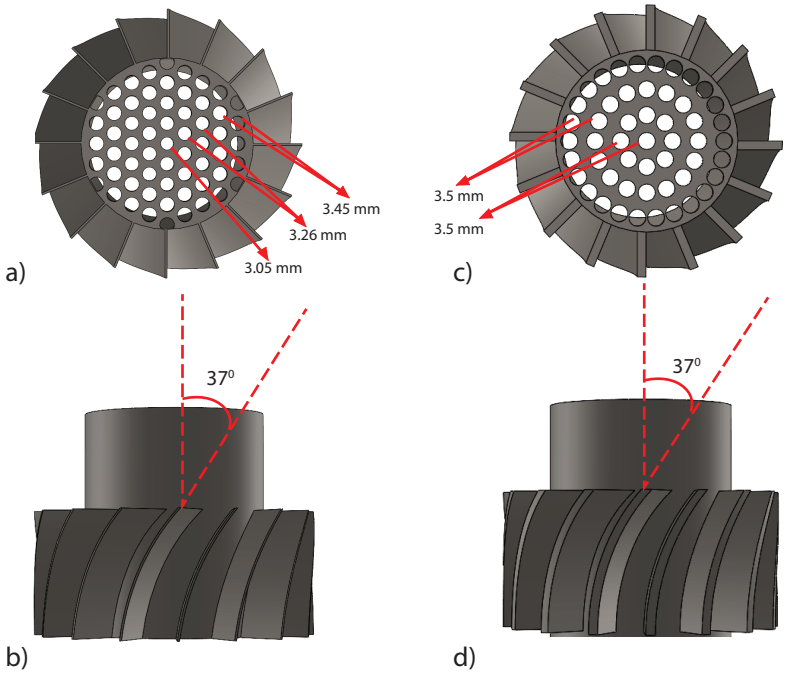

Figure 4.2: Bottom and side view of LSI of Cheng and Littlejohn [20] (a) & (b) and Cheng et al. [19] (c) & (d) respectively, modelled in Solidworks 2021.

4.1.1. Computational Domain

The flow domain of the physical system was extracted to study the flow fields of the system. Since the LSI consists of vanes and perforated plates, the computational flow through the LSI can only be modelled in 3D. Whereas the combustion chamber's computational domain (enclosure) can be modelled in 2D. The 3D computational domain of the LSI burner setup is shown in figure 4.3 (a), and its 2D projection is also shown in figure 4.3 (b), excluding the LSI part. Neumayer and Hirsch [91] performed a 2D simulation by avoiding the complex LSI geometry, considering only the downstream portion of LSI as a computational domain as shown in figure 4.3 (b).

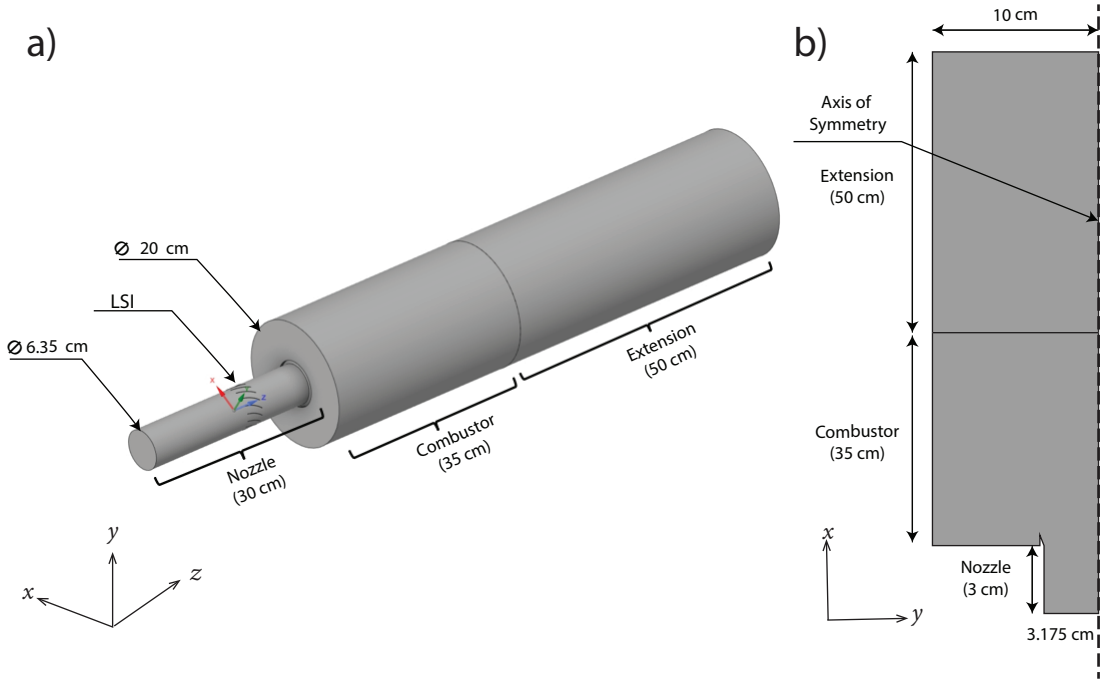

Figure 4.3: Computational domain in 3D with LSI (a) and 2D computational domain without LSI signifying the experimental setup of Cheng and Littlejohn [20]

Initially, the computational domain of the combustor and nozzle was modelled in 3D to investigate the non-reacting flow fields. The presence of reverse flow was identified in the simulations at the outlet. The occurrence of reverse flow is not desirable since it affects the convergence and accuracy of the simulations. The reason for the reverse flow is explained in subsection 4.3.2. Therefore, an extension to the combustor is used to simulate both non-reacting and reacting flows, as shown in figure 4.3 (a). The extension has the same diameter as the combustor, with a length of 50 cm.

Later, to save computation time, a 2D combustor model was modelled, neglecting the LSI geometry for simulating the reacting flows. The main difference between the 3D (figure 4.3 (a)) and 2D (figure 4.3(b)) computational model is that the LSI is not modelled in 2D; instead, the swirling flow is specified based on the simulation data obtained from the 3D simulation (figure 4.3 (a)), more about this will be discussed in subsection 4.3.2. Apart from the two computational models shown in figure 4.3, the 3D model without LSI is also used for simulations (domain created by sweeping the 2D domain shown in figure 4.3 (b) about the axis of symmetry). The meshing strategy employed to create a mesh of LSI geometry is explained in the next section.

4.2. Meshing

The extracted flow domain of the system should be divided into smaller cells in the form of geometric shapes like triangles and quadrilaterals in 2D and hexahedrons, tetrahedrons and prisms in 3D to solve the discretised governing equations in each one of them. This study used ANSYS meshing and ICEM CFD 2021 R2 for mesh generation. The meshing methodologies employed for non-reacting and reacting flow simulations are discussed in detail in Appendix C

4.3. Simulation setup

In this section, the steps and methods involved in setting up the premixed combustion simulation of the LSI burner are briefed. The non-reacting and reacting flow simulations were performed in ANSYS Fluent 2019R3. The combustion parameters required to set up the reacting flow simulations were calculated using Cantera 2.6.0 [43] in python.

4.3.1. Combustion parameters

The mixture properties required to set up the reacting flow simulation are calculated using Cantera 2.6.0 in python. The multi-component transport model available in Cantera is used to calculate mixture properties along the standard GRI 3.0 reaction mechanism. The thermodynamic properties of the fuel mixtures, unburnt density (ρ_u), dynamic viscosity (μ), specific heat capacity at constant pressure (C_p) and thermal conductivity (k) are calculated from the *ThermoPhase* class available in Cantera [43] for the specified initial temperature and pressure. The thermal diffusivity of the mixtures can be calculated from equation 4.1.

$$\alpha = \frac{k}{\rho_u C_p} \tag{4.1}$$

AFT is calculated from the Gibbs free energy formulation. The AFT computed using this method is more accurate than the other methods [68] since it considers the dissociation reactions in the reaction mechanism. Gibbs's free energy is determined using the equation 4.2.

$$\Delta G = \Delta H - T\Delta S \tag{4.2}$$

The S_L^0 is the important property of the fuel mixture. It is determined by solving the ordinary differential governing equation for 1D freely propagating flat flame for the specified initial temperature and pressure. The Lewis number (Le) calculation of the fuel mixtures differs from study to study. In this study the method proposed by the Dinkelacker et al. [29] as defined in equation 3.33 is used for calculating Le. The in-flow conditions and properties for five different methane and hydrogen fuels mixtures are given in table 4.1.

	phi (ϕ)	H_2 $vol\%$	CH_4 $vol\%$	ρ_u (kg/m^3)	AFT (K)	Le_{eff}	S_L^0 (m/s)	α x 10^{-5} (m^2/s)	ν x 10^{-5} (m^2/s)
Flame 1	0.59	0	100	1.13	1610	0.96	0.104	2.00	1.61
Flame 2	0.4	40	60	1.11	1416	0.498	0.069	2.16	1.65
Flame 3	0.4	60	40	1.1	1495	0.402	0.116	2.30	1.66
Flame 4	0.4	80	20	1.06	1557	0.336	0.193	2.55	1.71
Flame 5	0.4	100	0	1	1614	0.29	0.302	3.05	1.81

Table 4.1: Experimental inflow conditions for reactive flow simulation from [19]

4.3.2. Boundary conditions

The boundary conditions are determined based on the experimental setup shown in figure 4.1. The flow in the computational domain is defined at the nozzle inlet as *velocity inlet* where the bulk velocity (U_0) is specified. The fluid enters the computational domain through the nozzle, swirl in the flow is created as a result of LSI. Due to the suddenly expanding geometry, the swirl flow radially diverges in the combustion chamber and leaves the domain through the outlet surface.

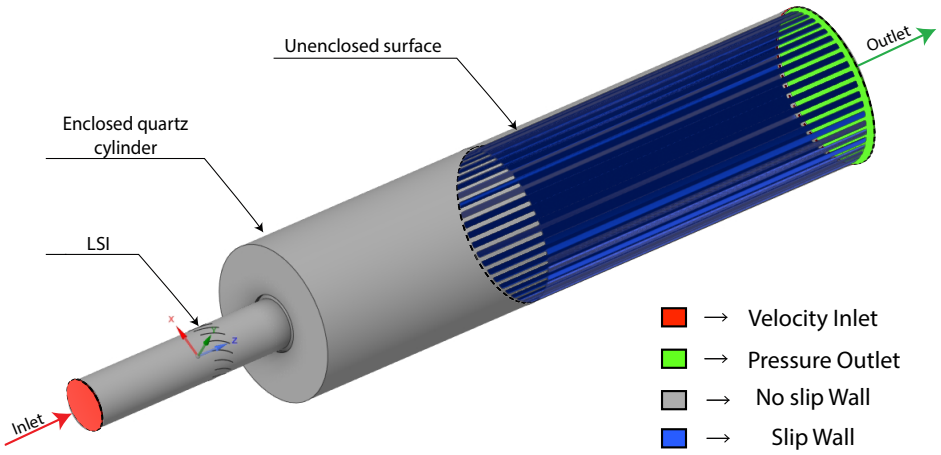

Figure 4.4: Location of boundary conditions

The conditions at which the flow exists in the domain are unknown from the experiments, so implementing the Dirichlet boundary condition at the outlet is challenging for the swirling flows. From the figure 4.3, it is evident that the flow is leaving from the enclosure to the environment, so applying the *Pressure outlet* boundary condition will be a valid assumption. The *Pressure outlet* requires static pressure (P_s) to be specified at the outlet face. Initially, a zero gauge pressure was set at the outlet of the enclosure (without extension), but this produced reverse flow in the domain where a small pocket of fluid flow was entrained into the domain through the outlet. The flow reversal is due to the adverse pressure gradient created near the outlet, which is, in turn, due to imposing a uniform static pressure at the outlet face. Swirling flow is said to have radial pressure distribution, and the streamlines are helical, so imposing a *Pressure outlet* will force the swirling streamlines to straighten out.

Outflow is the other option available in Fluent, which can be specified at the outlet of the model. This boundary condition is applied when the gradient of all the variables normal to the direction is zero. This is imposed when one knows the solution is completely developed and flow variables are not changing across the flow direction. For swirling flows, the normal gradient of the flow variables to be zero usually requires a very long domain, increasing the computational cost.

So an extension domain representing the atmosphere is implemented with *symmetry* boundary condition where flow variables will have the same value and gradients. These conditions at the boundary will make the streamlines straight, and then the zero gauge pressure outlet can be specified at the extension outlet *Pressure outlet*.

The *No slip* wall boundary condition is imposed on the LSI injector and to the walls of the nozzle and the combustion chamber (enclosed quartz cylinder). For turbulent inflow conditions, the condition assumed by Muppala et al. [87] is used, which are turbulent intensity and length scale of 5% and 0.001 m, respectively.

4.3.3. Solution methods

The partial differential governing equations are initially discretised into algebraic equations in the form of a matrix, and these algebraic equations are solved to get a numerical solution based on the conditions imposed at the boundary. Many discretization schemes and solvers are available in Fluent to discrete and solve those discretized equations, respectively.

The cell-centred Finite Volume Method (FVM) available in Fluent is used in this study. In FVM, the flow variable is discretised by integrating the momentum governing equations over each control volume or cell. These discretised coefficients of the flow variables are stored at the cell centre. However, for discretisation, one requires the face value of the cells, which is obtained by interpolation. The interpolation is accomplished by using an upwind scheme. The discretised equations containing both the pressure and velocity term are solved sequentially (SIMPLE, SIMPLEC, PISO) or simultaneously (Coupled) to obtain a numerical solution.

In this study, the pressure-based solver is used since the density is not varying with pressure, and combustion happens at a low mach limit. Coupled solver is used to solve the coupled discretised equation. Though the computation time required is higher than the segregated solver, coupled solver produces a robust solution with fewer iterations. The least-square cell-based scheme is used for spatial discretisation of gradients since it results in a stable numerical solution with less computational time when compared to other methods. The PRESTO scheme is employed for pressure interpolation at the cell faces since it is recommended for swirling flows [44]. The discretisation schemes used to discrete the momentum, turbulence and progress variable equations are discussed in the next section.

4.3.4. Simulation strategy

The simulation strategy followed to get stable and converging steady-state numerical solutions to the reactive swirling flows simulations are mentioned below.

1. Initially, the non-reacting simulations were performed, followed by the reacting flow simulation
2. First order upwind discretisation schemes were selected to discretise momentum and turbulence equations
3. The non-reacting flow variables were initialised using Hybrid initialisation
4. The residuals were set to 10^{-5} for all the flow variables. In addition, the convergence was also judged by the net mass flux between the outlet & inlet.
5. When the net mass flux between the outlet & inlet is below 10^{-6} and residuals of all the flow variables reach below 10^{-5}, the progress variable combustion equation is included to solve along with the continuity, momentum and turbulence equation.
6. The progress variable was initialised with the burnt state over the whole domain by patching C as 1.
7. The discretisation schemes were changed from first-order upwind to second-order upwind for all the flow variables, including the progress variable.
8. When the mass flux difference between the outlet & inlet reaches below 10^{-9}, it was assumed that the simulations had reached a steady state.

The above steps were performed sequentially for steady-state reactive flow simulations.

5

Validation of Numerical Results

This chapter discusses the results of the RANS simulations performed on the LSB. First, the non-reacting flow simulation results are discussed, where the meshes of the computational model are investigated for non-reacting flows, followed by the validation with different turbulence models. The results of the reacting flow simulations of lean premixed mixtures are discussed in the next section, along with their validation performed over experimental measurements. In addition to that, the shortcomings of the combustion model are briefed.

5.1. Non-reacting flow simulation

This section discusses the results obtained from the non-reacting flow simulations. The computational model resembling the experimental setup of Cheng and Littlejohn [20] and the LSI-N1 meshing technique mentioned in Appendix C is used throughout this section. The steady-state simulation methods and strategy discussed in the previous section were implemented, excluding the inclusion of the combustion transport equation. The governing equations discussed in chapter 2 were solved numerically in the Cartesian coordinates system.

5.1.1. Grid independence study

The accuracy of the simulations depends mainly on the mesh used in the simulations. Therefore it is necessary to perform a mesh independence study for a specific problem to check whether the solutions rely on the mesh. The bulk velocity (U_0) of 10 (m/s) is specified normal to the inlet for all meshes stated in table 5.1 as an inlet boundary condition. The k-ω - SST turbulence model was chosen to model the turbulence irrespective of mesh. The mesh was refined one-and-a-half times from that of the previous coarse mesh, approximately. The structured mesh was refined axially, tangentially and radially in the structured volume parts of 2, 3 and 4 as shown in figure C.1. Since the flow gets divided in the LSI, a significant pressure drop is experienced across the injector; therefore, the size of the elements in the vicinity of LSI was also decreased as the structured mesh was refined.

Since the flow field region near the nozzle exit is of interest in this study, the axial velocity along the axis centre line (z-axis) was chosen to investigate the mesh dependence. From figure 5.1, it is evident that all the mesh produced similar results except the coarsest *Mesh A*. All the meshes predicted the formation of reversal flow in the combustion chamber, but the estimation of the position of the stagnation point ($U_0 = 0m/s$) of flow reversal was different. Compared to other meshes, the *Mesh A* predicted the stagnation point near the dump plane. The stagnation point of the other mesh was approximately found at the exact axial location.

Mesh size	Number of element	Element size in LSI
A	0.52 M	2.5 mm
B	1.1 M	2 mm
C	1.6 M	1.5 mm
D	3 M	1 mm

Table 5.1: Mesh independence study

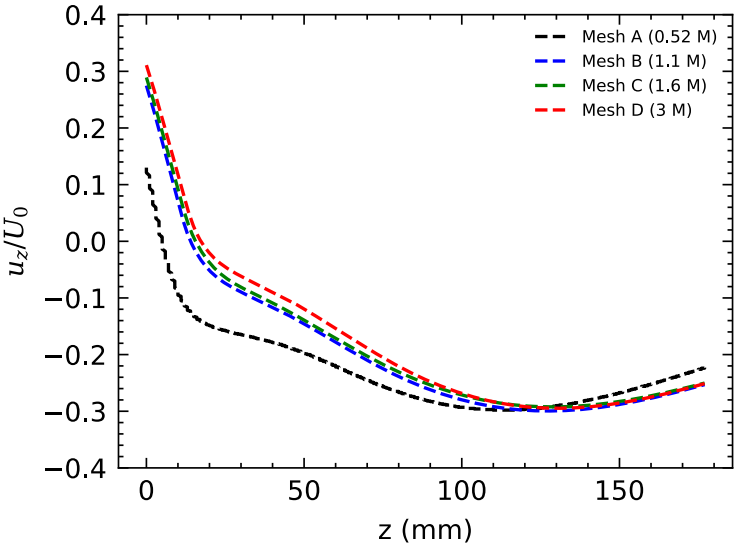

Figure 5.1: Axial velocity along the centre line (Z -axis), normalised with the inlet bulk velocity U_0 $(10\ m/s)$ from the dump plane (Z =0) for different meshes in table 5.1

The mesh independence based on figure 5.1 is challenging to decide for swirling flows since the axial velocity along the centre axis only ensures the independence of axial divisions in the mesh. Therefore, radial profiles of axial and radial velocity normalised with U_0 at 6.5 mm from the dump plane are also considered to determine the mesh independence.

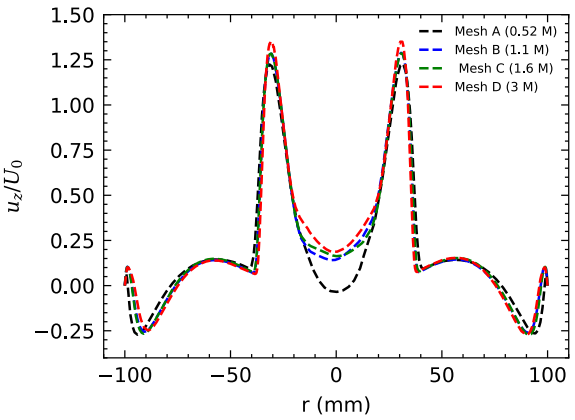

Figure 5.2: Axial velocity normalised with the inlet bulk velocity U_0 $(10\ m/s)$ along the radial line at Z = 6.5 mm.

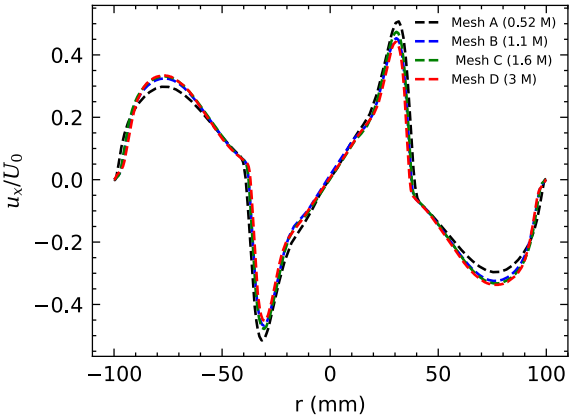

Figure 5.3: Radial velocity normalised with the inlet bulk velocity U_0 $(10\ m/s)$ along the radial line at Z = 6.5 mm.

From figure 5.2 it is evident that the formation of stagnation point was found to be much before z = 6.5 mm from figure 5.2. The figure 5.3 shows the mesh independence in the radial direction for all the mesh, with *Mesh A* having significant maximum and minimum differences compared to other mesh radial velocity profiles. The difference in the velocity profiles shown in figure 5.1, 5.2 and 5.3 of *Mesh B, C and D* were found to be insignificant, so considering the computational time in mind *Mesh B* with 1.1 million cells was employed in all the non-reacting flow simulations.

5.1.2. Validation of Non-reacting flow

Before proceeding with the reacting flow simulations, all the two-equation turbulence models except RSM discussed in Appendix B were evaluated for non-reacting flows with standard wall functions (only for standard k-ϵ) to check the capability of modelling the turbulence correctly since the swirling flow field is complex. Velocity profiles obtained upon simulating the non-reacting flow for all the turbulence models were compared with the experimental measurements of Cheng and Littlejohn [20] with Reynolds number (Re) equal to 4.3 x 10^4 based on the inlet diameter D (6.35 cm) of the nozzle. The figure 5.4 shows the axial velocity normalised with an inlet bulk velocity of 10 (m/s). Upon comparing the velocity profiles of all the turbulence models with experimental measurements as seen in figure 5.4, the stagnation point of all the turbulence models lying slightly upstream concerning the measured stagnation point except k-ω - SST, While standard k-ϵ being the far upstream as seen in figure 5.4. All the turbulence models over-predicted the flow velocity in the recirculation zone (50 < Z < 100 mm), which is also seen in simulations of [88] with equivalent LSI burner configuration. These errors were attributed to the turbulence calculations by steady-state RANS models. In reality, the swirling flow exhibits an unsteady behaviour in the central flow reversal zone due to PVC.

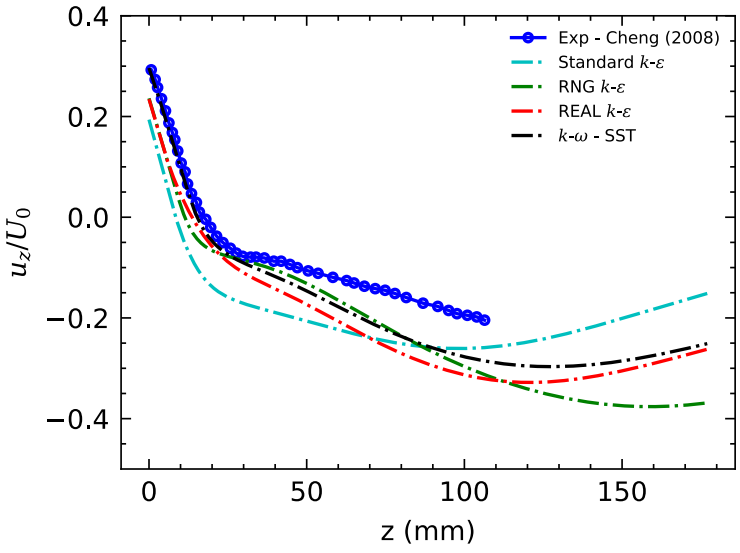

Figure 5.4: Axial velocity along the centre line (Z-axis) from the dump plane (Z = 0 mm) normalised with the inlet bulk velocity U_0 ($10\ m/s$) of different turbulence models, validated with the experimental measurements of Cheng and Littlejohn [20]

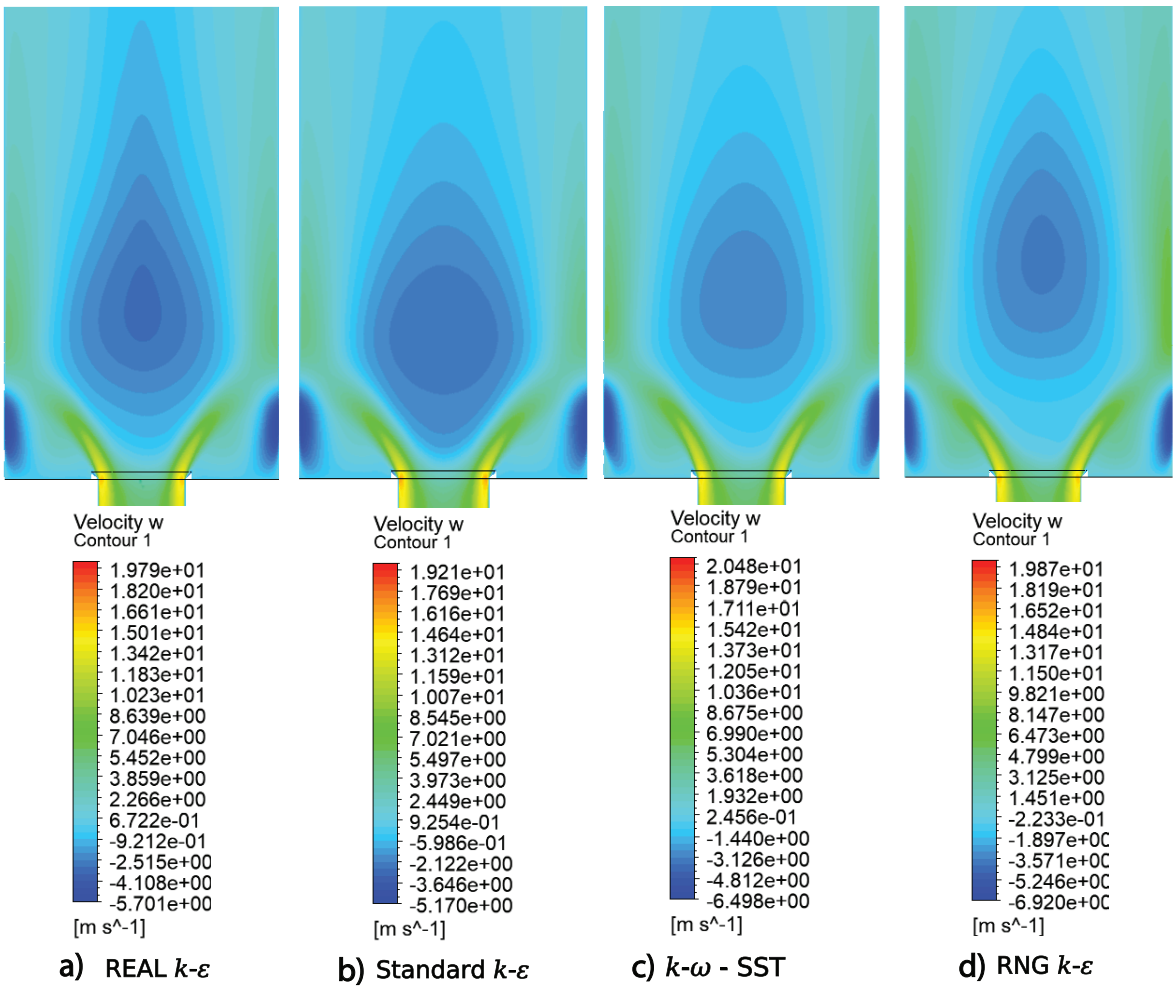

Figure 5.5: Axial velocity contour of non-reacting flow with four different turbulence models

The measured axial velocity profiles of Cheng and Littlejohn [20] seen in figure 5.6 shows a slight asymmetry. Hence, the computational studies of Neumayer and Hirsch [91] and Muppala and Vasudevan [88] validated their results from r = 0 to 100 mm, neglecting the velocity profiles of another half of the domain. Similarly, the radial velocity profile seen in figure 5.7 was also neglected for comparison due to the huge asymmetry. The reason for the huge asymmetry seen in the experimental measurements of radial velocity (figure 5.7) is not mentioned explicitly in literature. However, the asymmetry behaviour might be due to asymmetric flow features like PVC. The peak value seen in figure 5.6 results from shear layers between the recirculation zones seen in figure 5.5. The velocity deficit seen in the central region (-20<r<20 mm) is due to flow divergence. The divergence experienced by the flow is also intuitive from the steep slopes of radial velocity profiles (figure 5.7) seen in the central region (-20<r<20 mm). The peak values of axial velocity seen in figure 5.6 agree well with the experiments, and axial velocity in the central region was under-predicted by all the turbulence models.

The figure 5.5 shows the contours of axial velocity of different turbulence models, the recirculation zone formed as a result of vortex breakdown differs in magnitude and reattachment axial location of the bubble. The maximum negative velocities were seen in the ORZs than the IRZ in all turbulence models. The IRZ of the standard k-ϵ model was more upstream than other turbulence models.

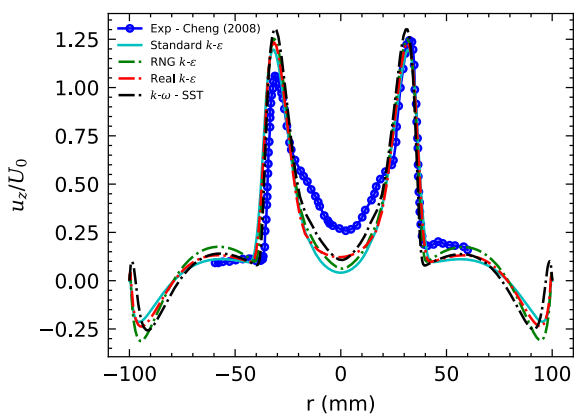

Figure 5.6: Axial velocity normalised with the inlet bulk velocity U_0 $(10\ m/s)$ along the radial line at 6.5 mm from the dump plane, obtained from the simulations of different turbulence models, validated with the experimental measurements of Cheng and Littlejohn [20]

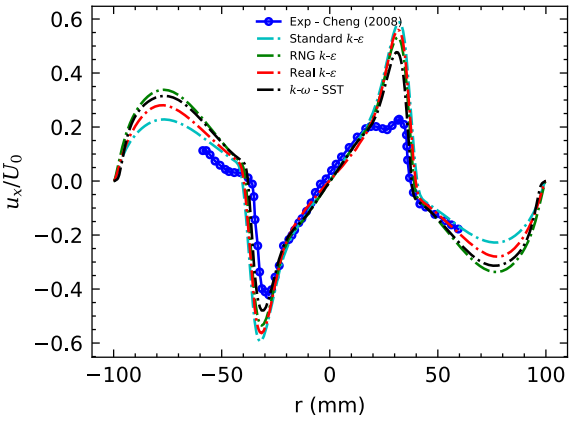

Figure 5.7: Radial velocity normalised with the inlet bulk velocity U_0 $(10\ m/s)$ along the radial line at 6.5 mm from the dump plane, obtained from the simulations of different turbulence models, validated with the experimental measurements of Cheng and Littlejohn [20]

Though the IRZ of the RNG k-ϵ and k-ω - SST look identical, the axial velocity in the IRZ and CRZ was found to be over-predicted in RNG k-ϵ turbulence model when compared with experimental measurements. The comparison of axial and radial velocity profiles along the radial axis also shows that the k-ω - SST turbulence model agreed better with the experimental data. Therefore, upon comparing the velocity profiles and contour plots of non-reacting flows, the k-ω - SST model was able to correlate well with the experimental data than other turbulence models. Hence, the k-ω - SST turbulence model will be used for further simulations.

5.1.3. Two-Dimensional Vs Three-Dimensional

The non-reacting flow field of LSB seems to be nearly axisymmetrical from the axial velocity contours in figure 5.5. Therefore, two-dimensional simulations were performed to compare them with the three-dimensional simulations, qualitatively. The computational domain and the mesh of the two-dimensional domain with 7.3 x 10^4 quadrilateral cells are shown in figure 4.3 (b) and figure C.5 respectively. The two-dimensional mesh size was smaller than the three-dimensional by two orders of magnitude, resulting in less computational time. Hence, the non-reacting swirling flow was analysed in two dimensions, neglecting the derivatives concerning the tangential (or) azimuthal direction. The two-dimensional axisymmetrical turbulent swirling flow governing equations in Appendix A is solved numerically in the cylindrical coordinate system.

The inlet boundary condition required for the two-dimensional simulation was adapted from the three-dimensional simulations. The axial and tangential components of the velocity taken from the three-dimensional simulations of the k-ω - SST turbulence model at 10 mm (see figure 5.8) downstream of LSI were specified at the inlet along with turbulence parameters while radial velocity was set to zero. A similar kind of methodology of velocity profile definition as inlet conditions for swirling flows was also used in the numerical simulations of Alahmadi et al. [4]. figure 5.9 shows the plot of applied velocity profiles at the inlet of the two-dimensional domain.

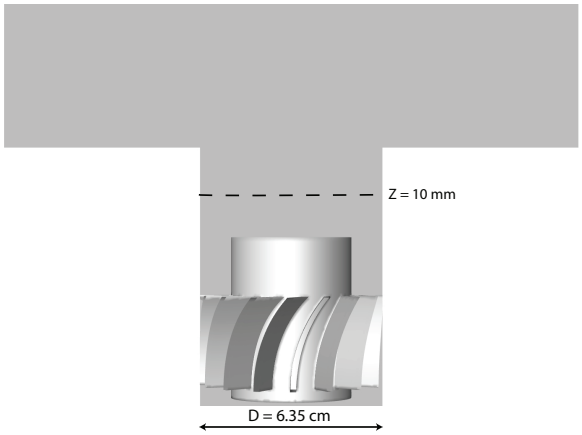

Figure 5.8: Schematics of the radial line location (Z = 10 mm) where the velocity and turbulent profiles are taken from the three-dimensional simulation for the two-dimensional simulation

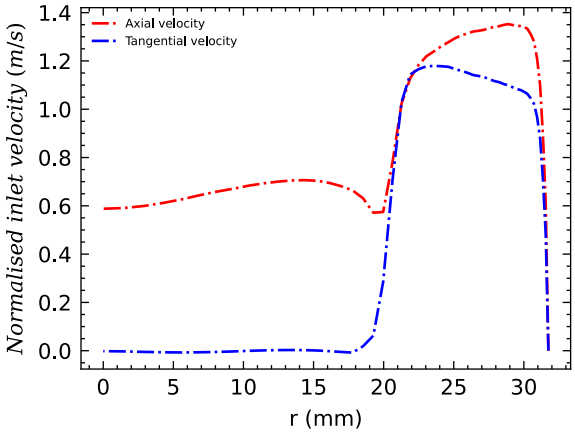

Figure 5.9: Axial and tangential velocity, normalised with the inlet bulk velocity, U_0 $(10\ m/s)$ specified at the inlet of the two-dimensional computational model, obtained from the three-dimensional simulation at 10 mm downstream of LSI

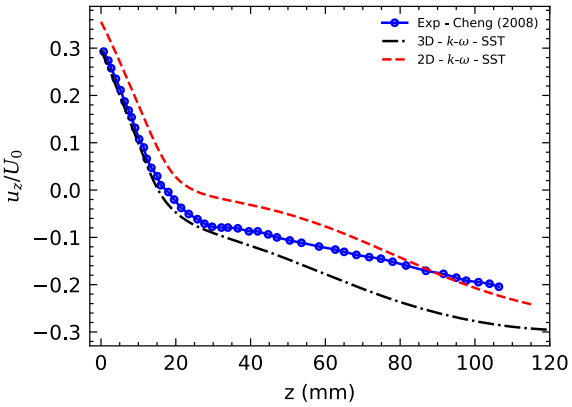

Figure 5.10: Axial velocity along the centre line, normalised with the inlet bulk velocity U_0 $(10\ m/s)$ at 6.5 mm from the dump plane

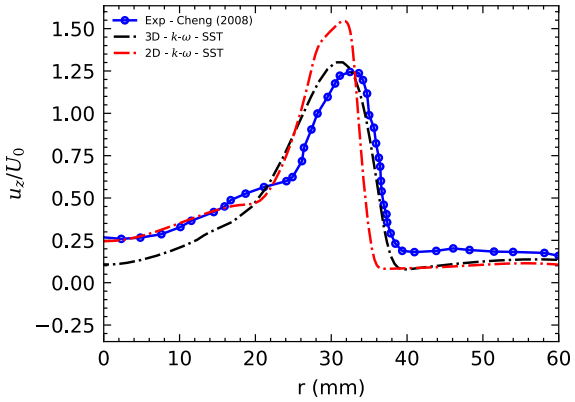

Figure 5.11: Axial velocity normalised with the inlet bulk velocity U_0 $(10\ m/s)$ along the radial line at 6.5 mm from the dump plane

From figure 5.9, it is evident that the tangential velocity component is present only in the annular region (r > 20 mm), and the axial velocity along the central channel (0 < r < 20 mm) almost remained constant at 10 mm downstream of LSI (at the inlet in the two-dimensional computational model). The figure 5.10 and 5.11 show the axial velocity profile along the axis of symmetry and radial profile of axial velocity from the two-dimensional simulation, respectively, in comparison with the experimentally measured velocity profiles and velocity profiles from three-dimensional simulation. Though both the radial and axial profiles of axial velocity were in the same trend, the difference between the three-dimensional and two-dimensional simulations was significant. The two-dimensional simulation ended up in 5 % over prediction of axial velocity along the centre line (figure 5.10) when compared with the axial velocity obtained at the dump plane (z = 0) from the three-dimensional simulation, simulated with the identical condition and turbulence model. The axial velocity along the radial plane also showed a significant difference at r = 30 mm. The peak axial velocity was over-predicted by 20 %. The axial velocity gradient (figure 5.11) was steep compared to three-dimensional simulations.

Even though the mass flow rate of the inlet velocity profiles shown in figure 5.9 was identical to the inlet mass flow rate of the three-dimensional simulation, a significant difference in axial velocity values was seen in the two-dimensional simulations.

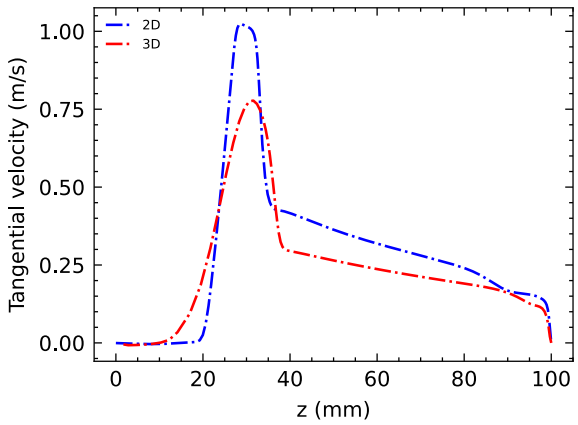

Figure 5.12: Comparison of two-dimensional and three-dimensional tangential velocity normalised with the inlet bulk velocity U_0 $(10\ m/s)$ along the radial line at 6.5 mm from the dump plane

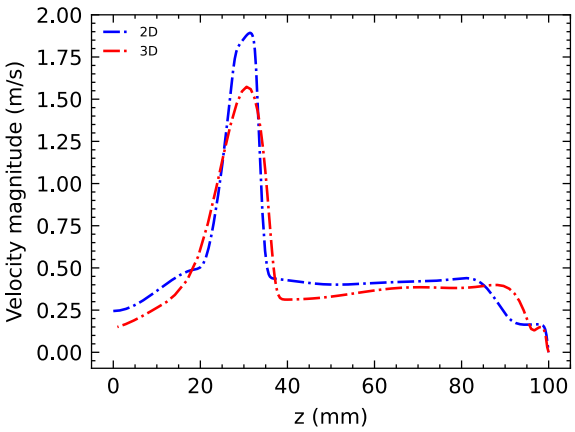

Figure 5.13: Comparison of two-dimensional and three-dimensional velocity magnitude normalised with the inlet bulk velocity U_0 $(10\ m/s)$ along the radial line at 6.5 mm from the dump plane

From figure 5.12 and figure 5.13, the over-predicted peak velocity and steep axial velocity gradient were also seen in tangential velocity profiles and velocity magnitude. The contour plot of axial velocity shown in figure 5.14 estimates the presence of a recirculation bubble at a downstream location compared to three-dimensional simulation, which is also evident from figure 5.10.

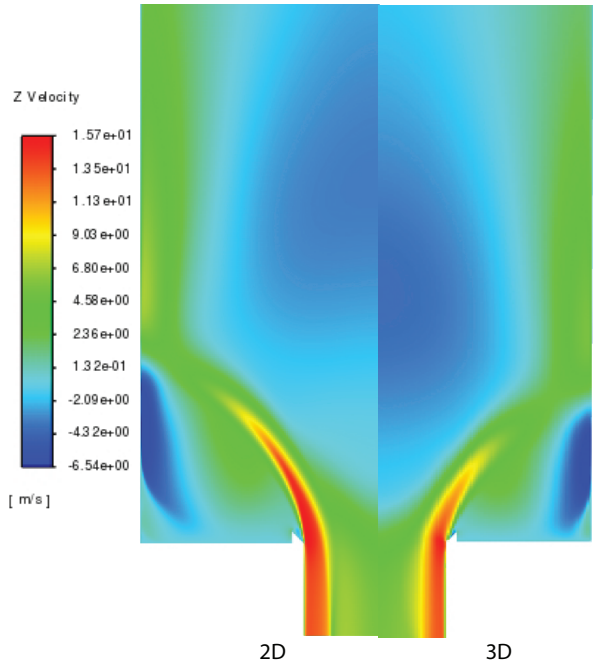

Figure 5.14: Comparison of axial velocity contours of two-dimensional (left) and three-dimensional (right) simulation

To understand the difference between the two-dimensional and three-dimensional simulations, the static pressure at the inlet of the 2D domain and 10 mm downstream of the LSI from the three-dimensional domain were analysed as shown in figure 5.15.

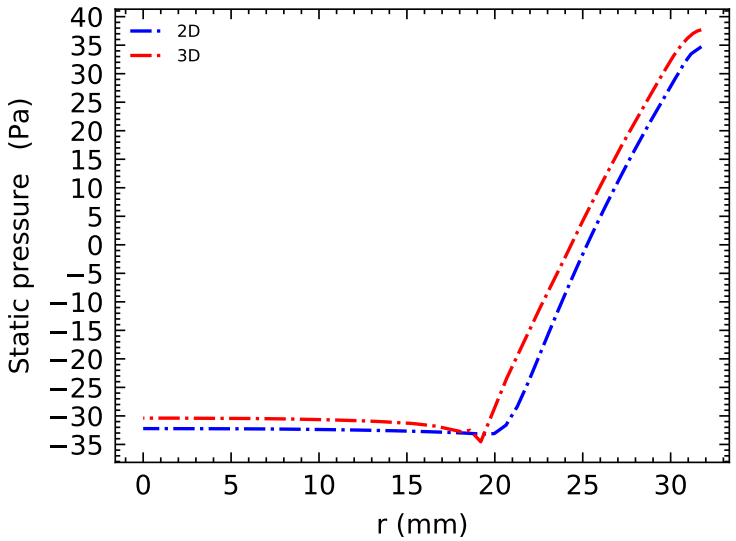

Figure 5.15: Static pressure along the radial line at the inlet for the two-dimensional model and at 10 mm downstream of LSI in the three-dimensional model.

Since the velocity inlet conditions for two-dimensional simulations were taken at 10 mm downstream of the LSI from the converged three-dimensional simulation, the static pressure at that location and the static pressure at the inlet of the two-dimensional domain must be identical. But from figure 5.15, it is seen that the static pressure profiles are not similar to each other. Three-dimensional simulation estimated pressure was more than two-dimensional estimation, which explains the over prediction of velocity in two-dimensional simulations as a result of neglecting the azimuthal direction. The velocity over prediction was attributed to the wrong estimation of velocity decay in two-dimensional since the gradient concerning azimuthal direction is neglected [5].

The over prediction of axial velocity is also evident from the axial velocity contour seen in figure 5.14. Upon comparing the position of the IRZ in two-dimensional and three-dimensional, the IRZ was found to be located a bit downstream in two-dimensional with respect to three-dimensional. This is due to the absence of stretching term in the vorticity equation (equation A.20) in two-dimensional, which results in less induced velocity production; as a result, the IRZ will be formed farther downstream than in three-dimensional. In addition to that, IRZ found in three-dimensional is not completely axisymmetric, Hence, it is intuitive that the under prediction of static pressure seen in figure 5.15 the two-dimensional simulations is due to neglecting the calculation of gradients in the azimuthal direction in continuity and momentum equations.

5.1.4. Summary of non-reacting flow results

From the analysis of non-reacting flow steady-state simulations, it is evident that the three-dimensional simulation estimation with the k-ω - SST turbulence model agreed well with the experimental measurements with 1.1 M cells. Though two-dimensional estimation failed to model the flow field accurately, the overall flow features were captured well. It is worth noting that the time required for the two-dimensional simulation was less than three-dimensional by three orders of magnitude. Therefore, two-dimensional simulations will be employed for flashback analysis.

5.2. Reacting flows

In this section reacting flow simulations were analysed and investigated. To validate the numerical procedure and modelling approach, the experimental measurements obtained from the experiments performed in the NETL SimVal (Simulation Validation) combustor was chosen [19]. Since the combustion characteristics of various lean premixed in low swirl injectors for hydrogen-enriched fuels were documented. The LSI and combustion chamber dimensions differed from non-reacting flow studies, which are briefed in chapter 4. The meshing strategy of LSI-N2 mentioned in Appendix C is adapted for reacting flow simulations since this strategy provides room for the mesh refinement in the region of interest by reducing the unstructured elements in the LSI as seen in figure C.3. The mesh refinement study with the combustion transport equation was not performed due to brevity. Instead, the mesh was refined axially in the flame stabilisation region and radially in the shear-affected area as seen in figure C.4 resulting in 2.1 million cells.

5.2.1. Validation of methane flame

Initially, the reacting flow field of premixed methane mixture with $\phi = 0.59$ was simulated in a three-dimensional domain with the Zimont flame speed model with mixture properties mentioned in table 4.1. The isolines with values C = 0.1 and C = 0.9 seen in figure 5.16 illustrate the 'M' shaped flame attached to the nozzle exit. The IRZ and ORZ were also depicted using isolines with 0 m/s velocities. A region of high-velocity gradients is seen between the recirculation zones due to shear.

The axial velocity was normalized with the bulk inflow velocity U_0 $(18\ m/s)$ along the central axis and validated with the experimental measurement of Cheng et al. [19] and with the numerical simulation of Muppala et al. [87] as shown in figure 5.17. Due to the divergence experienced by the flow at the inlet of the combustion chamber, the axial velocity along the axis shows a decreasing trend. This velocity down ramp helps the flame to stabilise at the location where the convection flow speed balances the turbulent flame speed.

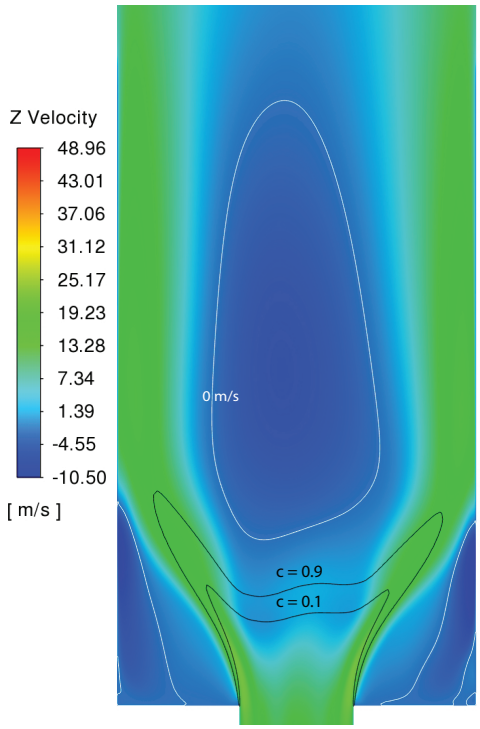

Figure 5.16: Contours of axial velocity of reacting flow field of premixed methane mixture with $\phi = 0.59$

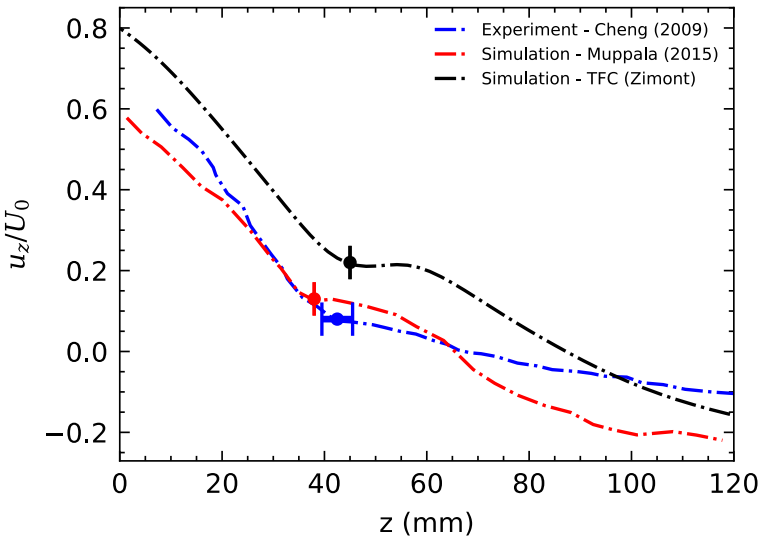

Figure 5.17: Axial velocity normalised with inlet bulk velocity U_0 ($18\ m/s$) along the centre line for methane flames with Zimont reaction model at $\phi = 0.59$. Flame front locations are marked with the respective colour bars

The velocity down ramp has a constant slope up to the flame front, and once the flow encounters the flame, the velocity profile will have a change in slope due to the density jump. Hence, it is logical to assume an arbitrary flame position based on the change in velocity gradient. Therefore, the position of the flame front was located from the axial velocity profile. In reality, the position of the flame is not fixed to a particular point, and it fluctuates around a mean point [87] therefore, a blue bar representing the range of flame location in experiments are marked as shown in figure 5.17.

The flame fronts location of Muppala et al. [87] was also marked in a similar way, but the change in gradient of the velocity was conspicuous, so a red dotted line in figure 5.17 was used for marking the assumed flame front. The position of the flame front in simulations was determined based on the same logic. The so-determined flame front position had a progress variable value of C = 0.1. Hence, marking the blue dotted lines in figure 5.17 was easy, which depicts the flame position from simulations.

The position of the flame from the experiments of Cheng et al. [19] was found between 40 to 45 mm. The flame front was identified at 38 mm by Muppala et al. [87] with the identical turbulent flame speed closure model. But the leading edge of the flame was predicted at 45 mm from the in-house simulations.

Flow behaviour and flame stabilisation discussed above were also seen in the experiments of Cheng et al. [19] and the numerical prediction of Muppala et al. [87]. But the flow acceleration in the burnt region was not explicitly captured in the experiments since the flame, in reality, is expected to flicker, which fluctuates the velocity in the burnt area. Hence, the legitimacy of the measured velocity profiles depends on the averaging size of the measured data. This explains the difference in velocity profiles between the experiments and simulations above 40 mm. When comparing the velocity profiles seen in figure 5.17, it is evident that the inhouse simulation over-predicted the velocity along the axis. The velocity over prediction was attributed to the assumptions of LSI dimensions made during the geometry generation since the detailed information about the perforation diameter, the number of perforations, the pattern of perforation and the thickness of vanes in the annular region was not known priori. All the above-discussed parameters directly affect the pressure drop across the LSI; thus, the flow split [121].

Even though the LSI geometry was optimised several times to get a target swirl number of 0.5, similar to experiments, the closest possible LSI with swirl number 0.48 was produced. Due to brevity, LSI with swirl intensity of 0.48 was chosen for all reacting flow simulations.

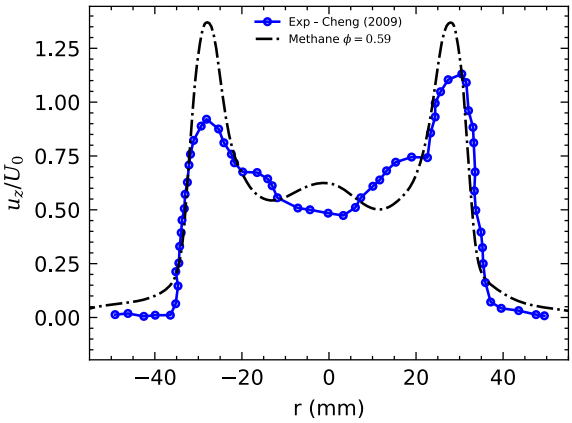

Figure 5.18: Axial velocity normalized with inlet bulk velocity U_0 (18 m/s) along the radial line at z = 15 mm for methane flames with Zimont reaction model at ϕ = 0.59

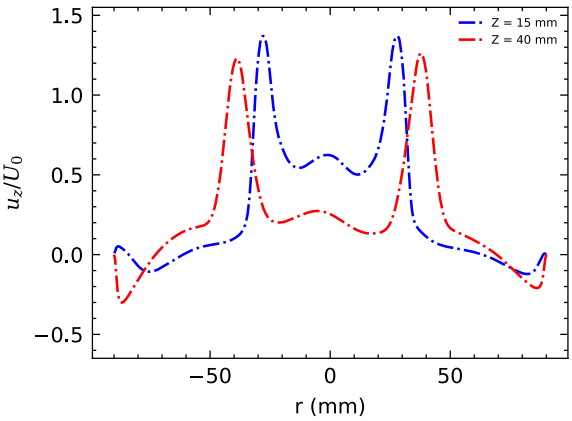

Figure 5.19: Axial velocity normalized with inlet bulk velocity U_0 (18 m/s) at z = 15 mm and z = 40 mm for methane flames with Zimont reaction model at ϕ = 0.59

In addition to the axial velocity along the axis, the radial profile of axial velocity figure 5.18 was investigated with the experimental measurements. The central channel velocity profile (-20<r<20 mm)) in figure 5.18 illustrates the presence of high axial velocity at the centre line compared to experiments, this is due to the presence of an additional jet known as pilot jet with diameter 3.2 mm in experiments. The pilot jet was embedded with the perforated plate and positioned at the centre of the premix section. The main role of the pilot jet is to ignite the fuel mixture initially and the rest of the time the jet remained shut, which acted as a central blockage. This explains the increased axial velocity at the centre and downstream flame stabilisation compared to the experiments, as seen in figure 5.17. The peak values at r = 30 and -30 mm in the figure 5.18 were over-estimated compared to the experimental measurements. However, the mean velocity over the line must be conserved since the velocity profiles of the ORZs (50 < r > -50 mm) were not reported in the experiments of Cheng et al. [19].

In the numerical simulation of Muppala et al. [87] the radial profile of axial velocity was not reported. It is highly probable that the ORZs formed near the walls might have been located at z = 15 mm from the dump plane in experiments resulting in low peak velocity. Upon comparing the axial velocity contour of reacting figure 5.16 and non-reacting figure 5.5 flows, the core of the ORZs was located downstream in reactive flow as a result of 'M' shaped density jump. However, in experiments, 'V' shaped flame is said to be formed in hydrocarbon flames [18]. The difference between the 'V' and 'M' shaped flame is discussed in detail in the upcoming sections. In addition, experimental observation states that the ORZs are subjected to axial and radial oscillations, periodical shrinkage and periodical detachments [50]. The figure 5.19 shows the radial profile of the axial velocity at Z = 15 and Z = 40 mm; the downstream location of the ORZs is evident from the maximum negative velocity at z = 40 mm. This explains the low peak axial velocity at z = 15 mm along the radial direction in experiments.

5.2.2. Hydrogen enriched flames

In this section, the effect of adding hydrogen to the fuel mixtures is studied using the TFSC model (Zimont turbulent flame speed closure), where the impact of preferential diffusion is neglected. Hydrogen was added to the methane fuel mixture in increasing percentages keeping the inflow bulk velocity U_0 (18 m/s) and equivalence ratio ϕ (0.4) as constant to investigate the effects of increased reactivity of 40 vol.%, 60 vol.%, 80 vol.%, and 100 vol.% of hydrogen-enriched fuel mixtures in experiments. Similarly, for simulating the hydrogen-enriched fuel mixtures mentioned in table 5.2, the combustion properties mentioned in table 5.2 were used for the corresponding hydrogen-enriched fuels. The combustion transport equation was not initialised each and every time for different fuel mixtures; instead, the previous reacting flow field solution was used as an initial condition, thus ramping the hydrogen concentration sequentially.

	phi (ϕ)	H_2 $vol\%$	ρ_u (kg/m^3)	AFT (K)	Le_{eff}	S_L^0 (m/s)
Flame 1	0.59	0	1.13	1610	0.96	0.104
Flame 2	0.4	40	1.11	1416	0.498	0.069
Flame 3	0.4	60	1.1	1495	0.402	0.116
Flame 4	0.4	80	1.06	1557	0.336	0.193
Flame 5	0.4	100	1	1614	0.29	0.302

Table 5.2: Combustion parameters for reactive flow simulations from [19]

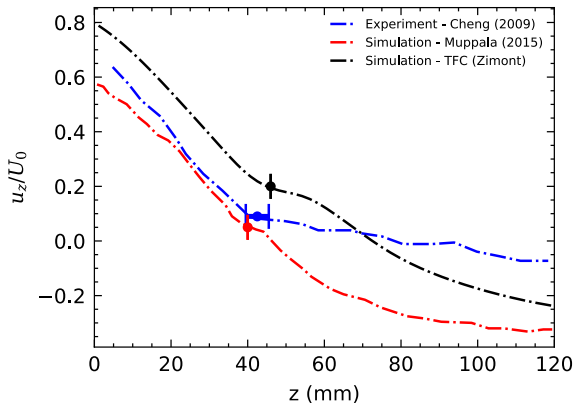

Figure 5.20: Axial velocity normalized with inlet bulk velocity U_0 (18 m/s) along the centre line of 40 vol.% hydrogen-enriched flame with Zimont reaction model at $\phi = 0.4$. Flame front locations are marked with the respective colour bars

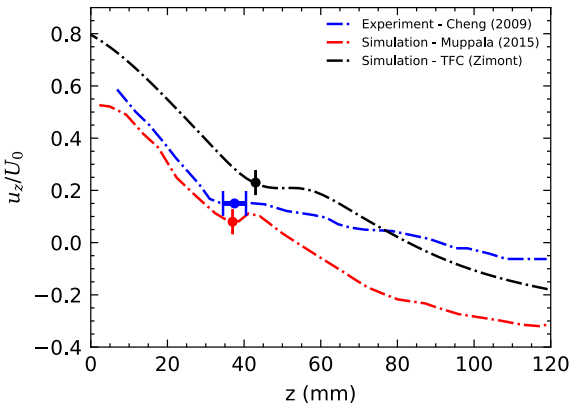

Figure 5.21: Axial velocity normalized with inlet bulk velocity U_0 (18 m/s) along the centre line of 60 vol.% hydrogen-enriched flame with Zimont reaction model at $\phi = 0.4$. Flame front locations are marked with the respective colour bars

The axial velocity profile of 40 vol.%, 60 vol.%, 80 vol.%, and 100 vol.% hydrogen-enriched fuel mixtures along the central axis is shown in figure 5.20, 5.21 5.22 and 5.23 respectively. Compared to the numerical simulations, the overestimation of the diverging velocity profile and the flame position can be attributed to the geometrical assumptions as discussed in subsection 5.2.1. Though the diverging velocity profile slope was identical to the experimental measurements, the flame anchoring position moves upstream insignificantly as the hydrogen concentration increased. However, the positive velocity gradient in the burnt region shows an increased gradient in the numerical simulations as the hydrogen concentration was increased due to an increase in reactivity.

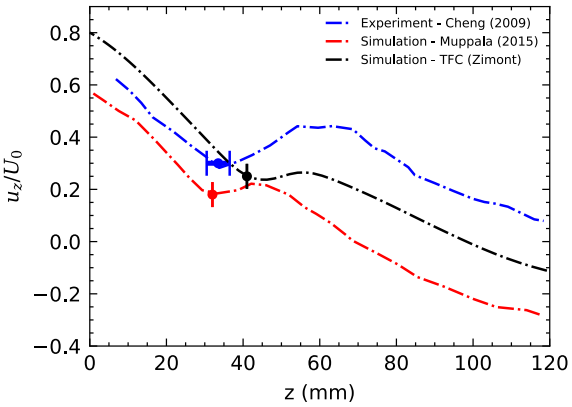

Figure 5.22: Axial velocity normalized with inlet bulk velocity U_0 (18 m/s) along the centre line of 80 vol.% hydrogen-enriched flame with Zimont reaction model at $\phi = 0.4$. Flame front locations are marked with the respective colour bars

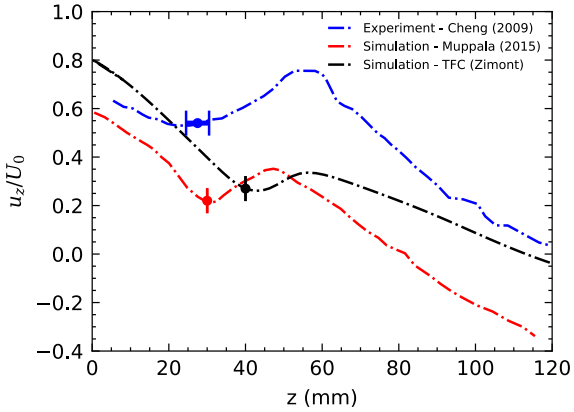

Figure 5.23: Axial velocity normalized with inlet bulk velocity U_0 (18 m/s) along the centre line of 100 vol.% hydrogen-enriched flame with Zimont reaction model at $\phi = 0.4$. Flame front locations are marked with the respective colour bars

Since the inflow velocity and the ϕ was set as a constant for all the flames in table 5.2, the turbulence intensity (u') of all the flames irrespective of hydrogen concentration remained identical as shown in figure 5.24. The increase in density jump (ρ_u/ρ_b) increases the flow acceleration downstream the flame front, which in turn increases the u'. The u' is the the most contributing parameter in the Zimont turbulent flame speed model, does not play any vital role in hydrogen addition since ϕ and U_0 are constant. Instead, the second most contributing variable S_L^0 is responsible for increased reactivity as the hydrogen percentage was increased as shown in figure 5.25. It is evident that the increase in S_L^0 significantly increases the velocity gradient in the burnt region due to an increase in reactivity. As a result, the IRZ seen in the figure 5.26 moved downstream due to the addition of hydrogen to the fuel mixture. In addition to that, the strength of the IRZ decreased. But, the location and strength of the ORZs remained unchanged.

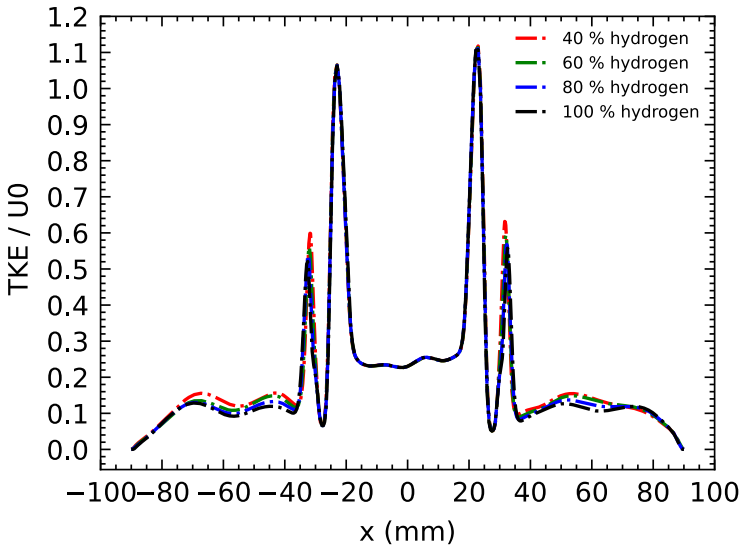

Figure 5.24: Turbulent Kinetic Energy (TKE) normalized with inlet bulk velocity U_0 (18 m/s) along the radial line at z = 15 mm of hydrogen-enriched flames with Zimont reaction model at $\phi = 0.4$

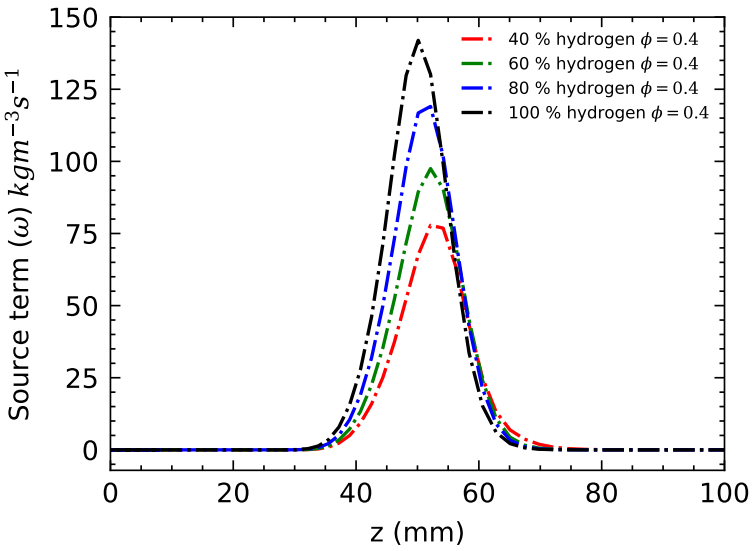

Figure 5.25: Reaction rate or source term (ω) of hydrogen-enriched fuel mixtures along the central axis of Zimont reaction model

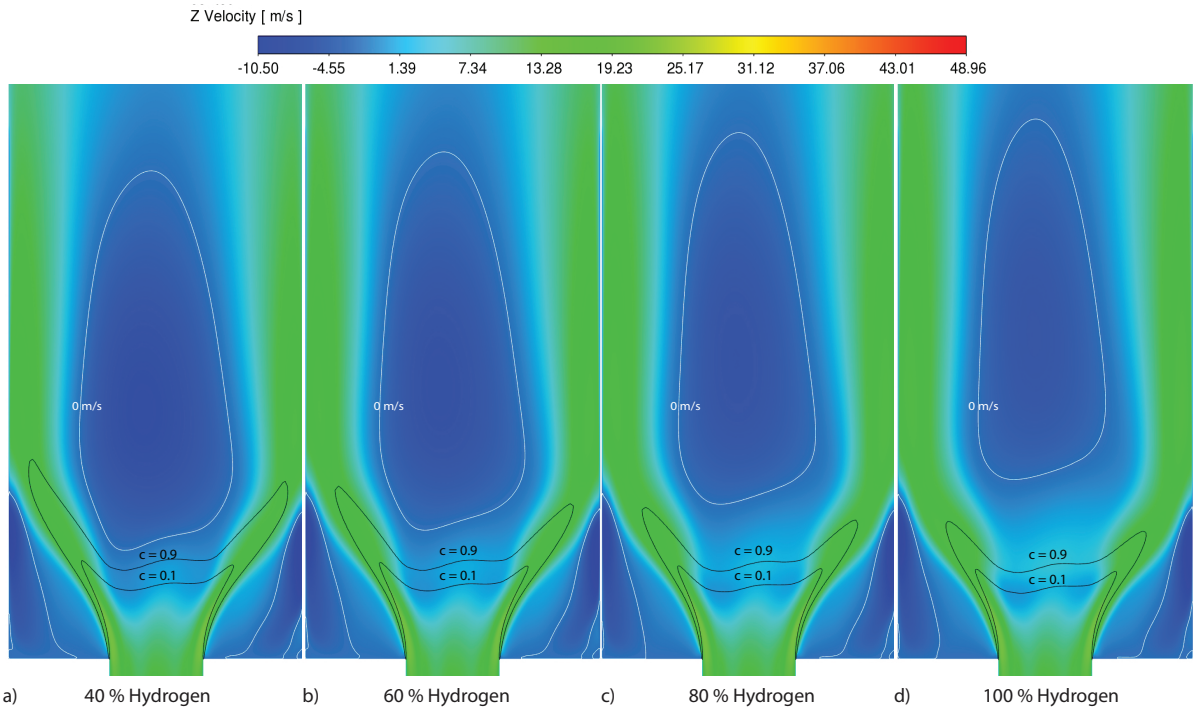

Figure 5.26: Axial velocity contours of hydrogen-enriched fuel mixtures

The peak values shown in the figure 5.24 reveal the presence of shear layers. figure 5.27 and 5.28 depicts the iso-surface of TKE with value $1.1/U_0$ (peak value from figure 5.24) m^2/s^2 and iso-surfaces of progress variable with value C = 0.9 & C = 0.1. It is evident that the flame is stabilized between ISL and OSL.

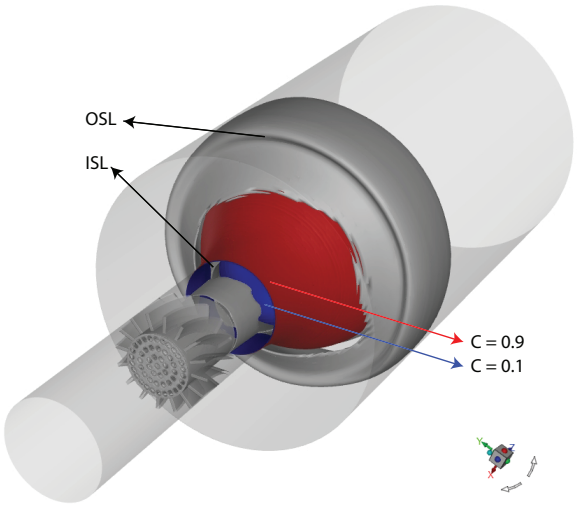

Figure 5.27: Three-dimensional view of the iso-surfaces of ISL, OSL and flame front of 100 vol.% hydrogen mixture from the bottom

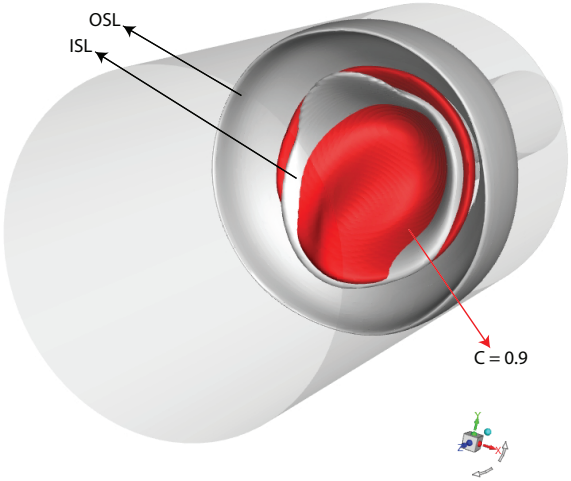

Figure 5.28: Three-dimensional view of the iso-surfaces of ISL, OSL and flame front of 100 % hydrogen mixture from the top

	$phi(\phi)$	H_2 $vol\%$	$Flame\ position\ in\ mm\ (Experiments\ Cheng\ et\ al.)$ [19]	$Flame\ position\ in\ mm\ (Simulation\ Muppala\ et\ al.)$ [87]	$Flame\ position\ in\ mm\ (Simulation\ in-house)$
Flame 1	0.59	0	40-45	38	45
Flame 2	0.4	40	40-45	40	46
Flame 3	0.4	60	35-40	37	43
Flame 4	0.4	80	31-36	32	41
Flame 5	0.4	100	25-30	30	40

Table 5.3: Comparison of flame position with experiments of Cheng et al. [19] and Numerical simulations of Muppala et al. [87]

The flame positions of the fuel mixtures are compared with experiments of Cheng et al. [19] and simulation of Muppala et al. [89] in table 5.3. From the table 5.3, it is evident that the flame position shift was marginal as the hydrogen volume percentage was increased due to a large velocity gradient before the flame. The flame front of 100 vol.% methane fuel mixture with $\phi = 0.59$ was upstream compared to 40 vol.% hydrogen fuel mixture with $\phi = 0.4$, since S_L^0 is low for a fuel mixture containing 40 vol.% hydrogen. When the flame positions were compared with the experiments, the location of the flames was in close agreement with the experiments up to 60 vol.% H_2 but the difference was significant for flame 4 and flame 5. When the flame front locations are compared with the numerical simulation of Muppala et al. [89] with the same combustion model, quite a difference was noticed for all the flames shown in table 5.3. The difference in flame front location is owed to the geometrical differences. But, the decrease in the axial location of the flame front was also marginal in the numerical simulation of Muppala et al. [89] as the vol.% of hydrogen was increased.

As the vol.% of hydrogen is increased, the position of the flame front and the positive velocity gradient generated by the flame was not well captured in the numerical simulations, which is also seen in the numerical simulations of Muppala et al. [89] and Pitsch [98]. Pitsch [98] attributed this difference to the unity Lewis number models employed in the numerical simulations. Therefore, in the next section, the effect of the addition of the Lewis number to the empirical turbulent model is examined.

5.2.3. Prediction of reactive flow with AFSW - Dinkelacker model

The reaction modelling results discussed in subsection 5.2.2 deal with the unity Lewis number assumption, and the effect of hydrogen addition in the reaction rate was incorporated through S_L^0 (for constant ϕ) in the TFC - Zimont model [133]. Therefore, to study the increase in reaction rate due to preferential diffusion effects in hydrogen-enriched flames, the AFSW reaction rate modelling discussed in subsection 3.4.5 is employed. The axial velocity profiles and reaction rates of the AFSW - Dinkelacker model [29] were investigated with the TFC - Zimont model.

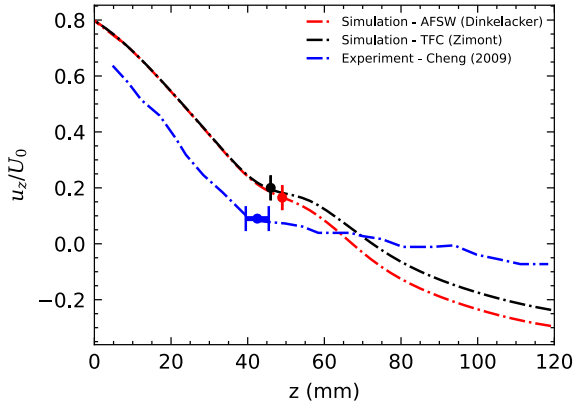

Figure 5.29: Axial velocity normalized with inlet bulk velocity U_0 (18 m/s) along the centre line of 40 vol.% hydrogen-enriched flame with Dinkelacker reaction model at $\phi = 0.4$, Flame front locations are marked with the respective colour bars

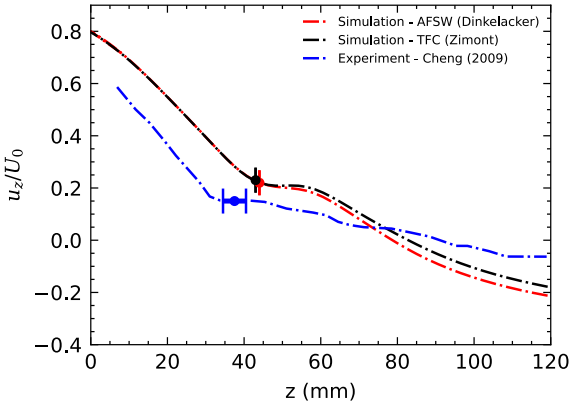

Figure 5.30: Axial velocity normalized with inlet bulk velocity U_0 (18 m/s) along the centre line of 60 vol.% hydrogen-enriched flame with Dinkelacker reaction model at $\phi = 0.4$, Flame front locations are marked with the respective colour bars

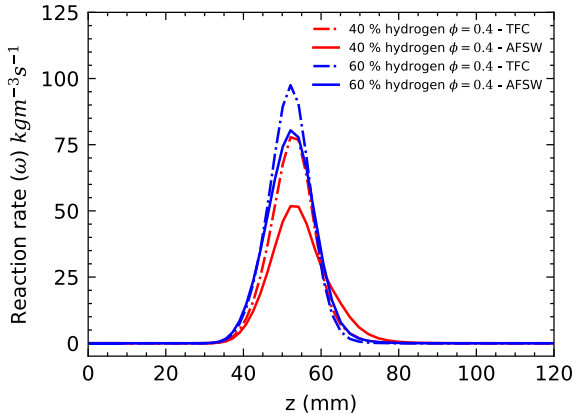

Figure 5.31: Axial velocity normalized with inlet bulk velocity U_0 (18 m/s) along the centre line of 80 vol.% hydrogen-enriched flame with Dinkelacker reaction model at $\phi = 0.4$.

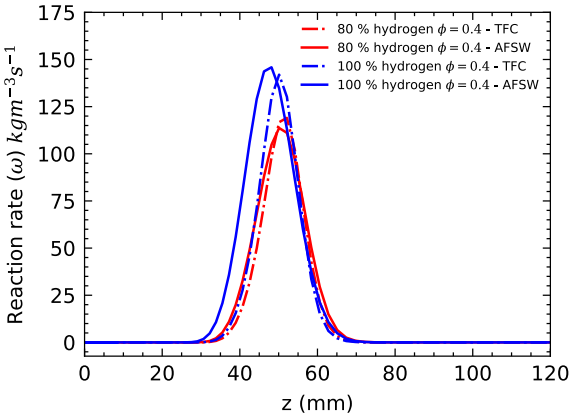

Figure 5.32: Axial velocity normalized with inlet bulk velocity U_0 (18 m/s) along the centre line of 100 vol.% hydrogen-enriched flame with Dinkelacker reaction model at $\phi = 0.4$.

Upon comparing the axial velocity profiles obtained form the Zimont and Dinkelacker models for 40 and 60 vol.% of hydrogen mixture as shown in figure 5.29 and 5.30, it is evident that the Zimont model produced greater flow acceleration behind the flame than Dinkelacker model. This is due to the reduced reaction rate predicted in Dinkelacker model than Zimont model (compared in figure 5.31) as a result of including the effective Lewis number in the turbulent flame speed closure. As a result the position of the flame front was seen a bit downstream in Dinkelacker model. However, it is difficult to interpret the location of the flame front from figure 5.29 and 5.30 since the decrease in S_T in Dinkelacker model reflects a small percentage in the sharp diverging velocity field.

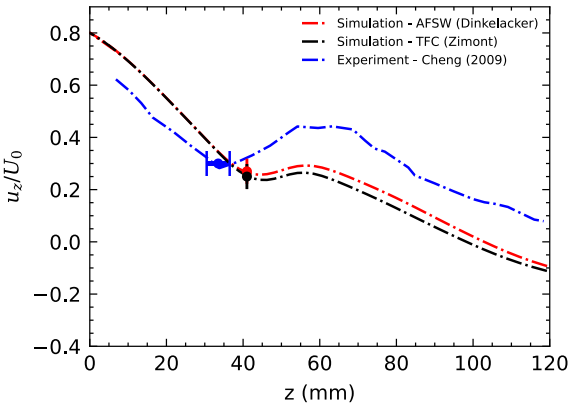

Figure 5.33: Axial profile of normalised axial velocity along the middle axis of 80 vol.% of hydrogen flame with AFSW reaction model at $\phi = 0.4$. Flame front locations are marked with the respective colour bars

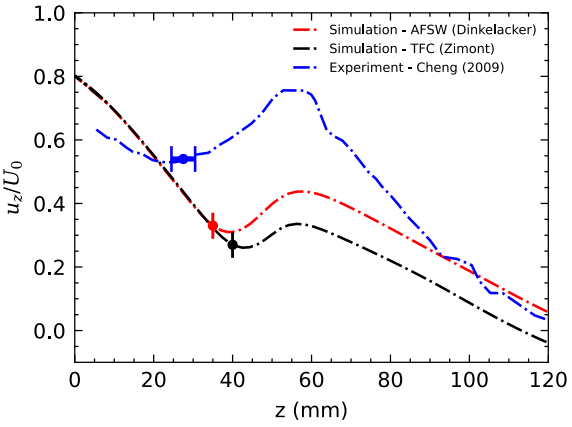

Figure 5.34: Axial profile of normalised axial velocity along the middle axis of 100 vol.% hydrogen flame with AFSW reaction model at $\phi = 0.4$. Flame front locations are marked with the respective colour bars

In the case of 80 vol.% of hydrogen mixture, the Dinkelacker model reaction rate and flow acceleration (figure 5.34 and 5.32) were approximately identical to the Zimont model. But in 100 vol.% of hydrogen mixture, the reaction rate distribution in the Dinkelacker model began more upstream than Zimont model. The reaction rate predicted by the Dinkelacker model was greater than the Zimont model, which resulted in an increased velocity gradient in the burnt region.

	$phi(\phi)$	H_2 $vol\%$	$Flame\ position\ in\ mm\ (Experiments\ Cheng\ et\ al.)$ [19]	$Flame\ position\ in\ mm\ Zimont\ Model$	$Flame\ position\ in\ mm\ Dinkelacker\ Model$
Flame 2	0.4	40	40-45	46	49
Flame 3	0.4	60	35-40	43	44
Flame 4	0.4	80	31-36	41	41
Flame 5	0.4	100	25-30	40	35

Table 5.4: Comparison of flame position with experiments of Cheng et al. [19] and numerical simulations with TFC - Zimont model & AFSW - Dinkelacker model

The flame front positions of both the combustion models were compared in table 5.4. The flame front positions for all the flames except flame 5 was similar and had a small effect on Le_{eff} addition. But, for flame 5, the flame front found in Dinkelacker model was upstream than Zimont model due to the increase in overall reaction rate seen in Dinkelacker model.

5.2.4. Summary of reacting flow results

The axial velocity profile and the reaction rate comparison with the experiments along the centre line discussed above shows that the simulation performed qualitatively good apart from the geometrical uncertainties. Though, the flow acceleration in 100 vol.% of hydrogen mixture after the flame seen in the experiments of Cheng et al. [19] (figure 5.23) was under-predicted by both Dinkelacker and Zimont model. This may be due to the S_L^0 calculated using the detailed chemical mechanism will be smaller than the experimentally measured S_L^0 in leaner regimes (ϕ = 0.4) [98].

The Dinkelacker model performed superior than Zimont model in 100 vol.% of hydrogen mixture upon implementing Le_{eff} in the reaction rate. For rest of the flame in table 5.4 the Dinkelacker model has a very small effect on the overall reaction rate. The increased reaction rate seen in Dinkelacker model can be achieved in Zimont model by artificially increasing the S_L^0 for a constant density jump. Therefore, Zimont model will be employed for the rest of the study.

6

Unraveling the Flashback Mechanism in LSB

This chapter discusses the potential reasons for the occurrence of flashback in LSB. This chapter evaluates and discusses the conditions leading to flashback based on multiple hypotheses. These hypotheses were formulated from the observations obtained from the literature and also from the numerical results discussed in the previous chapters.

6.1. Analysis of flashback in LSB

The table 6.1 shows the conditions at which flashback occurred in the experiments of [19]. The exact limit of flashback occurrence may vary in reality owing to the RANS turbulence and reaction model simulations and the adiabatic assumption. However, the mechanism or conditions responsible for a flashback in experiments should reflect in RANS simulations if the simulations are performed with correct parameters. The conditions at which flashback is said to take place in the experiments were at high vol.% of hydrogen. In addition, the inlet temperature and pressure of the fuel mixtures were also high [19]. Since the simulations of fuel mixtures at elevated inlet conditions (high T_0 and high P_0) are not within the scope of this thesis. Alternatively, the increased reaction rate required for the flashback occurrence will be provided by increasing the S_L^0 in the Zimont flame speed model for a constant $\phi = 0.4$.

Case	$H_2(vol.\%)$	$P_0(MPa)$	$T_0(\ K)$	$U_0(m/s)$	ϕ_{FB}	$S_L^0(cm/s)$
1	100	0.202	530	20	0.5	155.32
2	100	0.202	550	30	0.57	255.22
3	87	0.405	560	20	0.52	68.39
4	100	0.405	570	30	0.4	55.03
5	82	0.810	575	20	0.49	28.33
6	92	0.810	575	20	0.42	20.86

Table 6.1: Inlet conditions at flashback adapted from Cheng et al. [19]

6.1.1. Experimental observation of flashback in LSB

From the experimental observation of the occurrence of flashback in LSB by Beerer et al. [7], the flashback in the LSB took place all of a sudden, i.e. it took place in a short span of time (see figure 3.23). Upon increasing the hydrogen vol.% in the fuel mixture for the constant U_0 and ϕ, the change in flame shape from 'V' shaped flame to 'M' shaped flame was encountered at 80 vol.% of hydrogen in the experimental studies of Cheng et al. [19]. The change in flame shape was attributed to the high diffusivity of hydrogen by Cheng et al. [19]. But, the experimental studies of Kim et al. [60] state that even methane produced 'M' shaped flame at high ϕ. So, the higher burning velocity is responsible for the 'M' shape flame in hydrogen-enriched fuels. The figure 6.1 shows the comparison of the flame shapes from numerical calculations with Zimont correlation and from experiments of Cheng et al. [19].

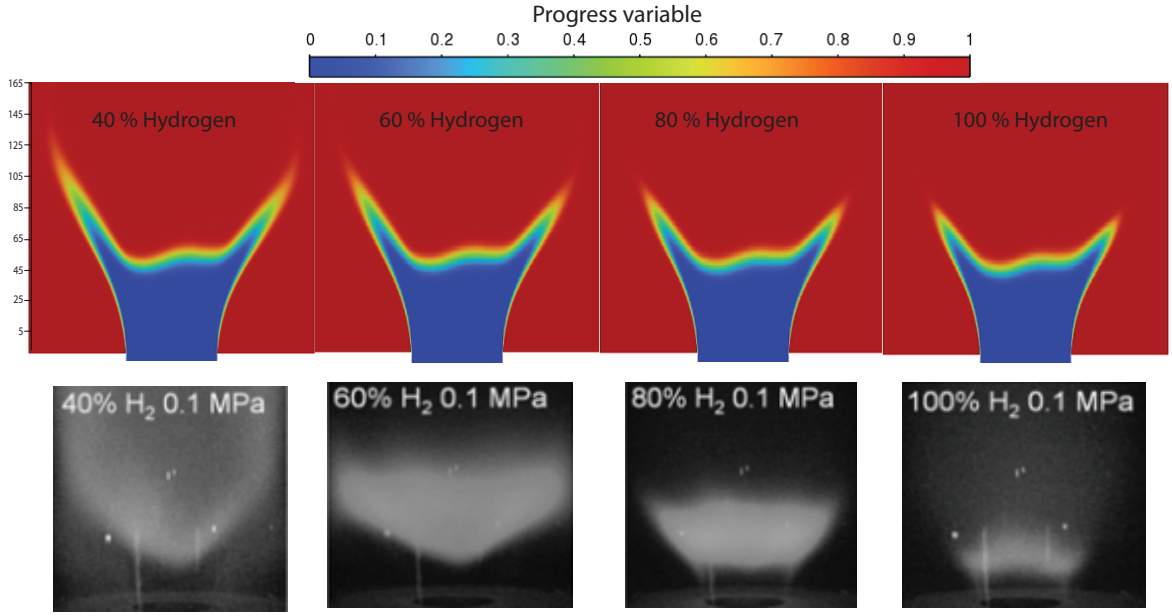

Figure 6.1: Progress variable contours of hydrogen enriched flame from numerical simulation with Zimont model (top) and photographs of flame luminosity of various CH_4/H_2 flames at $\phi = 0.4$, P= 0.1 MPa, adapted from Ref.[19] (bottom)

The flame shapes from the numerical calculation seen in figure 6.1 show the presence of 'M' shaped flame irrespective of hydrogen vol.%. Therefore, the 'V' shaped flame seen in the 40 and 60 vol.% of the hydrogen-enriched mixture was not replicated in the numerical simulations with the flamelet combustion model (Zimont and Dinkelacker). This limitation is due to the radial quenching and local strain extinction seen in the experiments, which is not taken into account in simulations. The same kind of limitation was also seen in the numerical simulations performed by Pitsch [98] and Muppala et al. [89]. Therefore, a numerical experiment will be performed by creating an artificial density jump with UDfs to study the effect of different flame shapes on flame flashback. Apart from that, the flame moved close to the nozzle exit rim significantly in experiments but not in numerical simulations, which is evident from the figure 6.1. However, in the flame obtained from the numerical simulation, it is evident that the flame size decreased as the hydrogen vol.% was increased in the fuel mixture, especially for the flame burning in the shear layers.

6.1.2. Numerical observation of flashback in LSB

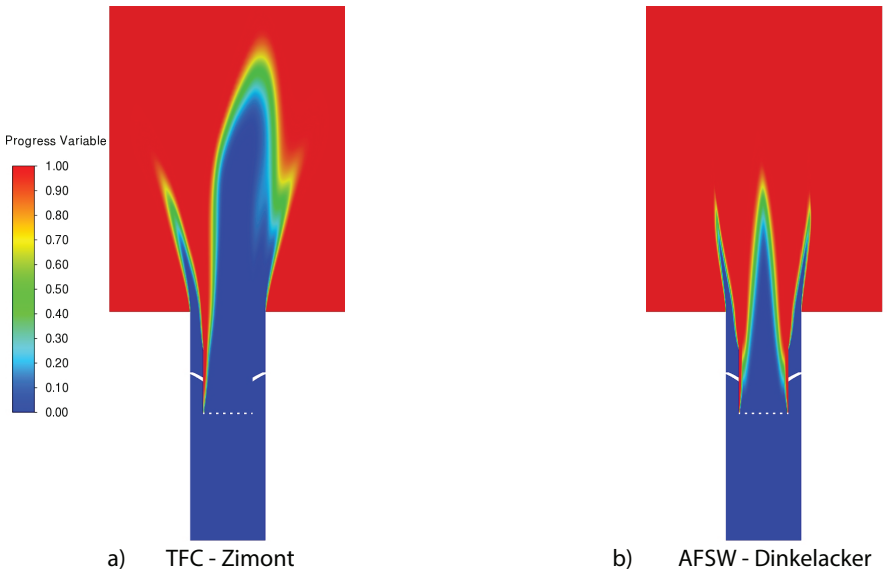

Figure 6.2: The progress variable contour of Zimont model (a) and Dinkelacker (b) for the steady-state simulations of flame 5 upon flashback.

The progress variable contour seen in figure 6.2 shows the flashback encountered during steady-state simulations for 100 vol.% of hydrogen mixture (Flame 5 in table 5.2) when the simulation was initialised from the completely burnt flow field for both Zimont and Dinkelacker model. From figure 6.2, it is evident that the flame was attached to the perforated plate. The flame seen in the figure 6.2 is just a flame holding behaviour seen only in the calculation, where it starts to burn from the wakes of the perforated plate. However, Beerer et al. [7] observed that the flame was attached to the perforated plate upon flashback. But, in the numerical simulation Muppala et al. [89] the phenomena of flashback was not investigated and in the numerical study by Pitsch [98] the flashback was not reported even at conditions mentioned in table 5.2. Though Pitsch [98] performed LES and the state-of-the-art combustion model is known as the two scalar model which is the combination of the G equation and the C equation, the flashback was not encountered. This might be because of the separate simulation of the nozzle and the combustion chamber.

To investigate the occurrence of flashback in a three-dimensional simulation without the LSI. A computational domain without LSI similar to Pitsch [98] was created (see figure C.6) to check the occurrence of flashback. The inlet velocity and turbulence profiles were extracted from the three-dimensional simulation performed with the LSI. Initially, non-reacting flow simulations were performed to verify the correctness of the specified inlet boundary. The velocity and pressure profiles of the simulation were verified in Appendix C with the non-reacting three-dimensional simulation performed with the LSI. From subsection C.3.1, it is evident that the simulations with and without swirler performed identically. Reacting flow simulations with the Zimont model were performed, excluding the LSI for flame 5 in table 5.2. Surprisingly the flashback was not encountered even when the reactive flow field was initialised with a completely burnt flow field. Therefore, simulations were performed for scaled up S_L^0 starting from $0.3\ m/s$ for a constant U_0 and ϕ.

The reaction rate obtained from the reacting flow simulation with scaled up S_L^0 is seen in figure 6.3. Flashback was not encountered in any of the S_L^0 values ranging from 0.3 to $1.65\ m/s$. Hence, it is apparent that wakes behind the perforate plate are responsible for the

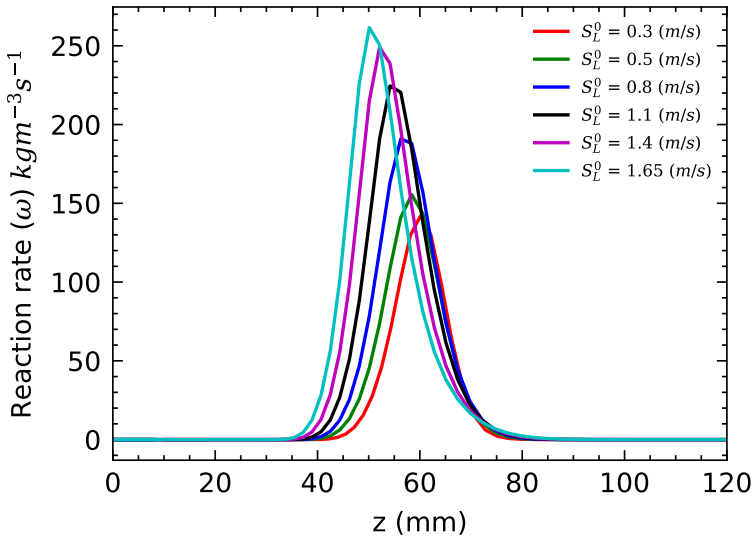

Figure 6.3: Reaction rates calculated from the Zimont model simulations for scaled up S_L^0

flame holding seen in (figure 6.2) the three-dimensional simulations with LSI modelled in the computational domain. Therefore, a three-dimensional model with the LSI will be employed for the rest of the flashback analysis.

6.2. Evaluation of standard flashback mechanisms in LSB

The mechanism and the conditions favouring the flashback process are analysed in this section based on the numerical calculation and observations performed so far.

- **Flame propagation in the core flow**: The axial velocity profile of hydrogen-enriched fuel mixtures along the central axis seen in figure 6.4 shows a strong velocity gradient due to flow divergence. So, for the flame to propagate against the core of the flow, the S_T must surpass the strong velocity gradient before the flame (z < 40mm). Hence, flame propagation in the core of the flow field is impossible.

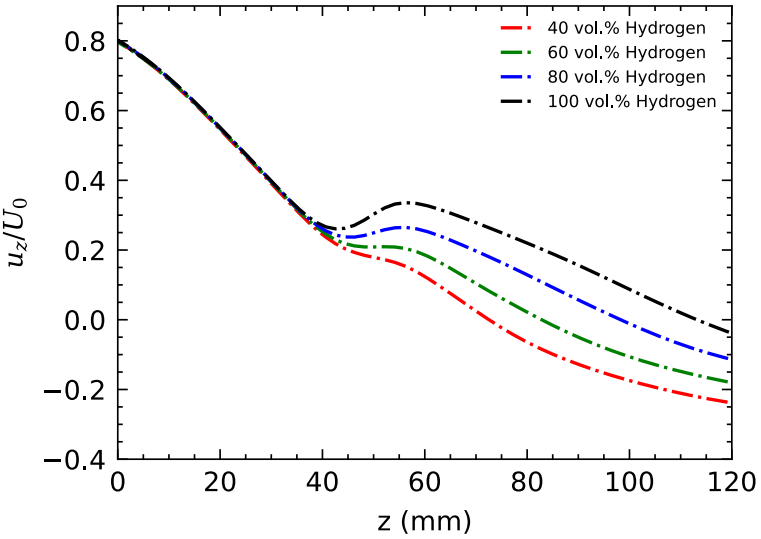

Figure 6.4: Axial profile of normalised axial velocity along the middle axis for hydrogen-enriched flames with TFC reaction model at $\phi = 0.4$

- **Flame propagation due to CIVB**: The axial velocity contours of hydrogen-enriched fuel mixtures seen in figure 5.26 illustrate the IRZ is located downstream from the flame front, and the distance between the flame front and the IRZ keeps increasing as the reaction rate of the fuel mixture increases. So, IRZ will be found far away from the flame in the experiments at the condition mentioned in the table 3.1. Therefore, the induced velocity produced as a result of the baroclinic term (see section A.3) does not pave the way for the flame to propagate upstream since the flame is not found inside the IRZ as seen in figure 3.22 (a). Hence, CIVB is also not accountable for a flame flashback in LSB.
- **Flame propagation in boundary layer**: Based on the progress variable contour seen in figure 6.2, it seems like a flashback might have initiated upstream of the centre channel through the ISL. Moreover, the stable flame is far away from the wall boundary layer. In addition, a three-dimensional simulation performed without LSI for a refined y^+ value of unity (see subsection C.3.1) illustrates the absence of boundary layer flashback. Therefore, it is evident that the flame did not propagate through the boundary layer of the outer wall. However, the wall of the centre channel in the low swirl injector might have aided the flashback process.
- **Flame propagation due to combustion instability**: To investigate the unsteady heat release and pressure fluctuations in LSB, transient simulations involving the reactions should be performed. But this is outside the scope of this thesis. However, the pressure oscillations before the flashback event were not seen in the experimental measurements of Beerer et al. [7]. Therefore it is presumed that this mechanism is also not responsible for a flashback in LSB.

The occurrence of flashback in LSB was not reported in the numerical simulations of Muppala et al. [87] and Pitsch [98]. But, flashback was reported in the experimental studies of Cheng et al. [19] and Beerer et al. [7] and the flame was attached to the perforated plate aftermath flashback in experiments, as seen in figure 6.2 [7]. The mechanism responsible for flashback was not stated explicitly in experiments studies. Hence, it is assumed that none of the above-listed standard flashback mechanisms was solely responsible for the flame flashback in LSB. Therefore, the formation of 'M' shaped flame due to high burning velocity, low-velocity streaks and wakes from the perforated plate, stretch effects, local enrichment due to preferential diffusion and other instabilities present in the ORZ might aid in the flame flashback in LSB. Hence, in the next section, multiple hypotheses stated below will be investigated and analyzed to identify the potential reason for a flame flashback in LSB. These hypotheses were formulated based on the numerical and experimental observations understood so far.

* **'M' shaped flame (attached flame) is more susceptible to flame flashback than 'V' (detached flame) shaped flame**
* **Upstream flame propagation into the nozzle influence the mass flow split between the swirler and the centre channel**
* **Reducing the axial mass flow rate of the centre channel in LSI results in flame flashback**
* **Upstream flame propagation is facilitated through the ISL**

6.2.1. Analysis of the 'M' and 'V' shaped artificial flame front

From the experimental observations of the LSB discussed in subsection 6.1.1 and subsection 3.3.3, it is understood that flame takes 'M' and 'V' shapes depending upon their flame speed. It is worth noting that flashback was never observed in the experiments when the flame was in 'V' shape [20]. But, the 'V' shaped flame front was not replicated in the reacting flow simulations due to adiabatic assumption and radial quenching neglection. Hence, artificial 'V' and 'M' shaped flame front was created by defining location dependent density jump at the dump plane without involving the combustion transport equation. A User Defined Functions (UDF) (see Appendix E) was employed in Fluent to generate and analyse the artificial flame. Therefore, the following hypothesis will be tested with the aid of UDFs to model the different flame shapes as shown in figure 6.5 at the nozzle exit with the inlet bulk velocity of U_0 = 18 m/s.

* **'M' shaped flame (attached flame) is more susceptible to flame flashback than 'V' (detached flame) shaped flame**

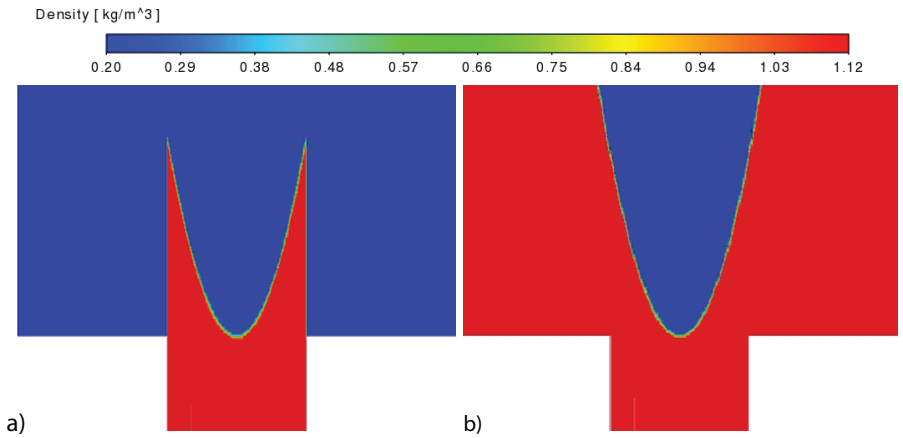

Figure 6.5: Density contours illustrating the M-shaped flame (a) and V-shaped flame (b)

The axial velocity vectors of the 'M' and 'V' shaped flames are shown in figure 6.6 (a) and (b), respectively, with the black iso-contour lines marking the flame front. It is certain that for the 'M' shaped flame, the flow acceleration downstream of the flame was higher than the 'V' shaped flame for a constant density jump figure 6.6. The downstream flow acceleration is also evident from the plot of the axial gradient of the static pressure along the centre line (figure 6.7). The lowest minimum of the static pressure gradient downstream of the density jump in the 'M' shaped flame is due to induced velocity created due to an additional density jump present at the nozzle exit.

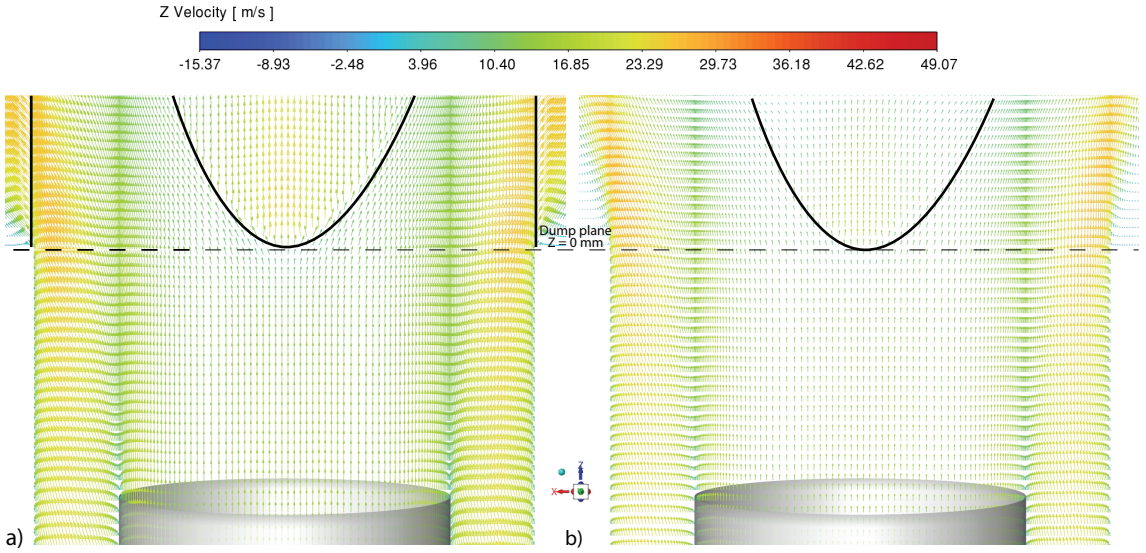

Figure 6.6: Axial velocity vectors of M-shaped flame (a) and V-shaped flame (b)

From figure 6.7, the presence of an adverse pressure gradient before the flame front was obvious. Due to an adverse pressure gradient upstream of the flame front, the flow starts to slow down, aiding the upstream flame propagation. Upon comparing the adverse pressure gradient of both the flames, the adverse pressure gradient of the 'M' shaped flame was higher than the 'V' shaped flame. Hence, the 'M' shaped flame is more susceptible to flame flashback than the 'V' shaped flame.

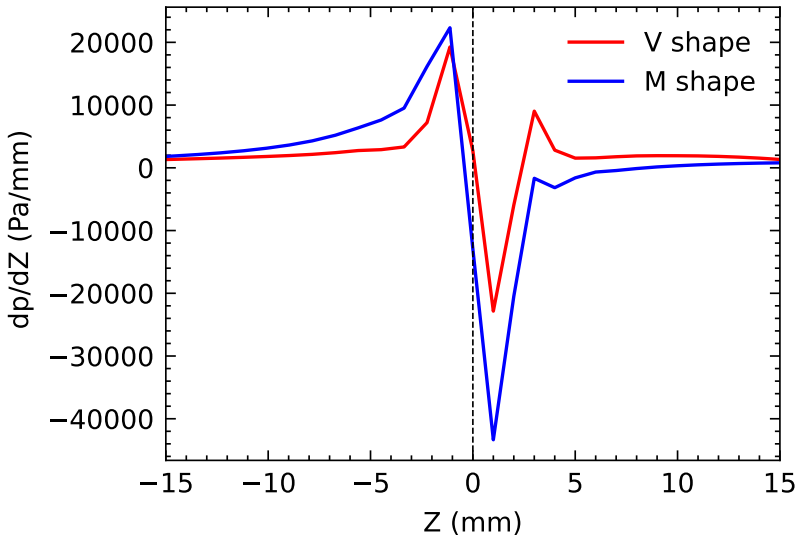

Figure 6.7: Static pressure gradient along the axis of 'M' and 'V' shaped flame

6.2.2. Evaluation of mass flow split in the nozzle

From the flame shape analysis in the previous subsection 6.2.1, it is clear that the 'M' and 'V' shaped flame located at the dump plane influence the flow upstream. The mass flow rate ($\dot{m}$ = 0.05165 kg/s where, ρ = 1.12 kg/m^3, U_0 = 18 m/s, area = 2.565 x 10^{-3} m^2) in the nozzle gets divided between the swirler and centre channel depending on the pressure drop across the LSI. Therefore the hypothesis stated below will be tested for the flame fronts positioned at various locations.

* **Upstream flame propagation into the nozzle influence the mass flow split between the swirler and the centre channel**

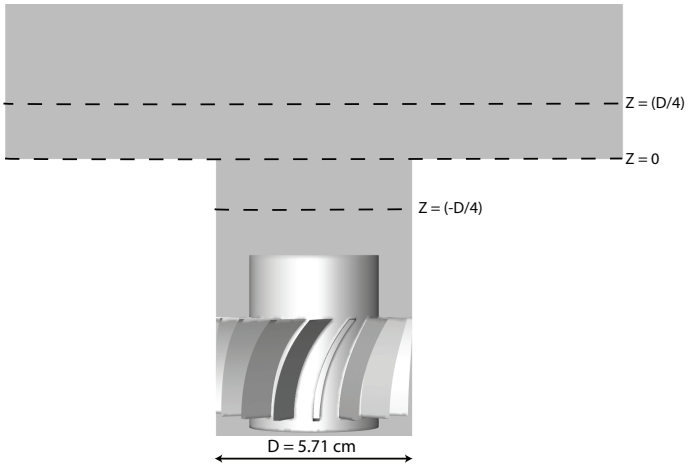

Figure 6.8: axial Location of the specified density jumps

The black dotted line in the figure 6.8 shows the locations of the 'M' and 'V' shaped flame fronts positioned to evaluate the mass flow distribution and upstream effects of the flame front. At three different locations (above the nozzle - Z = D/4, at the nozzle exit - Z = 0 and into the nozzle - Z = -D/4, where 'D' is the diameter of the nozzle (D = 5.715 x 10^{-2} m), the mass flow rate over the centre channel and the swirler were calculated for 'M' and 'V' flame fronts, and they are tabulated in table 6.2 and table 6.3.

Location	Mass flow rate through the swirler	Mass flow rate through the centre channel
Z = D/4	0.03238 (62.69 %)	0.01927 (37.31 %)
Z = 0	0.03239 (62.7 %)	0.01926 (37.30 %)
Z = -D/4	0.03244(62.81 %)	0.01921 (37.19 %)

Table 6.2: The mass flow rate split between the swirler and the centre channel in 'V' shaped flame

Upon upstream flame propagation, an insignificant mass of fluid shifts from the centre channel to the swirler irrespective of the flame shape due to the density jump which is evident from table 6.2 and table 6.3. When the flame front was above the nozzle (Z = D/4), the mass flow split between the swirler and the centre channel of both the flame shapes were identical. Therefore, the flame downstream of the nozzle exit has no influence on the mass flow split. Similarly, the mass flow split was identical between different flame shapes when the flame front was inside the nozzle. Thus, the additional density gradients seen in the 'M' shaped flame also have no influence when the flame is upstream and downstream of the nozzle.

Location	Mass flow rate through the swirler	Mass flow rate through the centre channel
Z = D/4	0.03238 (62.69 %)	0.01927 (37.31 %)
Z = 0	0.03240 (62.73 %)	0.01925 (37.27 %)
Z = -D/4	0.03244 (62.81 %)	0.01921 (37.19 %)

Table 6.3: The mass flow rate split between the swirler and the centre channel in 'M' shaped flame

Interestingly at Z = 0 (at nozzle exit), the mass flow rate in the swiler was higher in the 'M' shaped flame than 'V' shaped flame. This is because of the high adverse pressure gradient in the 'M' shaped flame shown in figure 6.7. Though the mass flow split difference was marginal, the 'M' shaped flame might propagate faster into the nozzle than the 'V' shaped flame during the occurrence of flashback.

6.2.3. Effect of the mass flow through the centre channel

Two-dimensional simulations were performed with the Zimont reaction model for flame 1 in table 4.1 to evaluate the following hypothesis.

* **Reducing the axial mass flow rate of the centre channel in LSI results in flame flashback**

Since the tangential velocity component is absent in the centre channel, as seen in figure 5.9, scaling the axial velocity component is equivalent to decreasing the mass flow rate through the centre channel. Hence, the effect of mass flow (velocity) through the centre channel is investigated by reducing the axial velocity of the centre channel. The two-dimensional simulations were performed because the axial velocity through the central axis was easily scaled down from the velocity profiles obtained from the three-dimensional simulation. The inlet velocity required for the two-dimensional simulations was specified in a similar method discussed in subsection 5.1.3. Six independent simulations were performed for six different axial velocity profiles plotted in figure 6.9 which were specified at the inlet of the two-dimensional domain shown in figure C.5.

figure 6.10 depicts the axial velocity normalized with bulk velocity ($U_0 = 18m/s$) along the central axis for six different scaled-down Uz_c. The location of the flame front is interpreted from the change in axial velocity gradient. Upon reducing Uz_c and keeping the S_L^0 as constant, the flame front above the centre channel moved upstream along with the flame front burning in shear layers as seen in figure 6.11. Therefore, it is evident that the velocity magnitude in the centre channel is the most important flow parameter for flame positioning in LSB. Reducing the axial component without changing the tangential component signifies increased swirl intensity. Therefore, an increased swirl number significantly brings the flame close to the nozzle. In addition to that, the size and strength of the IRZ increased significantly as the Uz_c was scaled down, as seen in figure 6.11.

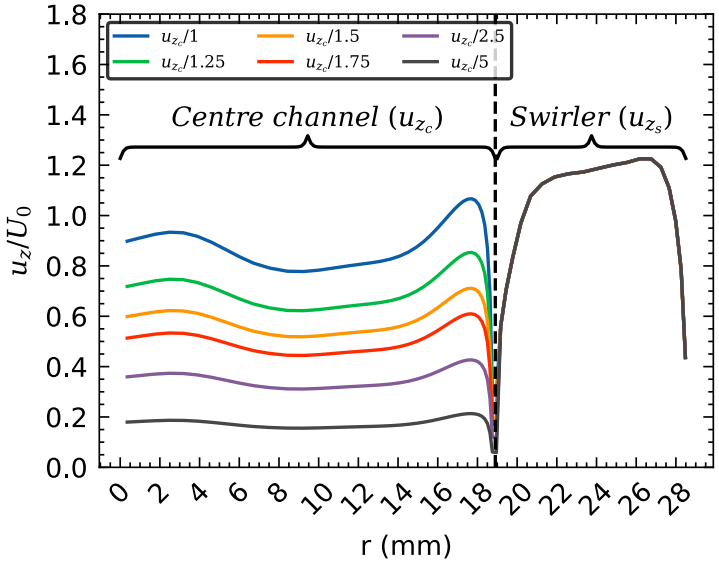

Figure 6.9: Radial profile of normalized axial velocity ($U_0 = 18m/s$) specified at the inlet for the two-dimensional simulation.

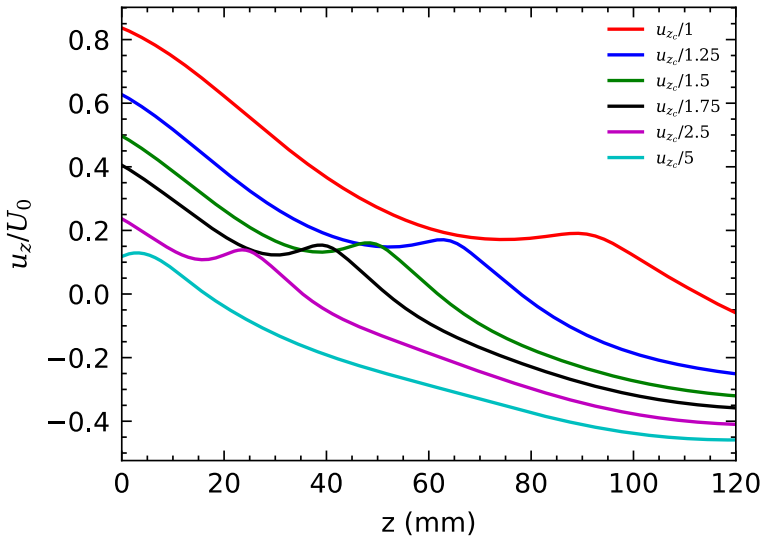

Figure 6.10: Axial velocity normalized with inlet velocity ($U_0 = 18m/s$) along the middle axis for flame 1 in table 5.2

The flashback was not observed in any scaled-down velocity profiles shown in figure 6.11. The flame was even stable when the scaled-down axial velocity profile brought the flame into the nozzle, as shown in figure 6.11 (f). This hypotheses analysis shows that flashback did not occur in the core flow and boundary layer. In addition, the IRZ was downstream of the flame. Hence, it is clear that the flame flashback in LSB was not captured in the numerical simulation performed by employing RANS and flamelet combustion models.

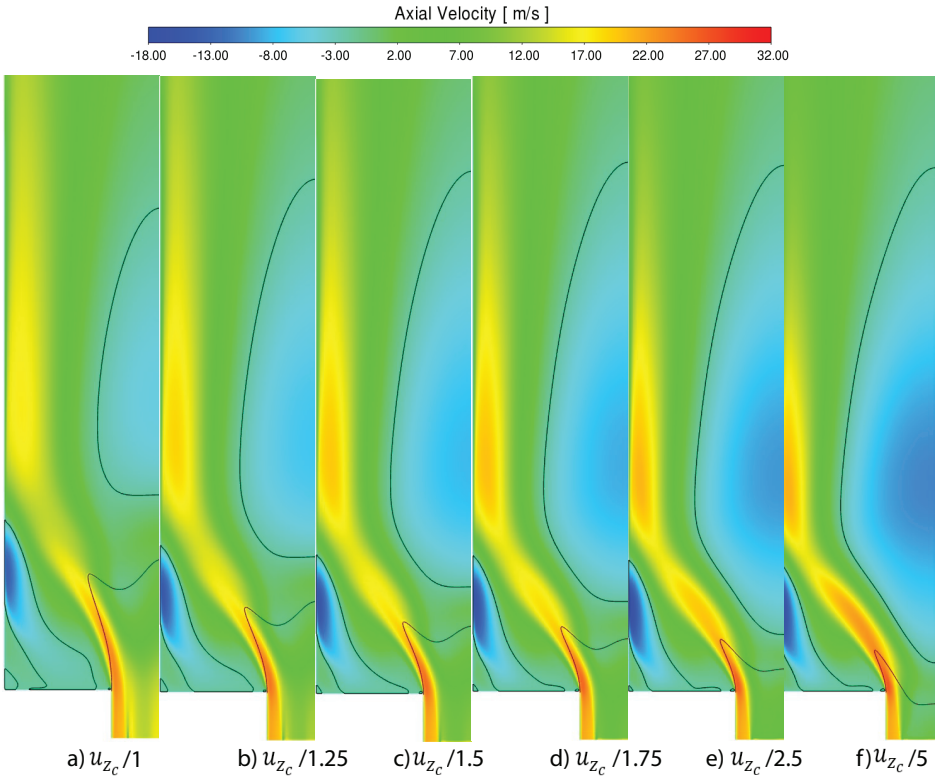

Figure 6.11: The axial velocity contours of scaled-down centre channel axial velocity (Uz_c) of flame 1.

6.2.4. Local analysis of shear layers

From the experimental observation of flashback event [7]; the flashback is said to happen suddenly in a short span of time. Hence, the following reason behind the sudden occurrence of flashback will be evaluated using the following hypothesis.

* **Upstream flame propagation is facilitated through the ISL**

From the axial velocity contour of the nozzle shown in figure 6.12, it is evident that the flow over the perforated plate produced a region of negative velocity (wake of the perforated plate) and positive velocity close to each other. However, the positive and negative velocity streaks get mixed after the LSI exit due to turbulence. But, the interaction of the wakes with the positive velocity region will exhibit a strong unsteadiness and non-uniformity [98]. Though the unsteady flow behaviour and the vortices from the perforated plate were not modelled in this thesis, the non-uniformity of the flow can be confirmed by plotting the axial velocity at the exit of the nozzle.

From figure 6.13 the presence of a non-uniform velocity profile in the centre channel is evident for all the velocity profiles. The presence of zero axial velocity at -20 and +20 mm for the LSI exit illustrates the presence of the inner wall of the centre channel. Upon comparing the radial velocity profiles from the injector exit to the nozzle exit, it is clear that the flow divergence due to the sudden expanding geometry starts to take effect inside the nozzle. Further, a small asymmetry is also noticed from the figure 6.13.

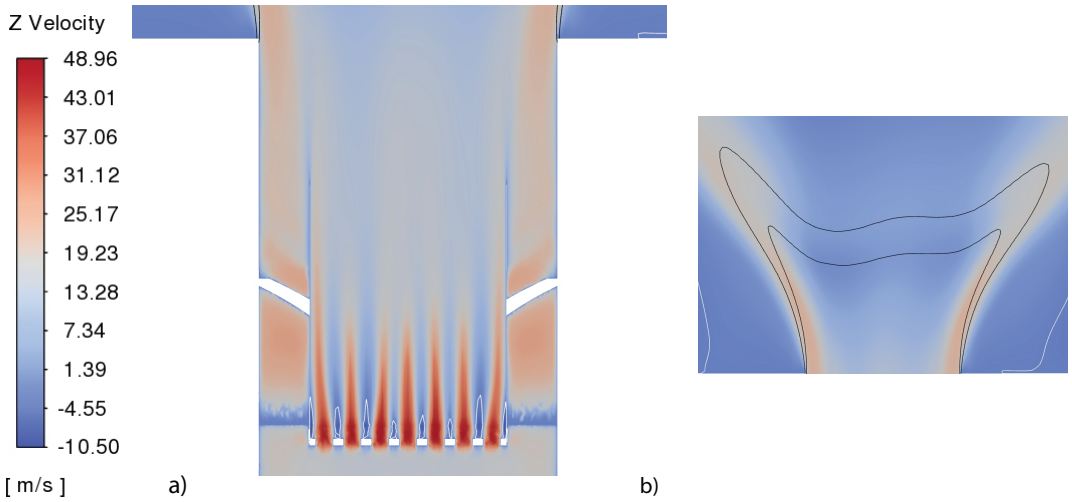

Figure 6.12: Axial velocity contour of the nozzle (a) and axial velocity contour above the nozzle with the flame front of flame 5 in table 5.2

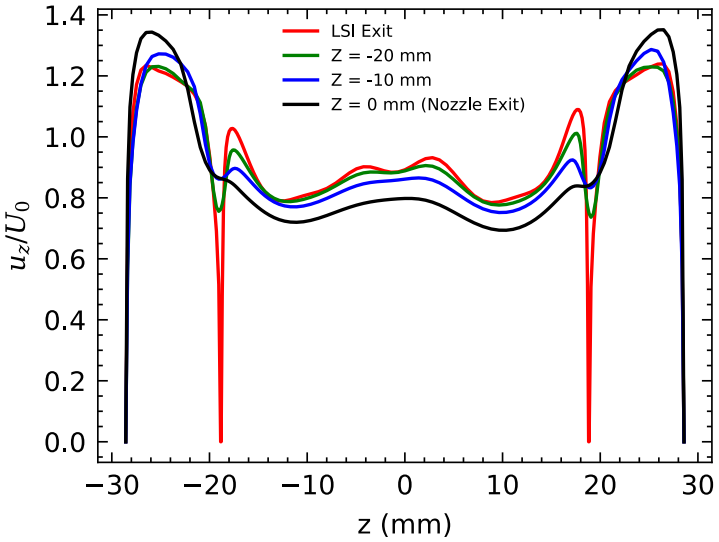

Figure 6.13: Axial velocity inside the nozzle normalized with inlet velocity ($U_0 = 18m/s$) along the radial planes for flame 5 in table 5.2

The figure 6.14 shows the iso-contours of TKE with a constant value of 20 m^2/s^2 along with the iso-contours of the progress variable (C) with values 0.1 and 0.9, illustrating the unburnt and burnt state respectively. The presence of the shear layer above the centre channel wall possesses the same TKE value as the ISL. From figure 5.27 and 5.28, it is evident that the stable flame is spotted along with the ISL and OSL with TKE equal to 20 m^2/s^2. Hence, a small upstream movement of the flame into the nozzle due to fluctuations results in flame propagation from ISL to the shear layer above the central channel wall.

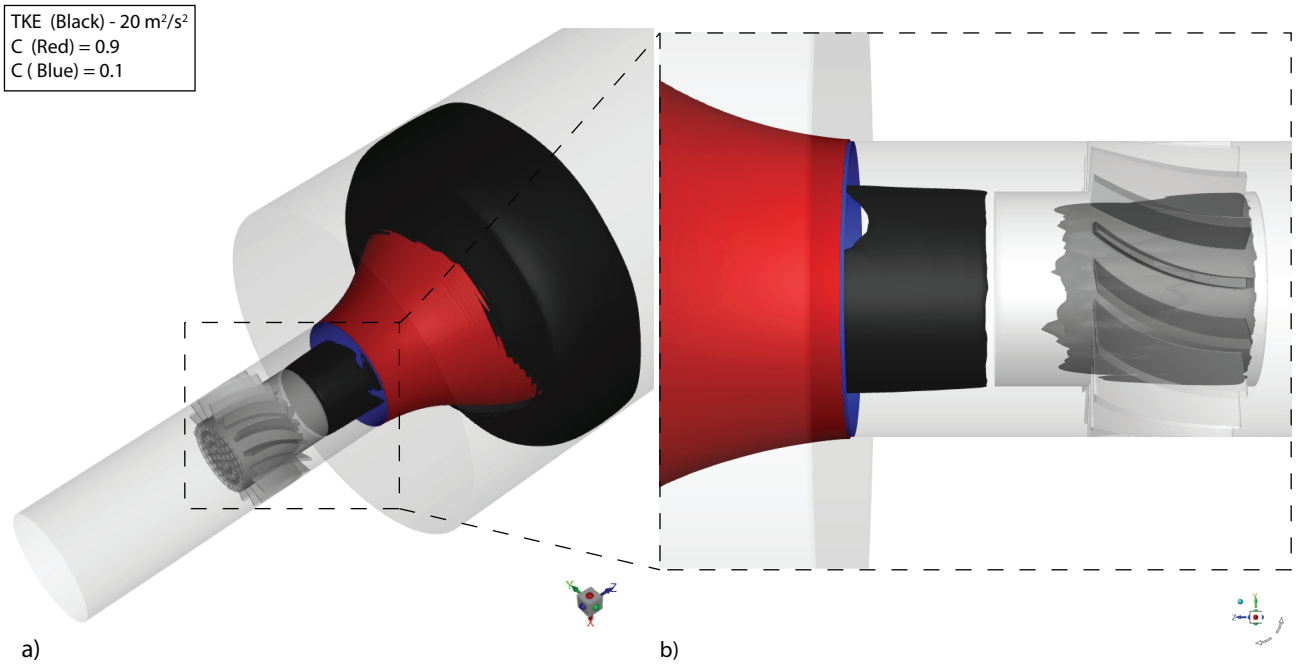

Figure 6.14: Iso-surfaces of TKE with value 20 m^2/s^2 and progress variable with value C = 0.1 and 0.9 of flame 5, overview (a) and zoomed in (b)

The flame luminosity photographs taken from the experiments of Cheng et al. [19] at condition close to flashback conditions mentioned in table 6.1 is shown in figure 6.15. The flame luminosity photograph illustrates the flame is located downstream of the nozzle exit even though the flame was close to flashback conditions. But, the flame front seen in figure 6.15 is more likely to be affected by the fluctuating ORZs, Precessing Vortex Core (PVC), flame stretch, and localised high flame speed due to thermo-diffusive instabilities discussed in subsection 2.6.2. Pitsch [98] suggested that thermo-diffusive instabilities need to be considered for capturing the flame flashback in hydrogen-enriched flames. But, even after considering the thermo-diffusive instabilities in the numerical modelling (see figure 6.16) of flame 5 in table 5.2 with S_L^0 scaled up by a factor of three, flashback was not reported by Pitsch [98].

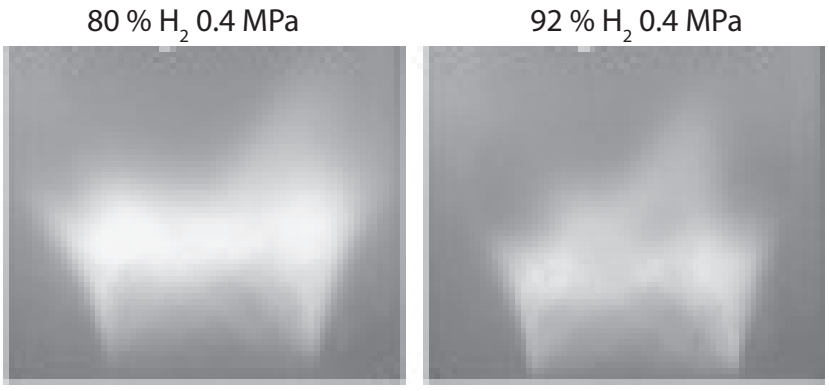

Figure 6.15: Flame luminosity photographs taken from the experiments of Cheng et al. [19] at P = 0.4 MPa, $U_0 = 40\ m/s$ and $T_0 = 500 - 600\ k$, close to flashback conditions mentioned in table 6.1

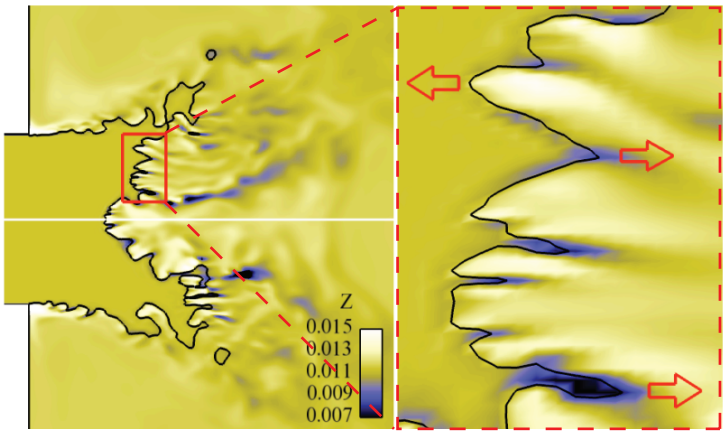

Figure 6.16: Instantaneous profile of mixture fraction capturing the thermo-diffusive instability, taken from Pitsch [98]

In addition, the flame front seen in figure 6.12 (b) is positively curved on the left and negatively curved on the right. The curvature effects seen in figure 6.12 (b) are perhaps due to the flow distribution from the centre channel, but this might lead to hydrodynamic instability (discussed in subsection 2.6.1). Furthermore, thermo-diffusive (discussed in subsection 2.6.2) instability seen in figure 6.16 for the hydrogen-enriched flame leads to amplification of upstream flame propagation. However, the reaction model employed in this thesis cannot model all the instabilities and local effects seen in reality. Therefore, considering all the instability and local effects in the numerical modelling might aid in capturing the flame flashback.

The schematic illustration seen in figure 6.17 illustrates the possible sequential steps for the occurrence of flame flashback in LSB. First, a slight flame fluctuation due to the thermo-diffusive instability (step 1) leads to the upstream flame propagation into the nozzle. In combination with the adverse pressure gradient in the 'M' shaped flame, the flame will propagate at a highly accelerating rate along the shear layer (step 2) above the centre channel wall. Then, with the help of the wall of the centre channel (step 3) and vortices in the perforated plate (step 4) flame will be stabilized at the perforated plate aftermath of the flashback.

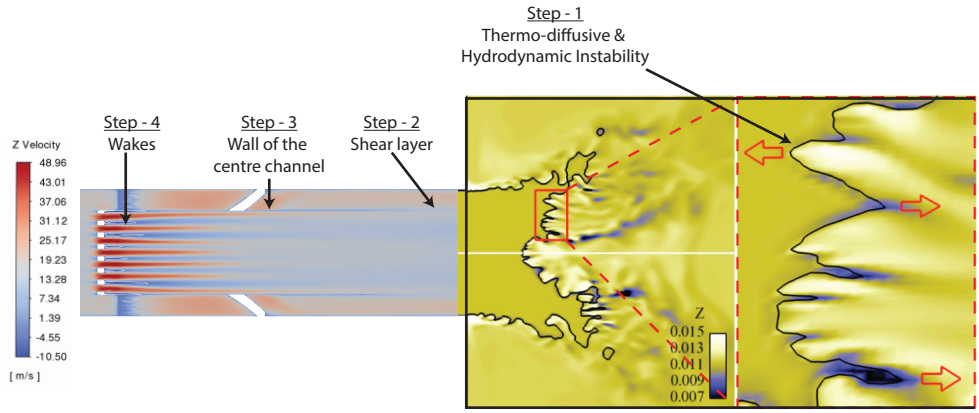

Figure 6.17: Schematic illustration of possible flashback event in LSB, adapted from Pitsch [98]

7

Conclusions and Recommendations

In this thesis, RANS simulations were performed for the LSB with the flamelet combustion model. First, a three-dimensional non-reacting flow simulations of the turbulent swirling flow were modelled using Standard k-ϵ, Re-Normalisation Group k-ϵ, Realizable k-ϵ and SST-k-ω turbulence models. Among the above-listed two-equation turbulence models, the best suitable turbulence model, which agrees well with the experiment results of Cheng and Littlejohn [20] was chosen to simulate the reactive flows. The numerical results from the three-dimensional reactive flow simulations were validated with the experimental results of Cheng et al. [19] and numerical simulations of Muppala et al. [87]. The reactive flow simulations with turbulent flame speed closure model suggested by Dinkelacker et al. [29] are performed to analyse the influence of Le_{eff} on the overall reaction rate.

After the numerical validation, the potential mechanisms responsible for the flame flashback in LSB were examined based on the observations gathered from the literature study and numerical simulations of LSB. Based on that, various hypotheses were formulated to test the conditions favouring the flashback event in LSB. This includes the local flow field analysis of the 'M', and 'V' shaped flames and investigation of the local mass flow distributions between the centre and annular swirling channels. Apart from that, two-dimensional simulations have been performed to analyse the initiation of flashback by reducing the axial velocity of the central channel. following that, the reasons for a sudden flame flashback seen in experiments [7] were argued along with the CFD calculations. Finally, a proposal for unravelling the flashback in LSB is suggested.

7.1. Conclusions

The following conclusions stated were drawn from the results discussed in the chapter 5 and chapter 6

1. The non-reacting flow simulations with SST-k-ω turbulence model were in good accordance with the experimental measurements and performed superior to Standard k-ϵ, Re-Normalisation Group k-ϵ and Realizable k-ϵ turbulence models.
2. The location of the flame fronts of hydrogen-enriched fuels predicted by the Zimont turbulent flame speed closure combustion model was nearly similar to that of experiments, Even though many assumptions were made during the geometry modelling.

3. The addition of Le_{eff} to the turbulent flame speed model (Dinkelacker model) resulted in better performance than the Zimont model for 100 vol.% of hydrogen. But for 40, 60 and 80 vol.% of hydrogen, the reaction rate produced by the Dinkelacker model was nearly identical.
4. Upon increasing the vol.% of hydrogen in the fuel mixture, the flame front moved upstream. However, the upstream flame movement was marginal due to a high-velocity gradient which is in turn due to divergence.
5. The IRZ formed in the swirling flow has no role in flame stabilization in LSB. The IRZ moved downstream upon increasing the vol.% of hydrogen in the fuel mixture due to flow acceleration produced by the flame.
6. From the experimental observations, it is said that 'M' shaped flame resulted in flame flashback and flashback was not noticed in 'V' shaped flame. So, from the numerical calculations it is proved that 'M' shaped flame was found to be more susceptible to flame flashback than 'V' shaped flame due to the high adverse pressure gradient present before the flame front in the 'M' shaped flame than 'V' shaped flame. The adverse pressure gradient before the flame hinders the incoming flow, which paves the way for the flame to propagate upstream.
7. Upon upstream flame propagation from the combustion chamber to the nozzle, the mass flow distribution between the centre and annular swirling channels was compared. Based on the comparison, less disturbance to the flow distribution between the centre and annular swirling channels was noticed.
8. Once the flame is into the nozzle; the flame propagation is facilitated by the presence of ISL above the centre channel wall and through the walls of the centre channel.

7.2. Recommendations

The occurrence of flashback was not captured by RANS and flamelet combustion models, so the following recommendations are listed for future research.

1. The implementation of the curvature correction in the k-ω - SST turbulence model was not analysed due to time constraints. But it is suggested in literature [4] to employ the k-ω - SST turbulence model with curvature correction for better prediction of swirling helical streamlines.
2. Instead of performing RANS simulations with isotropic turbulence assumption, employing RSM to model anisotropic turbulence might aid in better correlation with the experiment's measurements.
3. Perform numerical calculation with LES or DNS simulation to resolve the vortices originating form the LSI to investigate the interaction of vortices with the flame
4. Evaluate the effects of the flame due to localised stretch and non-unity Lewis number effects in LSB using the state-of-the-art combustion models employed by Pitsch [98]. Since the local behaviour of the flame front due to non-unity Lewis number effects can not be modelled in AFSW model by just including the Le_{eff} in the S_T.
5. Perform detailed experiments with LSB to better understand about the physical process leading to a flashback, which will aid in modelling the flame flashback. In addition, the flashback map for LSB can be obtained for various inlet conditions.

A

Appendix -A

This chapter presents the basic vector calculus operators and the directional derivative form of the continuity and momentum equations.

A.1. Nabla and Laplacian operators in Cartesian coordinates

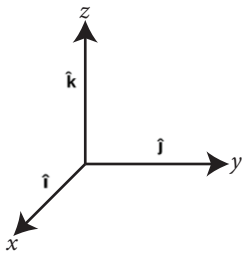

Figure A.1: Cartesian coordinates

The above figure A.1 shows the Cartesian coordinates system with unit vectors $\hat{\imath}$, $\hat{\jmath}$ and $\hat{k}$ of axes *x*, *y* and *z* respectively. Nabla operator to a scalar field signifies the gradient operation, which results in a vector field.

The gradient of a scalar field ψ:

$$\nabla\psi = \hat{\imath}\frac{\partial\psi}{\partial x} + \hat{\jmath}\frac{\partial\psi}{\partial y} + \hat{k}\frac{\partial\psi}{\partial z} \tag{A.1}$$

Upon applying the Nabla operator to a vector field, $\vec{\varphi}$ signifies the divergence, and a multiplication sign $(\cdot)$ is included between the Nabla and the vector field for lucidity. Therefore, the divergence of a vector field results in a scalar field.

The divergence of a vector field $\vec{\varphi}(\varphi_x, \varphi_y, \varphi_z)$:

$$\nabla \cdot \vec{\varphi} = \frac{\partial\vec{\varphi}_x}{\partial x} + \frac{\partial\vec{\varphi}_y}{\partial y} + \frac{\partial\vec{\varphi}_z}{\partial z} \tag{A.2}$$

The Nabla with the cross product of vector $\vec{\varphi}$ signifies the rotation of the vector field. This operation is commonly known as curl.

The curl of a vector field $\vec{\varphi}(\varphi_x, \varphi_y, \varphi_z)$:

$$\nabla \times \vec{\varphi} = \det \begin{vmatrix} \hat{i} & \hat{j} & \hat{k} \\ \partial/\partial x & \partial/\partial y & \partial/\partial z \\ \vec{\varphi_x} & \vec{\varphi_y} & \vec{\varphi_z} \end{vmatrix} \tag{A.3}$$

To note is that the cross product of any gradient of the scalar field and divergence of the cross product of the vector is zero:

$$\begin{aligned} \nabla \times (\nabla \psi) &= 0 \\ \nabla \cdot (\nabla \times \vec{\varphi}) &= 0 \end{aligned} \tag{A.4}$$

The divergence of the gradient of a scalar is known as the Laplacian operator ∇^2, The Laplacian of a vector field $\vec{\varphi}(\varphi_x, \varphi_y, \varphi_z)$:

$$\nabla^2 \vec{\varphi} = \left(\frac{\partial^2 \vec{\varphi_x}}{\partial x^2} + \frac{\partial^2 \vec{\varphi_x}}{\partial y^2} + \frac{\partial^2 \vec{\varphi_x}}{\partial z^2} \right) \hat{\imath} + \left(\frac{\partial^2 \vec{\varphi_y}}{\partial x^2} + \frac{\partial^2 \vec{\varphi_y}}{\partial y^2} + \frac{\partial^2 \vec{\varphi_y}}{\partial z^2} \right) \hat{\jmath} + \left(\frac{\partial^2 \vec{\varphi_z}}{\partial x^2} + \frac{\partial^2 \vec{\varphi_z}}{\partial y^2} + \frac{\partial^2 \vec{\varphi_z}}{\partial z^2} \right) \hat{k} \tag{A.5}$$

A.2. Vorticity vector components in Cartesian coordinates

The vorticity vector $\vec{\omega}$ as defined in equation 2.6, in Cartesian coordinates the individual components of $\vec{\omega}$:

$$\omega_x = \frac{\partial w}{\partial y} - \frac{\partial v}{\partial z} \tag{A.6}$$

$$\omega_y = \frac{\partial u}{\partial z} - \frac{\partial w}{\partial x} \tag{A.7}$$

$$\omega_x = \frac{\partial v}{\partial x} - \frac{\partial u}{\partial y} \tag{A.8}$$

The divergence of the vorticity:

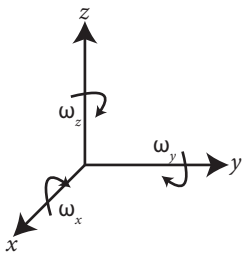

Figure A.2: Component of vorticity $\vec{\omega}$ in Cartesian coordinates

$$\frac{\partial \omega_x}{\partial x} = \frac{\partial^2 w}{\partial y \partial x} - \frac{\partial^2 v}{\partial z \partial x} \tag{A.9}$$

$$\frac{\partial \omega_y}{\partial y} = \frac{\partial^2 u}{\partial z \partial y} - \frac{\partial^2 w}{\partial x \partial y} \tag{A.10}$$

$$\frac{\partial \omega_z}{\partial z} = \frac{\partial^2 v}{\partial x \partial z} - \frac{\partial^2 u}{\partial y \partial z} \tag{A.11}$$

From the above equation, it is evident that the divergence of vorticity is zero.

$$\nabla \cdot \vec{\omega} = \frac{\partial \omega_x}{\partial x} + \frac{\partial \omega_y}{\partial y} + \frac{\partial \omega_z}{\partial z} = 0 \tag{A.12}$$

A.3. Derivation of vorticity transport equation

The vorticity transport equation can be obtained by taking curl on the momentum equation 2.5:

$$\underbrace{\nabla \times \left(\frac{\partial \vec{u}}{\partial t}\right)}_{\text{Transient term}} + \underbrace{\nabla \times ((\vec{u} \cdot \nabla)\vec{u})}_{\text{convection term}} = \underbrace{-\nabla \times \left(-\frac{1}{\rho}(\nabla p)\right)}_{\text{Pressure term}} + \underbrace{\nabla \times (\nu(\nabla^2 \vec{u}))}_{\text{Diffusion term}} + \underbrace{\nabla \times \vec{f}}_{\text{Body force}} \tag{A.13}$$

$$\text{Transient term} = \nabla \times \left(\frac{\partial \vec{u}}{\partial t}\right) = \frac{\partial \vec{\omega}}{\partial t} \tag{A.14}$$

$$\text{Convective term} = \nabla \times (\vec{u} \cdot \nabla)\vec{u} = \nabla \times \left(\nabla\left(\frac{\vec{u} \cdot \vec{u}}{2}\right) - \vec{u} \times (\nabla \times \vec{u})\right) \tag{A.15}$$

The first term in the right side is zero since the curl over the gradient of scalar ($\vec{u} \cdot \vec{u}$) is zero

$$-\vec{u} \times (\nabla \times \vec{u}) = -\vec{u}(\nabla \cdot \vec{\omega}) + \vec{\omega}(\nabla \cdot \vec{u}) + (\vec{u} \cdot \nabla)\vec{\omega} - (\vec{\omega} \cdot \nabla)\vec{u} \tag{A.16}$$

From the above vector identity, the first term on the right side ($-\vec{u}(\nabla \cdot \vec{\omega}) = -\vec{u}(\nabla \cdot \nabla \times \vec{u})$) is zero, since the divergence of the curl is zero.

$$\text{Pressure term} = \nabla \times \left(-\frac{1}{\rho}(\nabla \vec{p})\right) = -\left(\frac{1}{\rho}(\nabla \times \nabla p) + \nabla\left(\nabla\left(\frac{1}{\rho}\right) \times \nabla p\right)\right) \tag{A.17}$$

$-\frac{1}{\rho}(\nabla \times \nabla p)$ signifies the curl over the gradient of the scalar field; hence this is zero.

$$\text{Diffusive term} = \nabla \times (\nu(\nabla^2 \vec{u})) = \nu(\nabla^2 \vec{\omega}) \tag{A.18}$$

After applying all the vector identities and simplifying them, the vorticity transport equation is given as:

$$\underbrace{\frac{\partial \vec{\omega}}{\partial t} + (\vec{u} \cdot \nabla)\vec{\omega}}_{\frac{D\omega}{Dt}} = \underbrace{(\vec{\omega} \cdot \nabla)\vec{u}}_{\text{Stretching / tilting term}} - \underbrace{\vec{\omega}(\nabla \cdot \vec{u})}_{\text{Expansion term}} + \underbrace{\frac{1}{\rho^2}(\nabla \rho \times \nabla p)}_{\text{Baroclinic term}} + \underbrace{\nu\,(\nabla^2 \omega)}_{\text{Diffusion term}} \tag{A.19}$$

In 2D axisymmetric swirl, Let the velocity vector $\vec{u} = (u, v, 0)$ and vorticity vector $\vec{\omega} = (0, 0, \omega_z)$

Since $\partial/\partial z = 0$

The stretching term $= (\vec{\omega} \cdot \nabla)\vec{u} = \left(\omega_x(\partial/\partial x) + \omega_y(\partial/\partial y) + \omega_z(\partial/\partial z)\right)\vec{u}$

$$(\omega.\nabla)\vec{u} = 0 \tag{A.20}$$

Since ω_x and ω_y are zero.

A.4. 2D axisymmetric swirl governing equations

Continuity equation

$$\nabla \cdot V = \frac{\partial V_z}{\partial z} + \frac{\partial V_r}{\partial r} + \frac{V_r}{r} = 0 \tag{A.21}$$

Axial momentum equation

$$\begin{aligned}\frac{\partial V_z}{\partial t} + \frac{1}{r}\frac{\partial}{\partial z}\left(rV_zV_z\right) + \frac{1}{r}\frac{\partial}{\partial r}\left(rV_rV_z\right) = &-\frac{1}{\rho}\frac{\partial p}{\partial z} + \frac{1}{r}\frac{\partial}{\partial z}\left[r\left(\frac{\mu}{\rho}\right)2\frac{\partial V_z}{\partial z}\right] \\ &+ \frac{1}{r}\frac{\partial}{\partial r}\left[r\left(\frac{\mu}{\rho}\right)\left(\frac{\partial V_z}{\partial r} + \frac{\partial V_r}{\partial z}\right)\right]\end{aligned} \tag{A.22}$$

Tangential momentum equation

$$\begin{aligned}\frac{\partial V_\theta}{\partial t} + \frac{1}{r}\frac{\partial}{\partial z}\left(rV_zV_\theta\right) + \frac{1}{r}\frac{\partial}{\partial r}\left(rV_rV_\theta\right) = &-\frac{V_rV_\theta}{r} + \frac{1}{r}\frac{\partial}{\partial z}\left[r\left(\frac{\mu}{\rho}\right)\frac{\partial V_\theta}{\partial z}\right] \\ &+ \frac{1}{r^2}\frac{\partial}{\partial r}\left[r^3\left(\frac{\mu}{\rho}\right)\frac{\partial}{\partial r}\left(\frac{V_\theta}{r}\right)\right]\end{aligned} \tag{A.23}$$

Radial momentum equation

$$\begin{aligned}\frac{\partial V_r}{\partial t} + \frac{1}{r}\frac{\partial}{\partial z}\left(rV_zV_r\right) + \frac{1}{r}\frac{\partial}{\partial r}\left(rV_rV_r\right) = &-\frac{1}{\rho}\frac{\partial p}{\partial r} + \frac{V_\theta^2}{r} + \frac{1}{r}\frac{\partial}{\partial z}\left[r\left(\frac{\mu}{\rho}\right)\left(\frac{\partial V_r}{\partial z} + \frac{\partial V_z}{\partial r}\right)\right] \\ &+ \frac{1}{r}\frac{\partial}{\partial r}\left[r\left(\frac{\mu}{\rho}\right)2\frac{\partial V_r}{\partial r}\right] - 2\left(\frac{\mu}{\rho}\right)\frac{V_r}{r^2}\end{aligned} \tag{A.24}$$

B

Appendix -B

In this chapter, the modelling equations of the two-equation turbulent model and Reynolds Stress Model (RSM) are discussed in detail.

B.1. Standard k-ϵ (SKE) model

SKE model is the most popular and robust two-equation model. SKE model is a semi-empirical model which consists of a transport equation for turbulent kinetic energy k and dissipation rate ϵ which is related by the turbulent viscosity formulation defined in equation B.1. The transport equation of k, ϵ and ν_T is defined as follows,

$$\nu_T = C_\mu \frac{k^2}{\epsilon} \tag{B.1}$$

$$\frac{\partial}{\partial t}(\bar{\rho}k) + \frac{\partial}{\partial x_i}(\bar{\rho}k\tilde{u}_i) = \frac{\partial}{\partial x_j}\left[\left(\mu + \frac{\mu_t}{\sigma_k}\right)\frac{\partial k}{\partial x_j}\right] + P_k - \bar{\rho}\epsilon \tag{B.2}$$

$$\frac{\partial}{\partial t}(\bar{\rho}\epsilon) + \frac{\partial}{\partial x_i}(\bar{\rho}\epsilon\tilde{u}_i) = \frac{\partial}{\partial x_j}\left[\left(\mu + \frac{\mu_t}{\sigma_\epsilon}\right)\frac{\partial \epsilon}{\partial x_j}\right] + C_{\epsilon 1}\frac{\epsilon}{k}P_k - C_{\epsilon 2}\bar{\rho}\frac{\epsilon^2}{k} \tag{B.3}$$

$$P_k = -\bar{\rho}\widetilde{u_i'' u_j''}\frac{\partial \tilde{u}_j}{\partial x_i} \tag{B.4}$$

where σ_k and σ_ε are turbulent Prandtl numbers with value 1 and 1.3 respectively, which accounts for the turbulent diffusion of k and ϵ takes the value 1 and 1.3. $C_{\varepsilon 1}$ and $C_{\varepsilon 2}$ are empirical model constants with values 1.44 and 1.92. [55] and the model constant C_μ in equation B.1 takes the value of 0.09. The constants mentioned above are determined based on the experimental flow data of simple turbulent flows involving boundary layers and mixing layers. P_k is the TKE production term due to mean velocity gradients, and it is calculated from the equation B.4. The last term in equation B.2 (ϵ) act as a sink term, and ϵ is high near the walls and in shear layers since a large number of eddies are expected to shed.

The SKE model is robust and accurate for simple flows and performs poorly for flow with strong separation, swirling, and high pressure and velocity gradient. The other downside of this equation is the excessive prediction of TKE in the regions of high strain rate. In addition,

the SKE model performs poorly in the viscosity dominated regions (near the wall) because SKE is developed based on the assumptions that flow is fully developed and molecular viscosity is negligible. However, this is addressed by modelling the near wall region by two layer model or by introducing wall functions. The two layer model uses the low Reynolds number model in the near wall region and SKE in the rest of the region, while the latter is built based on the assumption that all turbulent flow behaves similarly in the near wall region. The near wall modelling strategy is discussed elaborately in subsection 2.3.1. Since the SKE model fails to accurately predict the complex flows with high strain rate different variants of k-ϵ model was developed, which is discussed in the upcoming sections. All the k-ϵ model differs in calculating the model equation of turbulent dissipation. The model equation of TKE is the same for all the k-ϵ models since the model equation for the TKE is derived from the exact equation., It is worth noting that the generation of k and ϵ due to effects of compressibility and buoyancy is neglected in all k-ϵ models.

B.2. Re - Normalisation Group k-ϵ (RNG) model

The RNG k-ϵ model was derived by applying the statistical technique named Re-Normalization Group (RNG) theory. This model is similar to k-ϵ along with some improvisations to accurately model flows with high strain rate, swirl, and separation, and it also accounts for low Reynolds's number effects. The formulation of the eddy viscosity is same as that of k-ϵ model for high Reynolds's number flows and the model constant C_μ in equation B.1 takes the value of 0.0845 which is slightly less from k-ϵ model. The differential equation given below is obtained from the RNG theory for low Reynolds's number flows and is solved to get the effective viscosity concerning Reynolds's number.

$$d\left(\frac{\rho^2 k}{\sqrt{\varepsilon\mu}}\right) = 1.72\frac{\hat{v}}{\sqrt{\hat{v}^3 - 1 + C_v}}d\hat{v} \tag{B.5}$$

$$\hat{v} = \frac{\nu_{eff}}{\nu}, \quad \nu_{eff} = \nu_t + \nu, \quad C_v \approx 100 \tag{B.6}$$

The turbulent viscosity is calculated from the above relation when the differential viscosity model option is enabled in ANSYS Fluent; otherwise, it is calculated from equation B.1. RNG model also provides an option to include effects of swirl on turbulence only for three-dimensional flows based on the functional relation mentioned below,

$$\nu_t = \nu_{t*}\, f(\alpha_s, \Omega_s, \frac{k}{\epsilon}) \tag{B.7}$$

ν_{t*} is calculated from equation B.1 and B.5. The α_s is the swirl factor which is a constant, and it takes different values depending upon the swirl strength. It is set to 0.07 by default in ANSYS Fluent, which is for mild swirling flow however, α_s can be changed depending on the swirling strength. Ω_s is the swirl number calculated within ANSYS Fluent. The transport equations of TKE are same as that of SKE (equation B.2), and the transport equation of eddy dissipation is defined as follows,

$$\frac{\partial}{\partial t}(\bar{\rho}\epsilon) + \frac{\partial}{\partial x_i}(\bar{\rho}\epsilon\tilde{u}_i) = \frac{\partial}{\partial x_j}\left[\left(\mu + \frac{\mu_t}{\sigma_\epsilon}\right)\frac{\partial \epsilon}{\partial x_j}\right] + C_{\epsilon 1}\frac{\epsilon}{k}P_k - C_{\epsilon 2}\bar{\rho}\frac{\epsilon^2}{k} - R_\epsilon \tag{B.8}$$

R_ϵ is the extra term included in the ϵ equation to enhance the prediction of strained flows. R_ϵ is given as follows,

$$R_\varepsilon = \frac{C_\mu \rho \eta^3 \left(1 - \eta/\eta_0\right)}{1 + \beta \eta^3} \frac{\varepsilon^2}{k} \tag{B.9}$$

where,

$$\eta = \sqrt{S_{ij}^2}\, \frac{k}{\epsilon} \tag{B.10}$$

Where α_k and α_ϵ are inverse effective Prandtl numbers, and it is approximately equal to 1.393 for high Reynolds's number. Model constants $C_{\varepsilon 1}$, $C_{\varepsilon 2}$, η_0 and β are 1.42, 1.68, 4.38 and 0.012 respectively. Apart from β, all other constants mentioned above are calculated analytically by RNG theory.

B.3. Realizable k-ϵ (RKE) model

Since the SKE model doesn't provide superior results for the flows with separation, swirling and recirculation. Shih et al. [111] modified the SKE model and came up with the RKE model. RKE model performed superior to the SKE model for low to moderate swirl flows than any other turbulence model. The transport equation of TKE is the same as the SKE model (equation B.2), and eddy dissipation has a modified transport equation which is derived from the exact transport equation of the mean square vorticity fluctuation.

$$\frac{\partial}{\partial t}(\bar{\rho}\epsilon) + \frac{\partial}{\partial x_i}(\bar{\rho}\epsilon\tilde{u}_i) = \frac{\partial}{\partial x_j}\left[\left(\mu + \frac{\mu_t}{\sigma_\epsilon}\right)\frac{\partial \epsilon}{\partial x_j}\right] + \bar{\rho} C_1 S_\epsilon - \bar{\rho} C_2 \frac{\epsilon^2}{k + \sqrt{v\epsilon}} \tag{B.11}$$

Where,

$$C_1 = max[0.43, \frac{\eta}{\eta + 5}], \quad \eta = S\frac{k}{\epsilon}, \quad S = \sqrt{2 S_{ij} S_{ij}} \tag{B.12}$$

The model constants C_2, σ_k and σ_ϵ has the value 1.9, 1 and 1.2 respectively. The main difference between the SKE and RKE models lies in defining the model constant C_μ in equation B.1. C_μ is no longer a constant in RKE, and it is defined as given below,

$$C_\mu = \frac{1}{A_0 + A_s \frac{kU^*}{\epsilon}} \tag{B.13}$$

Where,

$$U^* = \sqrt{S_{ij} Sij + \widetilde{\Omega_{ij}}\widetilde{\Omega_{ij}}} \tag{B.14}$$

and

$$\widetilde{\Omega_{ij}} = \Omega_{ij} - 2\epsilon_{ijk}\omega_k \tag{B.15}$$

$$\Omega_{ij} = \overline{\Omega_{ij}} - \epsilon_{ijk}\omega_k \tag{B.16}$$

$$\Omega_{ij} = \frac{1}{2}\left(\frac{\partial \overline{u_i}}{\partial x_j} - \frac{\partial \overline{u_j}}{\partial x_i}\right) \tag{B.17}$$

$\overline{\Omega_{ij}}$ is the mean rotation tensor with the angular velocity ω_k. It is worth to note that the last term in equation B.15 is not included by default in Ansys fluent. A_0 and A_s are the model constants and they take the value of 4.04 and $\sqrt{6}cos(\phi)$, where ϕ is modelled as follows,

$$\phi = \frac{1}{3}\cos^{-1}(\sqrt{6}W), \quad W = \frac{S_{ij}S_{jk}S_{ki}}{\tilde{S}^3} \tag{B.18}$$

B.4. Standard k-ω (SKW) model

Since the SKE model cannot accurately predict the boundary layers with adverse pressure gradients and is not suitable for low Reynolds's number flows, the SKW model was developed by Wilcox [128] to model such flows. Instead of solving the ϵ transport equation, a new form of turbulent dissipation called ω is solved. However, both ϵ and ω represent turbulent dissipation, and they are related as defined in equation B.19.

$$\omega = \frac{\epsilon}{\beta^* k} \tag{B.19}$$

The formulation of ν_t is defined as,

$$\nu_t = \alpha^* \frac{k}{\omega} \tag{B.20}$$

The relation for α^* is defined equation B.21 which includes the low Reynolds's number correction. This relation was added in order to damp the artificial turbulent viscosity developed in low Reynolds's number flows.

$$\alpha^* = \alpha^*_\infty \left(\frac{\alpha^*_0 + Re_t/R_k}{1 + Re_t/R_k} \right) \tag{B.21}$$

$$Re_t = \nu \frac{k}{\omega} \quad \alpha^*_0 = \frac{\beta_i}{3} \tag{B.22}$$

where α^*_0, R_k and β_i are constants and they take the value of 1, 6 and 0.072 respectively. However, for high Reynolds's number flows, α^* is equal to 1. Transport equations of TKE and ω are stated as follows,

$$\frac{\partial(\rho k)}{\partial t} + \frac{\partial\left(\rho k u_i\right)}{\partial x_i} = \frac{\partial}{\partial x_j}\left(\left(\mu + \frac{\mu_t}{\sigma_k}\right)\frac{\partial k}{\partial x_j}\right) + P_k - \beta^* \rho \omega k \tag{B.23}$$

$$\frac{\partial(\rho \omega)}{\partial t} + \frac{\partial\left(\rho \omega u_i\right)}{\partial x_i} = \frac{\partial}{\partial x_j}\left(\left(\mu + \frac{\mu_t}{\sigma_\omega}\right)\frac{\partial \omega}{\partial x_j}\right) + P_\omega - \beta \rho \omega^2 \tag{B.24}$$

where P_K is same as SKE (equation B.4). P_ω accounts for the production of turbulent dissipation and it is defined in equation B.25. σ_k and σ_ω are model constants equal to 2.

$$P_\omega = \alpha P_k \frac{\omega}{k} \tag{B.25}$$

Where the coefficient α for the low Reynolds's number flows is given by,

$$\alpha = \frac{\alpha_\infty}{\alpha^*}\left(\frac{\alpha_0 + Re_t/R_\omega}{1 + Re_t/R_\omega}\right) \tag{B.26}$$

α^*_0 and R_ω is equal to 0.52 and 2.95. For high Reynolds's number flows the above relation pf α is simplified into a constant equal to unity. The auxiliary relations for coefficients β^* in equation B.23 are defined as follows,

$$\beta^* = \beta^*_0 f_{\beta *} \tag{B.27}$$

$$\beta^*_0 = \beta^*_\infty \left(\frac{(4/15) + \left(Re_t/R_\beta\right)^4}{1 + \left(Re_t/R_\beta\right)^4} \right) \quad , \quad f_{\beta *} = \left\{ \begin{array}{ll} 1, & \chi_k \leq 0 \\ \frac{1+680\chi_k^2}{1+400\chi_k^2}, & \chi_k > 0 \end{array} \right\} \tag{B.28}$$

$$\chi_k \equiv \frac{1}{\omega^3}\frac{\partial k}{\partial x_j}\frac{\partial \omega}{\partial x_j} \tag{B.29}$$

Where, β^*_∞ and R_β are constants and they takes the value 0.09 and 8 respectively. β^*_0 is equal to unity for high Reynolds's number flows. The auxiliary relations for coefficients β in equation B.24 are defined as follows,

$$\beta = \beta_0 f_\beta \tag{B.30}$$

$$f_\beta = \frac{1+70\chi_\omega}{1+80\chi_\omega} \quad , \quad \chi_\omega = \left|\frac{\Omega_{ij}\Omega_{jk}S_{ki}}{(\beta^*_0\omega)^3}\right| \tag{B.31}$$

Where the closure coefficient β_0 takes the value 0.072. All the mentioned low Reynolds's number correction takes effect when the low Re option is checked in Fluent. The main downside of the SKW model is that it is dependent on the free stream turbulence boundary condition (k_∞ and ω_∞). Even a slight change in k_∞ leads to a significant shift in turbulent viscosity [61].

Since the SKW model is sensitive to free stream values of turbulence parameters defined at the inlet of the computational domain. Menter developed a baseline k-ω model (BSLKW) [84]. BSLKW model is a combination of the SKW and SKE model. Menter employed blending functions in the BSL model, which is designed so that SKW is modelled in the boundary layer and free stream independent SKE in regions other than the boundary layer. In the BSLKW model, the transport equation of ω includes an extra, which represents cross-diffusion. The cross diffusion term arises due to blending both SKE and SKW. However, BSLKW is not employed in this thesis; instead, a developed version of the BSLKW model is utilised, which is discussed in the next section.

B.5. Shear Stress Transport k-ω (SSTKW) model

The SSTKW model is an improvised version of the BSLKW model. SSTKW model incorporates all the transformations made in the SKW model to develop the BSLKW model. In addition to the refinements mentioned above, the effect of transport of turbulence shear stress is included in the turbulent viscosity definition in the SSTKW model. The turbulent viscosity formulation for the SSTKW model is defined in equation B.32.

$$\nu_t = \frac{k}{\omega}\frac{1}{\max\left[\frac{1}{\alpha^*}, \frac{SF_2}{a_1\omega}\right]}S \tag{B.32}$$

Where S is the magnitude of strain rate and F_2 is one of the blending functions defined in equation B.33.

$$F_2 = \tanh(\Phi_2^2) \quad , \quad \Phi_2 = \max\left[2\frac{\sqrt{k}}{0.09\omega y}, \frac{500\mu}{\rho y^2\omega}\right] \tag{B.33}$$

The empirical constants α^* are the same as the SKW model (equation B.21). a_1 is a model constant with a value of 0.31 and y is the distance to the next surface region from the no-slip boundary condition. The TKE and ω transport equations of SSTKW are defined as follows,

$$\frac{\partial(\rho k)}{\partial t} + \frac{\partial(\rho k u_i)}{\partial x_i} = \frac{\partial}{\partial x_j}\left(\left(\mu + \frac{\mu_t}{\sigma_k}\right)\frac{\partial k}{\partial x_j}\right) + P_k - \beta^*\rho\omega k \tag{B.34}$$

$$\frac{\partial(\rho\omega)}{\partial t} + \frac{\partial(\rho\omega u_i)}{\partial x_i} = \frac{\partial}{\partial x_j}\left(\left(\mu + \frac{\mu_t}{\sigma_\omega}\right)\frac{\partial \omega}{\partial x_j}\right) + P_\omega + D_\omega - \beta\rho\omega^2 \tag{B.35}$$

The turbulent Prandtl numbers σ_k and σ_ω are defined below,

$$\sigma_k = \frac{1}{F_1/\sigma_{k,1} + (1-F_1)/\sigma_{k,2}} \quad , \quad \sigma_\omega = \frac{1}{F_1/\sigma_{\omega,1} + (1-F_1)/\sigma_{\omega,2}} \tag{B.36}$$

Where, the model constants $\sigma_{k,1}$, $\sigma_{k,2}$, $\sigma_{\omega,1}$ and $\sigma_{\omega,2}$ takes the value 1.176, 1, 2 and 1.168 respectively. The blending function F_1 and their corresponding correlations are given as follows,

$$F_1 = \tanh\left(\Phi_1^4\right), \quad \Phi_1 = \min\left[\max\left(\frac{\sqrt{k}}{0.09\omega y}, \frac{500\mu}{\rho y^2 \omega}\right), \frac{4\rho k}{\sigma_{\omega,2} D_\omega^+ y^2}\right] \tag{B.37}$$

$$D_\omega^+ = \max\left[2\rho \frac{1}{\sigma_{\omega,2}} \frac{1}{\omega} \frac{\partial k}{\partial x_j} \frac{\partial \omega}{\partial x_j}, 10^{-10}\right] \tag{B.38}$$

D_ω^+ is the positive portion of the cross diffusive term. The turbulent production term in equation B.34 is due to velocity gradient P_k is defined in equation B.4 which is same as SKE and SKW. The production term P_ω in equation B.35 is defined as follows,

$$P_\omega = \frac{\alpha \alpha^*}{\nu_t} P_k \tag{B.39}$$

Where, α and α^* are defined in equation B.26 and B.21. The main difference between SKW and SSTKW lies in calculating the α_∞ in equation B.26, in SKW α_∞ is defined as a constant whereas in SSTKW model α_∞ is defined as,

$$\alpha_\infty = F_1 \alpha_{\infty,1} + (1-F_1)\, \alpha_{\infty,2} \tag{B.40}$$

$$\alpha_{\infty,1} = \frac{\beta_{i,1}}{\beta_\infty^*} - \frac{\kappa^2}{\sigma_{\omega,1}\sqrt{\beta_\infty^*}} \quad , \quad \alpha_{\infty,2} = \frac{\beta_{i,2}}{\beta_\infty^*} - \frac{\kappa^2}{\sigma_{\omega,2}\sqrt{\beta_\infty^*}} \tag{B.41}$$

Where, $\beta_{i,1}$, $\beta_{i,1}$ and κ are model constants with value 0.075, 0.0828 and 0.41 respectively. The last term in equation B.34 and equation B.35 accounts for the dissipation of k and ω and they are treated in a similar way as they are defined in SKW but they varies in calculating the functions f_b^*, f_b and constant β_0. In SSTKW the f_b^* and f_b are defined as constants equal to unity and β_0 is defined as follows,

$$\beta_0 = F_1 \beta_{i,1} + (1-F_1)\, \beta_{i,2} \tag{B.42}$$

The cross diffusion term in equation B.35 is defined as follows,

$$D_\omega = 2\,(1-F_1)\,\rho \frac{1}{\omega \sigma_{\omega,2}} \frac{\partial k}{\partial x_j} \frac{\partial \omega}{\partial x_j} \tag{B.43}$$

B.6. Reynolds Stress Model (RSM)

Unlike eddy viscosity models RSM model avoids the eddy viscosity assumption. RSM model solves the transport equations of all the six individual Reynolds stress terms. The Reynolds's stress tensor R_{ij} closure requires six transport equations along with an equation to model the dissipation rate. This approach is computationally expensive since it introduces an additional seven equations to model R_{ij} and dissipation rate. Like two-equation models, even RSM models depend on the turbulent dissipation scale equation. RSM model is most suitable for complex flows with anisotropic turbulence. RSM transport equation is derived by multiplying

the fluctuating terms with the momentum equation. The transport equations of the RSM model are defined as,

$$\begin{aligned}\frac{\partial}{\partial t}\left(\rho\overline{u_i'u_j'}\right)+\frac{\partial}{\partial x_k}\left(\rho u_k\overline{u_i'u_j'}\right)=&\frac{\partial}{\partial x_k}\left[\mu\frac{\partial}{\partial x_k}\left(\overline{u_i'u_j'}\right)\right]-\rho\left(\overline{u_i'u_k'}\frac{\partial u_j}{\partial x_k}+\overline{u_j'u_k'}\frac{\partial u_i}{\partial x_k}\right)\\&-2\rho\Omega_k\left(\overline{u_j'u_m'}\epsilon_{ikm}+\overline{u_j'u_m'}\epsilon_{ikm}\right)\\&-\frac{\partial}{\partial x_k}\left[\overline{\rho u_i'u_j'u_k'}+\overline{p\left(\delta_{kj}u_i'+\delta_{ik}u_j'\right)}\right]\\&+\overline{p\left(\frac{\partial u_i'}{\partial x_j}+\frac{\partial u_j'}{\partial x_i}\right)}-2\mu\overline{\frac{\partial u_i'}{\partial x_k}\frac{\partial u_i'}{\partial x_k}}\end{aligned}\tag{B.44}$$

Molecular diffusion $D_{L,ij}$, Stress production p_{ij} and production due to system rotation F_{ij} in equation B.44 do not require additional modelling since the terms are known. Whereas the last three terms, turbulent diffusion $D_{T,ij}$, pressure strain ϕ_{ij} and dissipation ϵ_{ij} require additional modelling. It is worth noting that the turbulent production due to buoyancy is neglected in equation B.44. In Fluent, RSM has different combinations, which differ in modelling the pressure strain and dissipation term. Different model combinations of RSM available in Fluent are,

- Linear pressure strain model
- Quadratic pressure strain model
- Stress omega model
- Stress BSL model

The first two classifications are based on modelling the p_{ij} term. The following two are classified based on the scale equation chosen to solve the turbulent dissipation. The stress omega model solves the transport equation of turbulent dissipation defined in SKW, whereas the stress BSL model solves the ϵ equation of the BSLKW model. The advantage of the stress BSL model over the stress omega model is the former is void of free stream dependencies. The last two models use the linear pressure strain model to close p_{ij} term. The pressure strain model mentioned above is not discussed in this thesis; it is discussed elaborately by Johansson and Hallbäck [52] and Speziale et al. [115]. The modelling equations of The turbulent diffusion term equation B.44 is identical to all RSM model combination, and they are given as follows,

$$D_{T,ij}=\frac{\partial}{\partial x_k}\left(\frac{\mu_t}{\sigma_k}\frac{\partial}{\partial x_k}\overline{u_i'u_j'}\right)\tag{B.45}$$

Where, μ_t is defined in equation B.1 and $\sigma_k$takes the value 0.82. Though RSM is computationally expensive, flow prediction in RSM is limited by the closure approximations assumed to model the last three terms in equation B.44, particularly p_{ij} and ϵ_{ij} terms. Even though RSM is superior to all eddy viscosity turbulence models, RSM is not employed in this thesis due to brevity.

C

Appendix -C

In this chapter, different meshes employed in this study are discussed in detail. The meshing techniques used for the nozzle and the combustion chamber are briefed. Furthermore, meshes created in different packages are verified.

C.1. Meshing Methodology of LSB

In this section, the meshing methodologies of LSB with LSI are briefed.

C.1.1. Meshing methodology of LSI nozzle

The complete flow domain can be meshed easily in an unstructured manner with tetrahedral cells in 3D. But this results in a larger number of cells compared to structured meshing. In addition to that, unstructured mesh results in poor convergence and numerical diffusion.

The structured hexahedral mesh produces a numerically stable and better resolution than the unstructured mesh. The structured mesh for the nozzle is difficult to construct since the nozzle consists of LSI. Hence, a hybrid or mixed meshing strategy is employed in this study. An unstructured tetrahedral mesh is created in and around the LSI, and the rest of the nozzle was structurally meshed with hexahedral cells as shown in figure C.1 (a). For parts 1, 2 and 4 in figure C.1 (a)), a structured mesh was created by radially dividing the nozzle into two parts, one to create a rectangular mesh at the centre (part 1 figure C.1 (b)) and another to create a cylindrical mesh. Further, to create a uniform cylindrical mesh, the cylindrical part was divided into four equal volumes (part 2,3, 4 and 5 in figure C.1 (b)) surrounding the rectangular mesh.

The above-discussed nozzle meshing methodology (LSI-N1) was initially implemented for non-reacting flow simulations representing the experimental setup of Cheng and Littlejohn [20]. Later, the mesh around the LSI was also modified to create a mesh with a high number of hexahedral cells by limiting tetrahedral cells, as shown in figure C.2 (a). figure C.2 (a) represents the mesh assembly of LSI representing the experimental setup of Cheng et al. [19], where the swirling annular region and the perforated or turbulence plate (part 1 in figure C.2 (a)) is meshed with tetrahedral elements whilst the other volume part of the centre channel were meshed with hex elements. Hence, the LSI was meshed in two different ways in this study, the LSI with complete tetrahedral cells (LSI-N1) as shown in figure C.1 and LSI with mixed cells (LSI-N2) as shown in figure C.2. LSI-N2 is implemented in reacting flow simulations and flashback analysis.

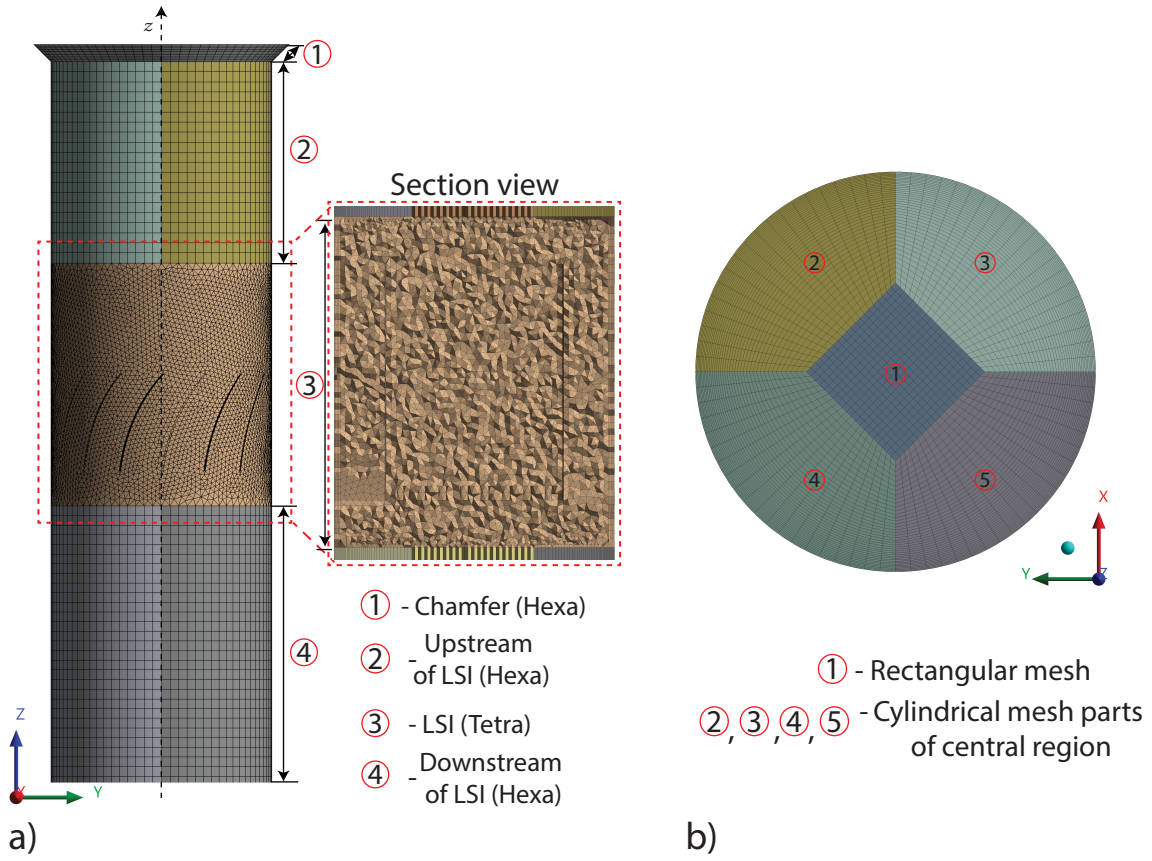

Figure C.1: 3D mixed mesh of the nozzle (LSI-N1)(a) and bottom view of the nozzle (b) representing the experimental setup of Cheng and Littlejohn [20]

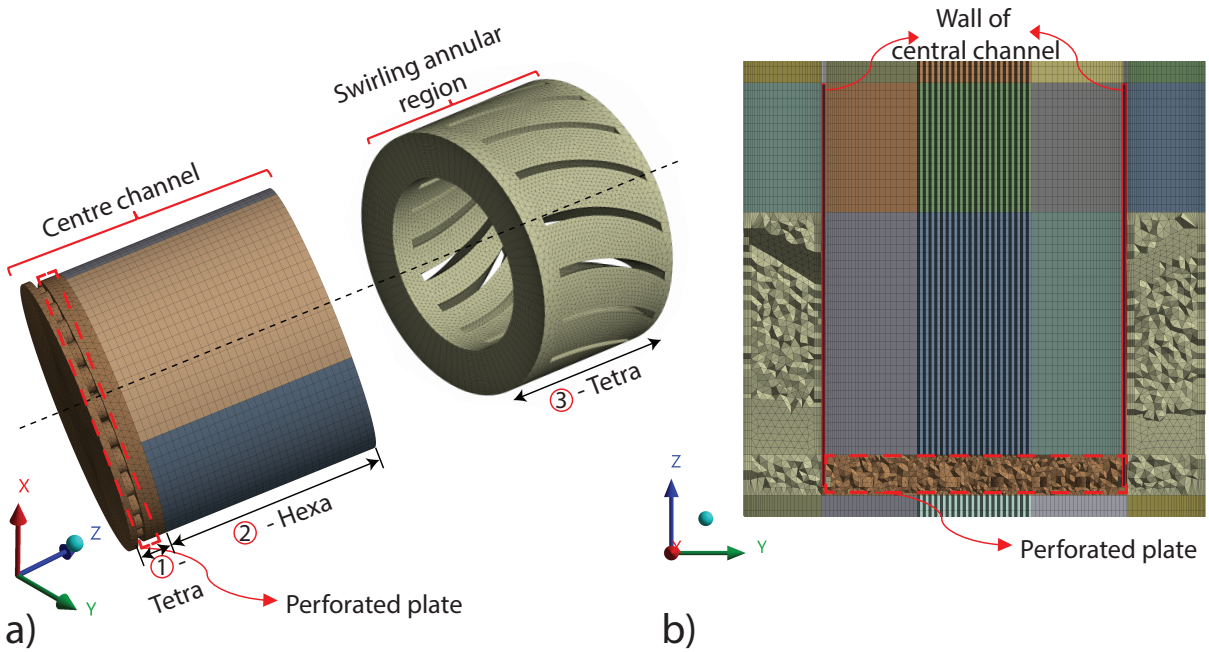

Figure C.2: Meshing strategy of LSI with mixed elements (a) and sectioned view of the LSI-N2 (b) representing the experimental setup of Cheng and Littlejohn [20]

The main difference between LSI-N1 and LSI-N2 is the radial division of LSI into two parts in the latter, namely the centre channel and the swirling annular region. Hence the upstream and downstream portions of LSI should also be fragmented accordingly, as shown in figure C.3 (b). To avoid the skewed cells near the wall of the centre channel in the nozzle section, an intersection region linking the annular and central region was divided further as shown in figure C.3 (b). The nozzle section downstream of the LSI was separated into thirteen volume parts, and the upstream section of the LSI was separated into nine volume parts as shown in figure C.3 (a) and (b), respectively.

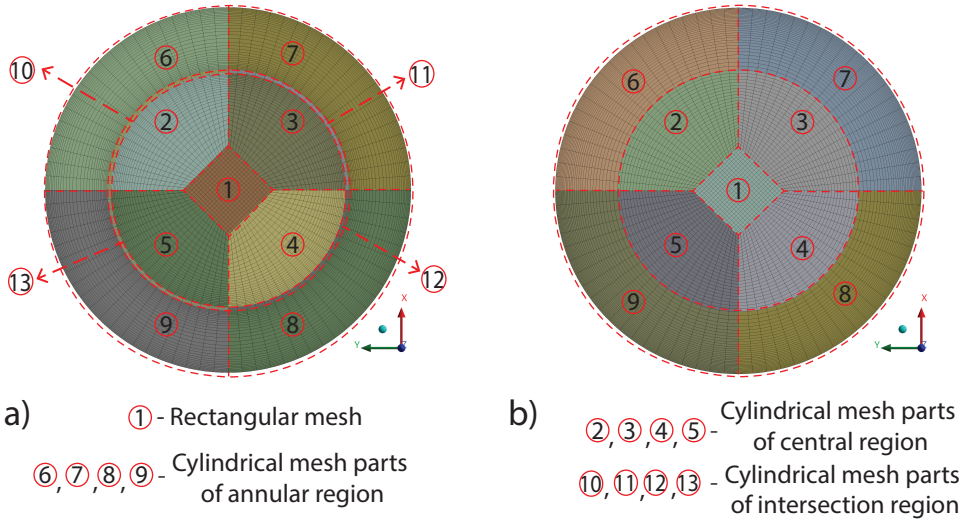

Figure C.3: Top view (a) and bottom view (b) of meshed nozzle representing the downstream and upstream portion of LSI-N2, respectively.

C.1.2. Meshing methodology of combustion chamber

The suddenly expanding combustion chamber starting from the end of the nozzle is meshed in a structured fashion. The structured meshing methodology discussed in the previous section is also applied to the combustion chamber and extension. So the combustion chamber is divided into inner, shear and outer regions as shown in figure C.4.

The mesh control of the inner region was the same as that of the nozzle (LSI-N1 and LSI-N2) to maintain the mesh continuity between the nozzle and the combustion chamber. The shear region was meshed finely due to the presence of shear layers where high-velocity gradients exist [19]. The mesh towards the enclosure was finely meshed to get a Y^+ value required to resolve the viscous sublayer. The cell sizes varied linearly, and less than 20 % of the change in cell sizes were maintained in radial, tangential and axial directions. The size of the cells was determined based on the mesh independence study, which will be discussed in the next section. The extension was meshed with the same mesh controls as the combustion chamber in the radial direction, whereas the axial cell division was increased linearly by a factor of 2 from the end of the enclosure.

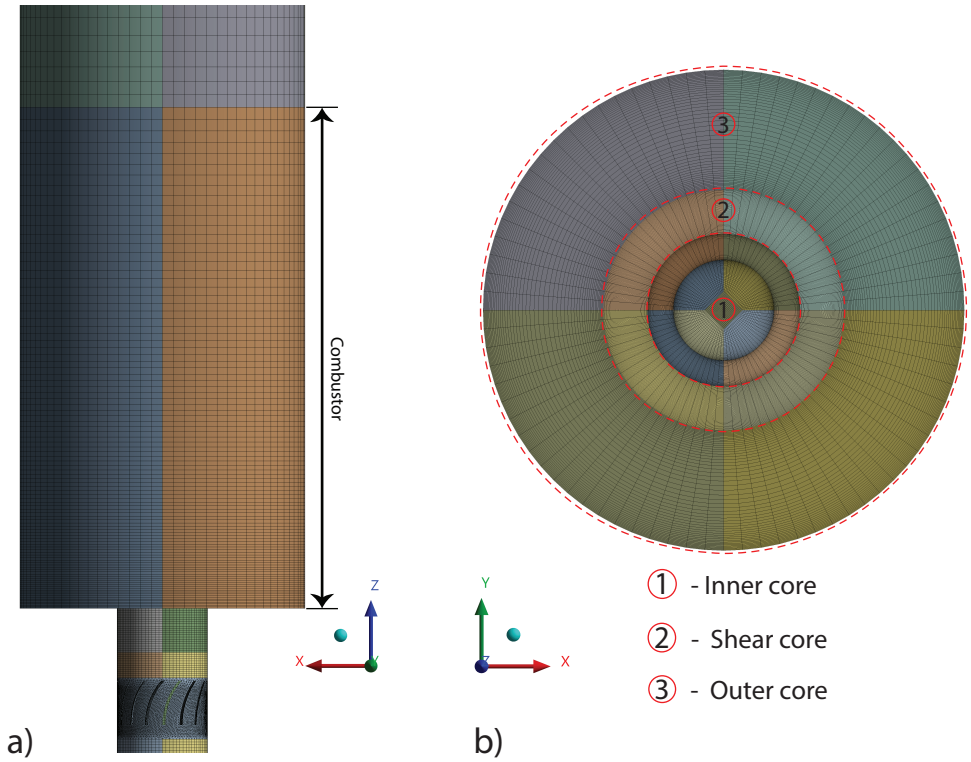

Figure C.4: 3D mesh of Combustion chamber connecting the nozzle (a) and top view of the combustion chamber representing the radial division of combustion chamber.

C.2. Mesh without LSI

Mesh for the 2D domain shown in figure 4.3 (b) was created to perform simulations in 2D. Though 3D simulation gives a more reliable solution than 2D, The effect of neglecting the azimuthal direction and LSI is to be studied in this study. Therefore, a 3D domain without LSI was modelled and meshed. The 3D structured mesh without LSI can be easily generated with fewer splits compared to mesh with LSI. The generated mesh in 2D and 3D without LSI are shown in subsection C.2.1 and C.6.

C.2.1. Two-Dimensional (2-D) Mesh

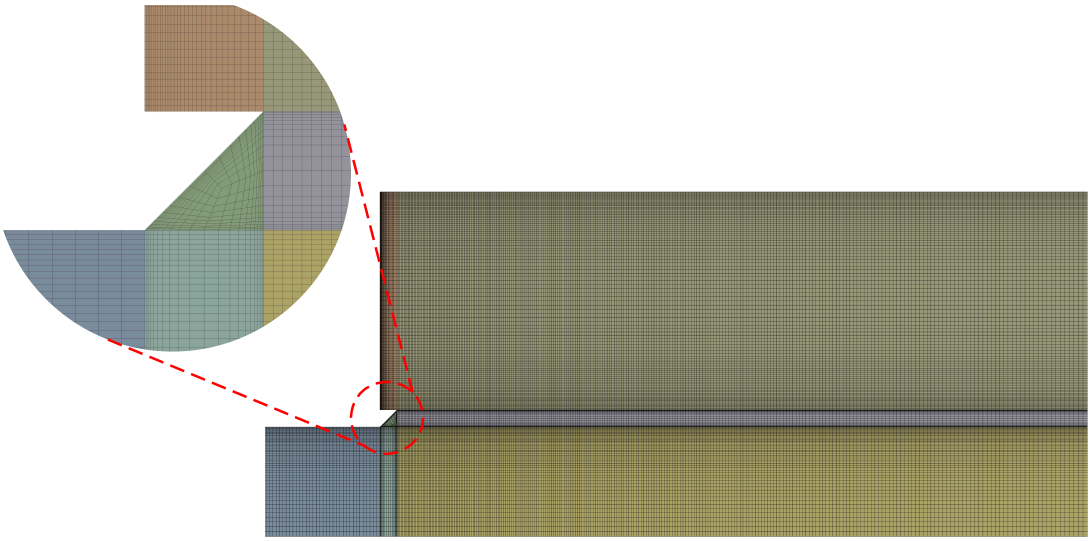

Figure C.5: 2D Mesh

C.3. Three-Dimensional (3-D) Mesh without LSI

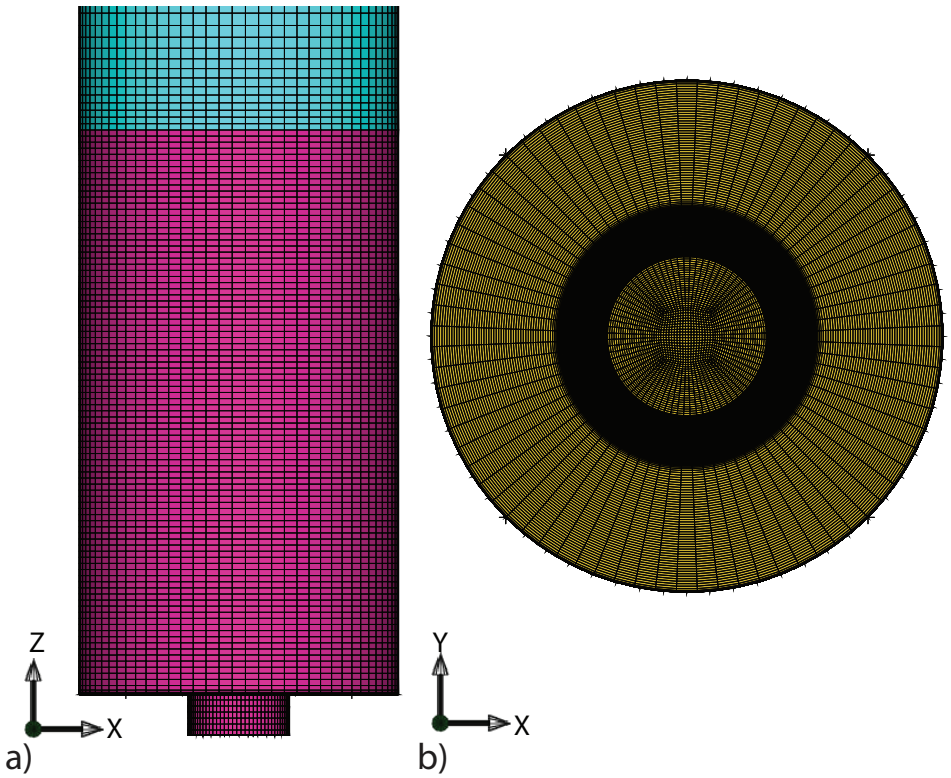

Figure C.6: 3D mesh generated in ICEM CFD to evaluate the absence of LSI in the model

C.3.1. Verification of three-Dimensional mesh without LSI

In this section, the three-dimensional mesh created in ICEM CFD was validated with the mesh created with LSI. Further, the three-dimensional mesh without LSI is refined to get a y^+ = 1 to study the y^+ influence.

The radial profile of the static pressure obtained from the three-dimensional simulations with and without LSI of the same y^+ value of 10 is compared in figure C.7. The profiles were taken at the inlet (without LSI) and Z = -20 mm (with LSI), where the velocity profiles were extracted. In addition, refined mesh (without LSI) with y^+ = 1 is included for the comparison.

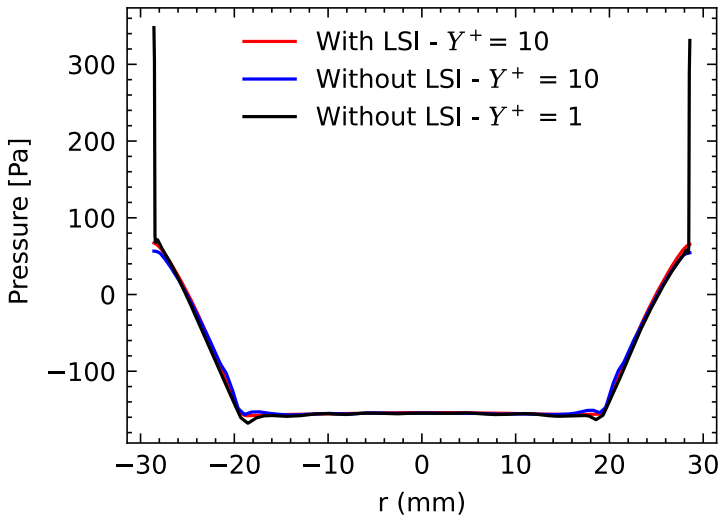

Figure C.7: Comparison of the radial profile of normalized static pressure at the inlet (without LSI) and Z = -20 mm (with LSI)

The axial velocity along the axis of two different meshes with LSI and without LSI is shown in figure C.8.

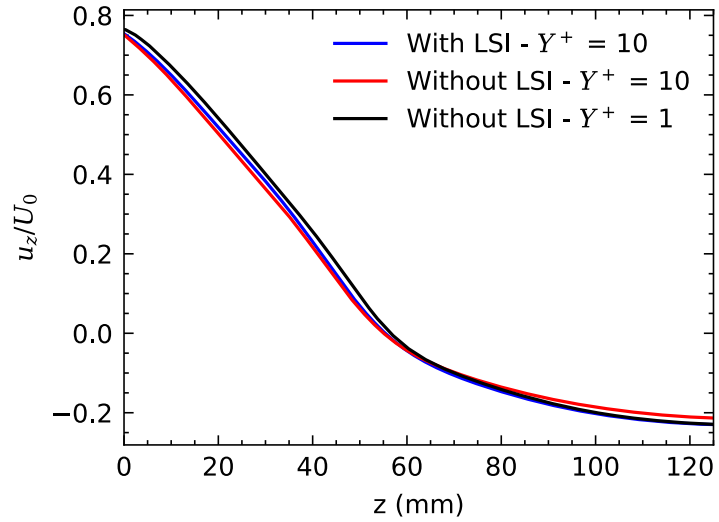

Figure C.8: Comparison of the normalized axial velocity with bulk velocity $U_0 = 18\ m/s$ along the middle axis

From figure C.7 and C.8 it is evident that all the simulations performed with and without swirler were identical even though the Y^+ was equal to unity.

Appendix -D

D.1. Mixture properties

```
#!/usr/bin/env python
# coding: utf-8

# In[16]:


import cantera as ct
import numpy as np
import gc


# In[17]:


# Equivalence ratios
Equivalence_ratios = [0.9] # Set equivalence ratios ranging from 0.4 to 0.8
# Hydrogen percentages by volume of fuel
H2_percentages = [80] # Set hydrogen volume percentages of the fuel ranging from 0
    to 100
gas = ct.Solution('gri30.yaml')
gas.transport_model= 'Multi'
gas.TP = 293, ct.one_atm
air_O2 = 0.21
air_N2 = 0.79


# In[20]:


gas = ct.Solution('gri30.yaml')
phi = 0.4
H2_percentage = 80
CH4_percentage = 100 - H2_percentage
x_H2 = H2_percentage/100
x_CH4 = CH4_percentage/100
mix_phases = [(gas, 1.0)]
fuel = {'H2':x_H2, 'CH4':x_CH4}
air = {'N2':air_N2/air_O2, 'O2':1.0}
gas.set_equivalence_ratio(phi, fuel, air)
mix = ct.Mixture(mix_phases)
```

```
mix.T = gas.T
mix.P = gas.P
mix.equilibrate('HP', solver='gibbs', max_steps=1000)
tad = mix.T
print('At phi = {0:12.4g}, Tad = {1:12.4g}'.format(phi, tad))
del gas
gc.collect()


# In[19]:



for phi in Equivalence_ratios:
    for H2_percentage in H2_percentages:
        gas = ct.Solution('gri30.yaml')
        gas.transport_model= 'Multi'
        gas.TP = 293.15, ct.one_atm
        air_O2 = 0.21
        air_N2 = 0.79
        CH4_percentage = 100 - H2_percentage
        x_H2 = H2_percentage/100
        x_CH4 = CH4_percentage/100
        fuel = {'H2':x_H2, 'CH4':x_CH4}
        air = {'N2':air_N2/air_O2, 'O2':1.0}
        # 3. Set the equivalence ratio
        gas.set_equivalence_ratio(phi, fuel, air)
        # Mass densities of fuel species
        rho_u = gas.density_mass # units: kg.m^-3
        mu_u = gas.viscosity # Pa.s
        cp_u = gas.cp_mass # units: J*K^-1*kg^-1
        cv_u = gas.cv_mass # units: J*K^-1*kg^-1
        nu_u = mu_u/rho_u # units: m^2.s^-1
        lambda_u= gas.thermal_conductivity # units: W.m^-1.K^-1
        alpha_u = lambda_u/(rho_u*cp_u) # units: m^2.s^-1

        print('Mixture propeties at phi=' + str(phi) + ', H2%=' + str(
    H2_percentage))
        print('Unburnt density of fuel mixture :' + str(rho_u) + 'kg.m^-3')
        print('Dynamic viscosity of air :' + str(mu_u) + 'Pa.s')
        print('kinematics viscosity of air :' + str(nu_u) + 'm^2.s^-1')

        # Set domain size (1D)
        width = 0.05  # units: m
        # Create object for freely-propagating premixed flames
        f = ct.FreeFlame(gas, width=width)
        # Set the criteria used to refine one domain
        f.set_refine_criteria(ratio=3, slope=0.1, curve=0.1)
        # Solve the equations
        f.solve(loglevel=0, auto=True)
        # Laminar flame speed
        S_L0 = f.velocity[0]*100 # units: cm.s^-1

        print('Laminar flame speed = ' + str(round(S_L0, 2)) + ' cm/s')
        print('-----------------------------------------------------')
```

D.2. Lewis number calculation

```
#!/usr/bin/env python
# coding: utf-8

# In[1]:


import cantera as ct
import numpy as np
import gc


# In[2]:


Equivalence_ratios = [0.8]
H = [100] # hydrogen amount in percentage


# In[3]:


for phi in Equivalence_ratios:
    for H_2 in H:
        gas = ct.Solution('gri30.yaml')
        gas.TP = 273, ct.one_atm
        M_O2 = 0.21
        M_N2 = 0.79
        CH_4 = 100 - H_2
        x_H2 = H_2/100
        x_CH4 = CH_4/100
        fuel = {'H2':x_H2, 'CH4':x_CH4}
        air = {'N2':M_N2/M_O2, 'O2':1.0}
        gas.set_equivalence_ratio(phi, fuel, air)
        rho_u = gas.density_mass # units: kg.m^-3
        lambda_u= gas.thermal_conductivity # units: W.m^-1.K^-1
        cp_u = gas.cp_mass # units: J*K^-1*kg^-1
        alpha_u = lambda_u/(rho_u*cp_u) # units: m^2.s^-1
        species_i_CH4 = gas.species_index('CH4')
        species_i_H2 = gas.species_index('H2')
        D_CH4 = gas.mix_diff_coeffs[species_i_CH4]
        D_H2 = gas.mix_diff_coeffs[species_i_H2]
        Le_CH4 =  alpha_u/D_CH4
        Le_H2 =  alpha_u/D_H2
        # The effective Lewis Number

#{Modelling and simulation of lean premixed turbulent methane/hydrogen/air flames with an effective Lewis Number Approch}
                              #[F.Dinkelacker & B. Manickam $ S.P.R Muppala (2011)]
                            #[DOI : http://dx.doi.org/10.1016/j.combustflame.2010.12.003 ]
        D_eff = (x_CH4*D_CH4) + (x_H2*D_H2)
        L_eff  =  alpha_u/D_eff
        print('At phi = {0:2.4g} for  {1:2.4g} % Hydrogen'.format(phi, H_2))
        print('The Lewis number of CH4 = {0:2.4g} '.format(Le_CH4))
        print('The Lewis number of h2 = {0:2.4g} '.format(Le_H2))
        print('The effective Lewis Number = {0:2.4g} '.format(L_eff))
        print('**************************************')
        del gas
        gc.collect()
```

E

Appendix -E

E.1. User Defined Functions (UDF)

E.1.1. Reaction rate - TFC

```
/************************************************************************
 UDF that specifies a custom turbulent flame speed and source
 for the premixed combustion model
 ************************************************************************/
 #include "udf.h"
 #include "sg_pdf.h" /* not included in udf.h so must include here */

 DEFINE_TURB_PREMIX_SOURCE(turb_flame_src,c,t,turb_flame_speed,source)
 {
   real k = C_K(c,t);
   real up = pow((2.0/3.0)*k, 0.5);
   real alpha = 3.131E-05;
   real omega = C_O(c,t);
   real eps = omega*0.09*k;
   real lx = (0.37*pow(up,3.0))/eps;
   real ut, ul, grad_c, rho_u, Xl, DV[ND_ND];
   ul = C_LAM_FLAME_SPEED(c,t);
   Calculate_unburnt_rho_and_Xl(t, &rho_u, &Xl);
   if(NNULLP(THREAD_STORAGE(t,SV_PREMIXC_G)))
    {
       NV_V(DV, =, C_STORAGE_R_NV(c,t,SV_PREMIXC_G));
       grad_c = sqrt(NV_DOT(DV,DV));
    }
   ut = 0.52*pow(up,0.75)*pow(ul,0.5)*pow(alpha,-0.25)*pow(lx,0.25);
   *turb_flame_speed = ut;
   *source = rho_u*ut*grad_c;
 }
```

E.1.2. Reaction rate - AFSW

```
/************************************************************************
    UDF that implements Muppala flame speed model in fluent
 ************************************************************************/

 #include "udf.h"
 #include "sg_pdf.h"


 DEFINE_TURB_PREMIX_SOURCE(turb_flame_src, c, t, turb_flame_speed, source)
 {
   real St, grad_c, rho_u, Xl, DV[ND_ND];
   real S_L0  = C_LAM_FLAME_SPEED(c,t);
   real turb_kin = C_K(c,t);
   real omega = C_O(c,t);
   real eps = omega*0.09*turb_kin;
   real uprime = pow((2./3.)*turb_kin, 0.5);
   real l_x = (0.37*pow(uprime,3))/eps;
   real mu = C_MU_L(c,t);
   real rho = C_R(c,t);
   real le_eff = 0.290;   /* need to be changed for different Flames mentioned in
    Table 4.1*/
   Calculate_unburnt_rho_and_Xl(t, &rho_u, &Xl);
   if(NNULLP(THREAD_STORAGE(t,SV_PREMIXC_G)))
     {
        NV_V (DV, =, C_STORAGE_R_NV(c,t,SV_PREMIXC_G));
        grad_c = sqrt(NV_DOT(DV, DV));
     }

   real ret = rho*uprime*l_x/mu;
   St = S_L0 + (0.46*S_L0*exp(-1*(le_eff-1))*pow(ret,0.25)*pow((uprime/S_L0),0.3))
    ;
   *turb_flame_speed = St;
   *source = rho_u*St*grad_c;
}
```

E.1.3. 'V' shape flame

```
/*
   ********************************************************************************

 UDF that simulates location depended density jump without combustion model in 3D
 ********************************************************************************
   */
 #include "udf.h"
 DEFINE_PROPERTY(density,c,t)
 {
 real rho, rho_u, rho_b;
 rho = C_R(c,t);
 rho_u = 1.12;
 rho_b = 0.20;
 real x[ND_ND];
 C_CENTROID(x,c,t);
 if (x[2] >= SQR(x[0]/0.1) + SQR(x[1]/0.1) + 0.074)
     rho = rho_b;
 else
     rho = rho_u;
return rho;
 }
```

E.1.4. 'M' shape flame

```
/*
   ********************************************************************************

 UDF that simulates location depended density jump without combustion model in 3D
 ********************************************************************************
   */
 #include "udf.h"
 DEFINE_PROPERTY(density,c,t)
 {
 real rho, rho_u, rho_b;
 rho = C_R(c,t);
 rho_u = 1.12;
 rho_b = 0.20;
 real x[ND_ND];
 C_CENTROID(x,c,t);
 if (SQR(x[0])+SQR(x[1]) >= SQR(0.02857) || (x[2] >= SQR(x[0]/0.1) + SQR(x[1]/0.1)
     + 0.074))
     rho = rho_b;
 else
     rho = rho_u;
return rho;
 }
```

Bibliography

[1] Incompressible lattice boltzmann method, Jun 2021. URL https://www.simscale.com/docs/incompressible-lbm-lattice-boltzmann-advanced/.

[2] IEA Shaping a Secure. Sustainable energy future for all.

[3] Yasir M Al-Abdeli and Assaad R Masri. Review of laboratory swirl burners and experiments for model validation. *Experimental Thermal and Fluid Science*, 69:178–196, 2015.

[4] Yaser H Alahmadi, Sawsan A Awadh, and Andrzej F Nowakowski. Simulation of swirling flow with a vortex breakdown using modified shear stress transport model. *Industrial & Engineering Chemistry Research*, 60(16):6016–6026, 2021.

[5] Mustafa Bal, Gökhan Kayansalçik, Özgür Ertunç, and Yakup Erhan Böke. Validation and comparison of 2d and 3d numerical simulations of flow in simplex nozzles. In *International Conference on Liquid Atomization and Spray Systems (ICLASS)*, volume 1, 2021.

[6] CG Bauer and TW Forest. Effect of hydrogen addition on the performance of methane-fueled vehicles. part i: effect on si engine performance. *International Journal of Hydrogen Energy*, 26(1):55–70, 2001.

[7] David Beerer, Vincent McDonell, Peter Therkelsen, and Robert K Cheng. Flashback and turbulent flame speed measurements in hydrogen/methane flames stabilized by a low-swirl injector at elevated pressures and temperatures. *Journal of engineering for gas turbines and power*, 136(3), 2014.

[8] John B Bell, Andrew J Aspden, Marcus S Day, and Michael J Lijewski. Numerical simulation of low mach number reacting flows. In *Journal of Physics: Conference Series*, volume 78, page 012004. IOP Publishing, 2007.

[9] Ali Cemal Benim and Khawar Jamil Syed. *Flashback mechanisms in lean premixed gas turbine combustion*. Academic press, 2014.

[10] Mounir Benzitouni, Zoubir Nemouchi, and Mohamed Salah Boulahlib. Numerical Study of a Flow through a Grid Placed in a Bunsen Burner. *International Journal of Heat and Technology*, 38(2):525–532, 2020. ISSN 03928764. doi: 10.18280/ijht.380230.

[11] R Borghi, C Bruno, and C Casci. Recent advances in aeronautical science. *Pergamont, London, UK*, 1984.

[12] KNC Bray, Paul A Libby, Goro Masuya, and JB Moss. Turbulence production in premixed turbulent flames. 1981.

[13] AV Brito Lopes, Nwabueze Emekwuru, Bernard Bonello, and Ebrahim Abtahizadeh. On the highly swirling flow through a confined bluff-body. *Physics of Fluids*, 32(5):055105, 2020.

[14] Stephan Burmberger and Thomas Sattelmayer. Optimization of the aerodynamic flame stabilization for fuel flexible gas turbine premix burners. *Journal of Engineering for Gas Turbines and Power*, 133(10), 2011.

[15] By. Combustion basics for beginner, Sep 2020. URL https://cfdflowengineering.com/combustion-basics-for-beginner/.

[16] Iñigo Capellán-Pérez, Inaki Arto, Josue M Polanco-Martinez, Mikel González-Eguino, and Marc B Neumann. Likelihood of climate change pathways under uncertainty on fossil fuel resource availability. *Energy & Environmental Science*, 9(8):2482–2496, 2016.

[17] CK Chan, KS Lau, WK Chin, and RK Cheng. Freely propagating open premixed turbulent flames stabilized by swirl. In *Symposium (International) on Combustion*, volume 24, pages 511–518. Elsevier, 1992.

[18] R. K. Cheng, D. Littlejohn, W. A. Nazeer, and K. O. Smith. Laboratory studies of the flow field characteristics of low-swirl injectors for adaptation to fuel-flexible turbines. *Journal of Engineering for Gas Turbines and Power*, 130(2), 2008. ISSN 07424795. doi: 10.1115/1.2795786.

[19] R. K. Cheng, D. Littlejohn, P. A. Strakey, and T. Sidwell. Laboratory investigations of a low-swirl injector with H2 and CH4 at gas turbine conditions. *Proceedings of the Combustion Institute*, 32 II(2):3001–3009, 2009. ISSN 15407489. doi: 10.1016/j.proci.2008.06.141. URL http://dx.doi.org/10.1016/j.proci.2008.06.141.

[20] RK Cheng and D Littlejohn. *Effects of combustor geometry on the flowfields and flame properties of a low-swirl injector*, volume 43130. 2008.

[21] RK Cheng and D Littlejohn. Laboratory study of premixed h2-air and h2–n2-air flames in a low-swirl injector for ultralow emissions gas turbines. *Journal of Engineering for Gas Turbines and Power*, 130(3), 2008.

[22] RK Cheng, IG Shepherd, B Bedat, and L Talbot. Premixed turbulent flame structures in moderate and intense isotropic turbulence. *Combustion Science and Technology*, 174 (1):29–59, 2002.

[23] RK Cheng, D Littlejohn, WA Nazeer, and KO Smith. Laboratory studies of the flow field characteristics of low-swirl injectors for adaptation to fuel-flexible turbines. *Journal of Engineering for Gas Turbines and Power*, 130(2), 2008.

[24] Robert K Cheng, Scott A Fable, D Schmidt, L Arellano, and KO Smith. Development of a low swirl injector concept for gas turbines. Technical report, Lawrence Berkeley National Lab., CA (US), 2000.

[25] N. A. Chigier and A. Chervinsky. Experimental investigation of swirling vortex motion in jets. *Journal of Applied Mechanics, Transactions ASME*, 34(2):443–451, 1964. ISSN 15289036. doi: 10.1115/1.3607703.

[26] G Ciccarelli and S Dorofeev. Flame acceleration and transition to detonation in ducts. *Progress in energy and combustion science*, 34(4):499–550, 2008.

[27] Andres Colorado. *Pollutant Emissions and Lean Blowoff Limits of Fuel Flexible Burners Operating on Gaseous Renewable and Fossil Fuels*. University of California, Irvine, 2016.

[28] Gerhard Damköhler. The effect of turbulence on the flame velocity in gas mixtures. 1947.

[29] F Dinkelacker, B Manickam, and SPR Muppala. Modelling and simulation of lean premixed turbulent methane/hydrogen/air flames with an effective lewis number approach. *Combustion and Flame*, 158(9):1742–1749, 2011.

[30] James F Driscoll. Turbulent premixed combustion: Flamelet structure and its effect on turbulent burning velocities. *Progress in Energy and Combustion Science*, 34(1): 91–134, 2008.

[31] XR Duan, P Weigand, W Meier, O Keck, W Stricker, M Aigner, and B Lehmann. Experimental investigations and laser based validation measurements in a gas turbine model combustor. *Progress in Computational Fluid Dynamics, an International Journal*, 4(3-5): 175–182, 2004.

[32] Franz Durst. *Fluid mechanics: an introduction to the theory of fluid flows*. Springer Science & Business Media, 2008.

[33] Dominik Ebi and Noel T Clemens. Experimental investigation of upstream flame propagation during boundary layer flashback of swirl flames. *Combustion and Flame*, 168: 39–52, 2016.

[34] G. Eggenspieler, P. A. Strakey, and T. Sidwell. Experimental and numerical study of flashback in the SimVal combustion chamber. *46th AIAA Aerospace Sciences Meeting and Exhibit*, 26505(January), 2008. doi: 10.2514/6.2008-1025.

[35] Christian Eichler, Georg Baumgartner, and Thomas Sattelmayer. Experimental investigation of turbulent boundary layer flashback limits for premixed hydrogen-air flames confined in ducts. *Journal of Engineering for Gas Turbines and Power*, 134(1), 2012.

[36] Ivar S Ertesvåg and Bjørn F Magnussen. The eddy dissipation turbulence energy cascade model. *Combustion science and technology*, 159(1):213–235, 2000.

[37] MP Escudier and JJ Keller. Recirculation in swirling flow-a manifestation of vortex breakdown. *AIAA journal*, 23(1):111–116, 1985.

[38] Aaron Alex Frank. *Effects of Downscaling on the Low Swirl Burner*. University of California, Berkeley, 2019.

[39] Robert Maurice Fristrom and Arthur Ayer Westenberg. Flame structure(text on flame structure with respect to high- temperature spectroscopy, transport properties, thermodynamics and chemical heat release in gas streams). *NEW YORK, MCGRAW-HILL BOOK CO., 1965. 424 P. NAVY-ARPA-ARMY-SUPPORTED RESEARCH*, 1965.

[40] J. Fritz, M. Kröner, and T. Sattelmayer. Flashback in a swirl burner with cylindrical premixing zone. *Journal of Engineering for Gas Turbines and Power*, 126(2):276–283, 2004. ISSN 07424795. doi: 10.1115/1.1473155.

[41] Jassin Fritz, Martin Kröner, and Thomas Sattelmayer. Flashback in a swirl burner with cylindrical premixing zone. In *Turbo Expo: Power for Land, Sea, and Air*, volume 78514, page V002T02A021. American Society of Mechanical Engineers, 2001.

[42] Irvin Glassman, Richard A Yetter, and Nick G Glumac. *Combustion*. Academic press, 2014.

[43] David G. Goodwin, Harry K. Moffat, Ingmar Schoegl, Raymond L. Speth, and Bryan W. Weber. Cantera: An object-oriented software toolkit for chemical kinetics, thermodynamics, and transport processes. https://www.cantera.org, 2022. Version 2.6.0.

[44] Ansys Fleunt Teory Guide. Ansys fleunt teory guide. 2013.

[45] Ashwani K Gupta, David G Lilley, and Nick Syred. Swirl flows. *Tunbridge Wells*, 1984.

[46] MV Heitor, AMKP Taylor, and JH Whitelaw. Influence of confinement on combustion instabilities of premixed flames stabilized on axisymmetric baffles. *Combustion and Flame*, 57(1):109–121, 1984.

[47] Ying Huang and Vigor Yang. Dynamics and stability of lean-premixed swirl-stabilized combustion. *Progress in energy and combustion science*, 35(4):293–364, 2009.

[48] JCR Hunt, I Eames, and J Westerweel. Mechanics of inhomogeneous turbulence and interfacial layers. *Journal of Fluid Mechanics*, 554:499–519, 2006.

[49] Our World in Data. Energy consumption by source. URL https://ourworldindata.org/grapher/energy-consumption-by-source-and-region?stackMode=absolute.

[50] Piero Iudiciani. *Swirl stabilized premixed flame analysis using of LES and POD*. Lund University, 2012.

[51] Jun Ji and Jay P Gore. Flow structure in lean premixed swirling combustion. *Proceedings of the Combustion Institute*, 29(1):861–867, 2002.

[52] Arne V Johansson and Magnus Hallbäck. Modelling of rapid pressure—strain in reynolds-stress closures. *Journal of Fluid Mechanics*, 269:143–168, 1994.

[53] M. R. Johnson, D. Littlejohn, W. A. Nazeer, K. O. Smith, and R. K. Cheng. A comparison of the flowfields and emissions of high-swirl injectors and low-swirl injectors for lean premixed gas turbines. *Proceedings of the Combustion Institute*, 30 II(2):2867–2874, 2005. ISSN 15407489. doi: 10.1016/j.proci.2004.07.040. URL http://dx.doi.org/10.1016/j.proci.2004.07.040.

[54] MR Johnson, D Littlejohn, WA Nazeer, KO Smith, and RK Cheng. A comparison of the flowfields and emissions of high-swirl injectors and low-swirl injectors for lean premixed gas turbines. *Proceedings of the Combustion Institute*, 30(2):2867–2874, 2005.

[55] WP Jones and Brian Edward Launder. The prediction of laminarization with a two-equation model of turbulence. *International journal of heat and mass transfer*, 15(2): 301–314, 1972.

[56] Alireza Kalantari, Elliot Sullivan-Lewis, and Vincent McDonell. Application of a turbulent jet flame flashback propensity model to a commercial gas turbine combustor. *Journal of Engineering for Gas Turbines and Power*, 139(4), 2017.

[57] RD Khadase and SK Bhele. Performance evaluation of combustor by using different swirler. *Int. J. Res. Appl. Sci. Eng. Technol*, 4:85–90, 2016.

[58] F Kiesewetter, M Konle, and TJJoEfGT Sattelmayer. Analysis of combustion induced vortex breakdown driven flame flashback in a premix burner with cylindrical mixing zone. 2007.

[59] Frank Kiesewetter, Christoph Hirsch, Jassin Fritz, Thomas Sattelmayer, et al. Two-dimensional flashback simulation in strongly swirling flows. In *ASME Turbo Expo 2003, collocated with the 2003 International Joint Power Generation Conference*, pages 293–300. American Society of Mechanical Engineers Digital Collection, 2003.

[60] Kyu Tae Kim, Jong Guen Lee, Hyung Ju Lee, Bryan D Quay, and Domenic A Santavicca. Characterization of forced flame response of swirl-stabilized turbulent lean-premixed flames in a gas turbine combustor. *Journal of engineering for gas turbines and power*, 132(4), 2010.

[61] Johan C Kok. Resolving the dependence on freestream values for the k-turbulence model. *AIAA journal*, 38(7):1292–1295, 2000.

[62] Marco Konle, Frank Kiesewetter, and Thomas Sattelmayer. Simultaneous high repetition rate PIV-LIF-measurements of CIVB driven flashback. *Experiments in Fluids*, 44 (4):529–538, 2008. ISSN 07234864. doi: 10.1007/s00348-007-0411-2.

[63] Marco Konle, Frank Kiesewetter, and Thomas Sattelmayer. Simultaneous high repetition rate piv–lif-measurements of civb driven flashback. *Experiments in Fluids*, 44(4): 529–538, 2008.

[64] Martin Kroener, Thomas Sattelmayer, Jassin Fritz, Frank Kiesewetter, and Christoph Hirsch. Flame propagation in swirling flows—effect of local extinction on the combustion induced vortex breakdown. *Combustion Science and Technology*, 179(7):1385–1416, 2007.

[65] M. Kröner, J. Fritz, and T. Sattelmayer. Flashback limits for combustion induced vortex breakdown in a swirl burner. *Journal of Engineering for Gas Turbines and Power*, 125 (3):693–700, 2003. ISSN 07424795. doi: 10.1115/1.1582498.

[66] Pijush K Kundu, Ira M Cohen, and David R Dowling. *Fluid mechanics*. Academic press, 2015.

[67] Kenneth K Kuo. *Principles of combustion*. Number TJ254. 5 K85 2005. 2005.

[68] Chung K Law. *Combustion physics*. Cambridge university press, 2010.

[69] CK Law and CJ Sung. Structure, aerodynamics, and geometry of premixed flamelets. *Progress in energy and combustion science*, 26(4-6):459–505, 2000.

[70] Arthur H Lefebvre. *Gas turbine combustion*. CRC press, 1998.

[71] Tim C Lieuwen. *Unsteady combustor physics*. Cambridge University Press, 2012.

[72] Tim C Lieuwen and Vigor Yang. *Gas turbine emissions*, volume 38. Cambridge university press, 2013.

[73] AN Lipatnikov and J Chomiak. Turbulent flame speed and thickness: phenomenology, evaluation, and application in multi-dimensional simulations. *Progress in energy and combustion science*, 28(1):1–74, 2002.

[74] D. Littlejohn and R. K. Cheng. Fuel effects on a low-swirl injector for lean premixed gas turbines. *Proceedings of the Combustion Institute*, 31 II(2):3155–3162, 2007. ISSN 15407489. doi: 10.1016/j.proci.2006.07.146.

[75] David Littlejohn and RK Cheng. Fuel effects on a low-swirl injector for lean premixed gas turbines. *Proceedings of the Combustion Institute*, 31(2):3155–3162, 2007.

[76] O Lucca-Negro and T O'doherty. Vortex breakdown: a review. *Progress in energy and combustion science*, 27(4):431–481, 2001.

[77] Marcin Lutyński. An overview of potential benefits and limitations of compressed air energy storage in abandoned coal mines. In *IOP Conference Series: Materials Science and Engineering*, volume 268, page 012006. IOP Publishing, 2017.

[78] Fanhua Ma, Yu Wang, Haiquan Liu, Yong Li, Junjun Wang, and Shuli Zhao. Experimental study on thermal efficiency and emission characteristics of a lean burn hydrogen enriched natural gas engine. *International Journal of Hydrogen Energy*, 32(18): 5067–5075, 2007.

[79] Bjørn F Magnussen and Bjørn H Hjertager. On mathematical modeling of turbulent combustion with special emphasis on soot formation and combustion. In *Symposium (international) on Combustion*, volume 16, pages 719–729. Elsevier, 1977.

[80] Seyedeh Sepideh Marashi. Network modeling application to laminar flame speed and nox prediction in industrial gas turbines, 2013.

[81] Sara McAllister, Jyh-Yuan Chen, and A Carlos Fernandez-Pello. *Fundamentals of combustion processes*, volume 302. Springer, 2011.

[82] W Meier, O Keck, B Noll, O Kunz, and W Stricker. Investigations in the tecflam swirling diffusion flame: Laser raman measurements and cfd calculations. *Applied Physics B*, 71(5):725–731, 2000.

[83] WEIGAND Meier, Peter Weigand, Xuru R Duan, and Robert Giezendanner-Thoben. Detailed characterization of the dynamics of thermoacoustic pulsations in a lean premixed swirl flame. *Combustion and Flame*, 150(1-2):2–26, 2007.

[84] Florian R Menter. Two-equation eddy-viscosity turbulence models for engineering applications. *AIAA journal*, 32(8):1598–1605, 1994.

[85] P Minutolo, G Gambi, and A D'alessio. The optical band gap model in the interpretation of the uv-visible absorption spectra of rich premixed flames. In *Symposium (International) on Combustion*, volume 26, pages 951–957. Elsevier, 1996.

[86] DP Mishra. *Fundamentals of combustion*. PHI Learning Pvt. Ltd., 2007.

[87] S Muppala, B Manickam, and F Dinkelacker. A comparative study of different reaction models for turbulent methane/hydrogen/air combustion. *Journal of Thermal Engineering*, 1(5):367–380, 2015.

[88] Siva PR Muppala and Sooraj Paleli M Vasudevan. Rans studies of hydrogen-enrichment premixed turbulent flames. In *IOP Conference Series: Materials Science and Engineering*, volume 1080, page 012046. IOP Publishing, 2021.

[89] SP Reddy Muppala, Naresh K Aluri, Friedrich Dinkelacker, and Alfred Leipertz. Development of an algebraic reaction rate closure for the numerical calculation of turbulent premixed methane, ethylene, and propane/air flames for pressures up to 1.0 mpa. *Combustion and flame*, 140(4):257–266, 2005.

[90] B Nagalingam, F Duebel, and K Schmillen. Performance study using natural gas, hydrogen-supplemented natural gas and hydrogen in avl research engine. *International Journal of Hydrogen Energy*, 8(9):715–720, 1983.

[91] Mathias Neumayer and C Hirsch. Rans simulation of methane combustion in a low swirl burner. *Doctoral dissertation, M. Sc. thesis*, 2013.

[92] Frans TM Nieuwstadt, Jerry Westerweel, and Bendiks J Boersma. *Turbulence: introduction to theory and applications of turbulent flows*. Springer, 2016.

[93] David R. Noble, Qingguo Zhang, Akbar Shareef, Jeremiah Tootle, Andrew Meyers, and Tim Lieuwen. Syngas mixture composition effects upon flashback and blowout. *Proceedings of the ASME Turbo Expo*, 1(December 2015):357–368, 2006. doi: 10.1115/GT2006-90470.

[94] Intergovernmental Panel on Climate Change. Ipcc special report on the ocean and cryosphere in a changing climate. 2019.

[95] S Ouali, AH Bentebbiche, and T Belmrabet. Numerical simulation of swirl and methane equivalence ratio effects on premixed turbulent flames and nox apparitions. *Journal of Applied Fluid Mechanics*, 9(2), 2016.

[96] Ronald L Panton. *Incompressible flow*. John Wiley & Sons, 2013.

[97] Norbert Peters. Turbulent combustion, 2001.

[98] Heinz Pitsch. Enabling advanced modeling and simulations for fuel-flexible combustors. Technical report, Stanford Univ., CA (United States), 2010.

[99] Thierry Poinsot and Denis Veynante. *Theoretical and numerical combustion*. RT Edwards, Inc., 2005.

[100] SB Pope. Turbulent premixed flames. *Annual review of fluid mechanics*, 19(1):237–270, 1987.

[101] AA Putnam and GD Markstein. Non-steady flame propagation. *Chapter F, Pergamon Press, The Macmillan Co., NY*, 1964.

[102] O Ramadan, Siddig Omer, Muhyiddine Jradi, H Sabir, and S Riffat. Analysis of compressed air energy storage for large-scale wind energy in suez, egypt. *International Journal of Low-Carbon Technologies*, 11(4):476–488, 2016.

[103] Ranzijn. Three-dimensional combustion modeling of the low swirl burner using fluent. *Doctoral dissertation, M. Sc. thesis*, 2012.

[104] Rodrigo Bento Rebouças, Ivan Rosa de Siqueira, and Taygoara Felamingo de Oliveira. An investigation of the boundary-layer equations of a dilute and monodispersed emulsion of very viscous drops.

[105] GA Richards, MM McMillian, RS Gemmen, WI A Rogers, and SR Cully. Issues for low-emission, fuel-flexible power systems. *Progress in Energy and Combustion Science*, 27(2):141–169, 2001.

[106] Lewis Fry Richardson. *Weather prediction by numerical process*. Cambridge university press, 2007.

[107] Pierre Sagaut, Marc Terracol, and Sebastien Deck. *Multiscale and multiresolution approaches in turbulence-LES, DES and Hybrid RANS/LES Methods: Applications and Guidelines*. World Scientific, 2013.

[108] RW Schefer, M Namazian, J Kelly, and M Perrin. Effect of confinement on bluff-body burner recirculation zone characteristics and flame stability. *Combustion science and technology*, 120(1-6):185–211, 1996.

[109] Fernando Schneider, Peter Gerlinger, and Manfred Aigner. Enhanced mixing in supersonic combustion. In *High Performance Computing in Science and Engineering'04*, pages 213–223. Springer, 2005.

[110] HJ Sheen, WJ Chen, SY Jeng, and TL Huang. Correlation of swirl number for a radial-type swirl generator. *Experimental thermal and fluid science*, 12(4):444–451, 1996.

[111] Tsan-Hsing Shih, William W Liou, Aamir Shabbir, Zhigang Yang, and Jiang Zhu. A new k-□ eddy viscosity model for high reynolds number turbulent flows. *Computers & fluids*, 24(3):227–238, 1995.

[112] Daisuke Shimokuri and Satoru Ishizuka. Flame stabilization with a tubular flame. *Proceedings of the Combustion Institute*, 30(1):399–406, 2005.

[113] S Sivasegaram and JH Whitelaw. Oscillations in confined disk-stabilized flames. *Combustion and flame*, 68(2):121–129, 1987.

[114] DB Spalding. Mixing and chemical reaction in steady confined turbulent flames. In *Symposium (International) on combustion*, volume 13, pages 649–657. Elsevier, 1971.

[115] Charles G Speziale, Sutanu Sarkar, and Thomas B Gatski. Modelling the pressure–strain correlation of turbulence: an invariant dynamical systems approach. *Journal of fluid mechanics*, 227:245–272, 1991.

[116] Thomas Sponfeldner, Nikolaos Soulopoulos, Frank Beyrau, Yannis Hardalupas, Alex MKP Taylor, and J Christos Vassilicos. The structure of turbulent flames in fractal- and regular-grid-generated turbulence. *Combustion and Flame*, 162(9):3379–3393, 2015.

[117] P Strakey, T Sidwell, and J Ontko. Investigation of the effects of hydrogen addition on lean extinction in a swirl stabilized combustor. *Proceedings of the combustion institute*, 31(2):3173–3180, 2007.

[118] Mohammed Yekini Suberu, Mohd Wazir Mustafa, and Nouruddeen Bashir. Energy storage systems for renewable energy power sector integration and mitigation of intermittency. *Renewable and Sustainable Energy Reviews*, 35:499–514, 2014.

[119] CJ Sung, JB Liu, and CK Law. On the scalar structure of nonequidiffusive premixed flames in counterflow. *Combustion and flame*, 106(1-2):168–183, 1996.

[120] Nicholas Syred. A review of oscillation mechanisms and the role of the precessing vortex core (pvc) in swirl combustion systems. *Progress in Energy and Combustion Science*, 32(2):93–161, 2006.

[121] Peter L Therkelsen, David Littlejohn, and Robert K Cheng. Parametric study of low-swirl injector geometry on its operability. In *Turbo Expo: Power for Land, Sea, and Air*, volume 44687, pages 309–318. American Society of Mechanical Engineers, 2012.

[122] Stephen R Turns et al. *Introduction to combustion*, volume 287. McGraw-Hill Companies, 1996.

[123] Maarten Vanierschot and Eric Van den Bulck. Influence of swirl on the initial merging zone of a turbulent annular jet. *Physics of fluids*, 20(10):105104, 2008.

[124] Henk Kaarle Versteeg and Weeratunge Malalasekera. *An introduction to computational fluid dynamics: the finite volume method*. Pearson education, 2007.

[125] D Veynante, A Trouvé, KNC Bray, and T Mantel. Gradient and counter-gradient scalar transport in turbulent premixed flames. *Journal of Fluid Mechanics*, 332(1):263–293, 1997.

[126] Jurgen Warnatz, Ulrich Maas, Robert W Dibble, and J Warnatz. *Combustion*. Springer, 2006.

[127] John K Watterson, Isobel J Connell, A Mark Savill, and William N Dawes. A solution-adaptive mesh procedure for predicting confined explosions. *International journal for numerical methods in fluids*, 26(2):235–247, 1998.

[128] David C Wilcox. Formulation of the kw turbulence model revisited. *AIAA journal*, 46(11): 2823–2838, 2008.

[129] FA Williams. Criteria for existence of wrinkled laminar flame structure of turbulent premixed flames. 1976.

[130] Forman A Williams. *Combustion theory*. CRC Press, 2018.

[131] DT Yegian and RK Cheng. Development of a lean premixed low-swirl burner for low nox practical applications. *Combustion science and technology*, 139(1):207–227, 1998.

[132] Dapeng Zhang, Qinghua Liu, and Yongdan Li. Design of flow battery. In *Reactor and process design in sustainable energy technology*, pages 61–97. Elsevier, 2014.

[133] V Zimont, Wolfgang Polifke, Marco Bettelini, and Wolfgang Weisenstein. An efficient computational model for premixed turbulent combustion at high reynolds numbers based on a turbulent flame speed closure. 1998.

[134] Vladimir L Zimont, Andrei N Lipatnikov, et al. A numerical model of premixed turbulent combustion of gases. *Chem. Phys. Reports*, 14(7):993–1025, 1995.